Single Particle Dynamics in Liquid Metals

Mark Patty

Department of Physics and Astronomy, University of Missouri-Columbia, Columbia, Missouri 65211, United States

Single Particle Dynamics in Liquid Metals

A Dissertation
presented to
the Faculty of the Graduate School
University of Missouri-Columbia

In Partial Fulfillment
of the Requirements for the Degree
of Doctor of Philosophy

---

by

Mark R. Patty

Wouter Montfrooij, _____ Dissertation Supervisor

December 2008

The undersigned, appointed by the Dean of the Graduate School, have examined the dissertation entitled:

Single Particle Dynamics in Liquid Metals

presented by Mark Patty
a candidate for the degree of Doctor of Philosophy
and hereby certify that in their opinion it is worthy of acceptance.

Wouter Montfrooij

Paul Miceli

Haskell Taub

Owen Vajk

Robert A. Winholtz

To my parents,
for always supporting me

Acknowledgements

I am grateful to my advisor Wouter Montfrooij for supporting me with my research and writing. It means a lot that he was always helpful and open to my countless questions.

I would also like to thank my comprehensive and dissertation committees (consisting of Hak Taub, Paul Miceli, Andy Winholtz, Owen Vajk, and Maikel Rheinstadter) for their comments and suggestions.

I would also like to thank my collaborators Keary Schoen and Zhara Yamani for their invaluable help with our articles.

Next, I would like to thank all the friends/students/colleagues in Wouter's lab for keeping me on track and keeping me fed on Tuesdays.

I would also like to acknowledge the American Chemical Society Petroleum Research Fund (ACS PRF 42615-G10) for financially supporting me in my research.

Finally, I would like to thank all of my family and friends for never giving up on me and for consistently telling me that I would be a doctor one day.

Contents

ACKNOWLEDGMENTS viii

TABLE OF CONTENTS ix

LIST OF TABLES xi

LIST OF FIGURES xii

ABSTRACT xvi

1 Introduction 1

2 Scattering Theory 8
- 2.1 Basic neutron properties 8
- 2.2 Graphical representation of neutron scattering 9
- 2.3 Definition of cross-section 19
- 2.4 Differential cross-section 21
- 2.5 Partial differential cross-section 22
- 2.6 Coherent and incoherent cross-sections 23
- 2.7 Liquids 24

3 Unexplained broad mode in liquid metals 27
- 3.1 Introduction 27
- 3.2 Theory 31
- 3.3 Results 38
- 3.4 Discussion 47

4 Experiments at MURR and Chalk River 50
- 4.1 Polarized experiments at MURR 51
- 4.2 Polarized experiments at Chalk River 53
- 4.3 Unpolarized inelastic experiments at MURR 59

5 Attenuation, monitor contamination and multiple scattering corrections 64
- 5.1 Attenuation correction 64
- 5.2 Monitor contamination correction 68
- 5.3 Multiple scattering correction 72

6 Partial Wave Method 84
- 6.1 Introduction 84
- 6.2 Glory scattering 92
- 6.3 Runge-Kutta-Gill method for solving differential equations 96
- 6.4 Bernstein trial for RKG4 approximation 98

7 Quantum interference effects in various liquid metals 105
7.1 Introduction 105
7.2 Liquid helium 107
7.3 Liquid lithium 110
7.4 Liquid sodium 111
7.5 Liquid gallium 116
7.6 Liquid lead 117

8 Immediate outlook 122
8.1 Fluctuating magnetic moments in other liquid metals 122
8.2 Quantum interference effects and their influence on the cage-diffusion mechanism 122

References 124

Appendix A Differential cross-section 127
A.1 Fermi's Golden Rule 127
A.2 Density of states 127
A.3 Particle wavefunction and the potential function 128
A.4 Fermi pseudopotential 129

Appendix B Partial differential cross-section 131
B.1 Hamiltonian 131
B.2 Summation notation 131
B.3 Heisenberg operator 132
B.4 Thermal average 132
B.5 Small momentum transfer approximation 132

Appendix C magnetic surprise for liquids- physics world.com 135

Appendix D Corrections to data 138
D.1 Slab attenuation 138

Appendix E Partial wave method 141
E.1 Incident plane wave 141
E.2 Full wavefunction 142

Appendix F Computer code 145
F.1 Multiple scattering code 145
F.2 RKG4 and phase shift code 173

VITA 185

List of tables

3.1 The observed magnetic cross-section σ_{magn} and the corresponding fraction n of ions with a magnetic moment, calculated for the most likely quantum numbers of the unpaired electron using Eq. 3.5. 37

4.1 The experimental values for the count rate per 400000 monitor counts for the flip and non-flip channels for samples of liquid and solid gallium contained in a quartz sample cell. The temperature of the liquid was held just above the melting point, the solid was kept just below the melting point at room temperature. 53

List of figures

1.1 Microscopic density fluctuations 2

2.1 Schematic of the required probing wavelength in the given system 10

2.2 Schematic of possible scattering process 11

2.3 Schematic representation of scattering components for a liquid 13

2.4 Schematic representation of scattering components for a liquid at low q 16

2.5 Schematic of triple-axis spectrometer 18

3.1 Schematic representation of how cage diffusion can lead to short-lived, fluctuating magnetic moments 30

3.2 Schematic representation of the components that make up the scattering by a liquid at low q and the relative strengths of such 32

3.3 The dynamic structure factor of liquid mercury at small momentum transfer 35

3.4 The static structure factor of liquid lead by X-ray and neutron scattering 42

3.5 Static structure factor of liquid aluminum above the melting point as measured by neutron scattering and X-ray scattering 44

3.6 The unnormalized static structure factor of liquid gallium at two temperatures 46

4.1 Schematic of the first cell 52

4.2 Schematic of Peltier cell 54

4.3 Spin-flip signal for neutrons scattered elastically by Ga 55

4.4 The scattered neutron intensity in liquid Ga at 303K 56

4.5 Inelastic scans of Gallium in liquid and solid phases 57

4.6 Directly and indirectly measured empty quartz cell scattering 58

4.7 Neutron scattering signal at constant $E = 3$ meV as a function of wave number q 60

4.8	Schematic of the second cell	61
4.9	The inelastic neutron scattering spectra of liquid Ga for various q-values	62
5.1	Schematic of the single scattering in a slab of material of thickness d	66
5.2	Schematic of the single scattering in a slab of material of thickness d at an angle ϕ_0	67
5.3		67
5.4	The scattered intensity for liquid Ga at 293 K for q= 2.52 Å^{-1} as measured at a thermal source triple-axis spectrometer	71
5.5	The monitor correction ratio with respect to energy transfer	72
5.6	Schematic of scattering components	73
5.7	Possible particle paths for multiple scattering events	75
5.8	The first order scattering model	78
5.9	The second order scattering model	79
5.10	The third order scattering calculated based on a Lorentzian model for single scattering	80
5.11	The inelastic neutron scattering spectra of liquid Ga for various q-values	83
6.1	Schematic representation of two particles scattering	85
6.2	Helium oscillations	86
6.3	Helium oscillations	86
6.4	Schematic representation of cage diffusion	87
6.5	Reported oscillations from Scopigno *et al.* [2]	88
6.6	Schematic of potential $V(r)$ and the radial wave function, $R_l(r)$	91
6.7	Scattering of an incident beam of particles by a center of force	93
6.8	Schematic representation of glory scattering	94
6.9	Effective potential resulting from a combination of a two-body interaction combined with an impact parameter s	94
6.10	Schematic of deflection angle ϕ versus impact parameter s for the potential shown in Fig. 6.9	95
6.11	l=0 radial wave solutions	99
6.12	l=10 radial wave solutions	100

6.13 l=15 radial wave solutions 100

6.14 l=20 radial wave solutions 101

6.15 Change in phase shift between $l = 11$ and $l = 12$ with A=5 102

6.16 Phase constant vs. the angular momentum quantum number 102

6.17 Zoom of Fig. 6.16 103

6.18 Quantum calculation of differential cross-section vs. angle 104

7.1 First three even l terms of the phase using the LJ(12,6) potential 108

7.2 First three even l terms of the phase using the repulsive part of the LJ(12,6) potential 108

7.3 Shown are the total cross-section, diffusion cross-section, and viscosity cross-section for liquid helium using Bose statistics 109

7.4 The total Bose cross-section, total Fermi cross-section, and total classical cross-section for liquid helium 110

7.5 The total cross-section, diffusion cross-section, and viscosity cross-section for liquid lithium using Bose statistics 111

7.6 The total Bose cross-section, total Fermi cross-section, and total classical cross-section for liquid lithium 112

7.7 Two methods of calculating the phase shifts for liquid lithium at a relative velocity of 50 m/s 112

7.8 Same as Fig. 7.7 except at a relative velocity of 200 m/s. 113

7.9 Same as Fig. 7.7 except at a relative velocity of 500 m/s. 113

7.10 Same as Fig. 7.7 except at a relative velocity of 1200 m/s. 114

7.11 The total cross-section, diffusion cross-section, and viscosity cross-section for liquid sodium using Bose statistics 114

7.12 The total Bose cross-section, total Fermi cross-section, and total classical cross-section for liquid sodium 115

7.13 The total cross-section of liquid sodium for Bose statistics 115

7.14 The total cross-section of liquid gallium for Bose statistics 116

7.15 The two methods of calculating the phase shifts for liquid gallium at a relative velocity of 20 m/s 118

7.16 Same as Fig. 7.15 except at a relative velocity of 60 m/s. 119

7.17 Same as Fig. 7.15 except at a relative velocity of 200 m/s. 119

7.18 Same as Fig. 7.15 except at a relative velocity of 600 m/s. 120

7.19 Displayed oscillations from heavy elements (like Pb) 121

ABSTRACT

Our understanding of the liquid (or molten) state of metals has progressed far within the past decades. Thanks to the advances in both x-ray and neutron scattering sources, it is now possible to measure the dynamics on a microscopic scale with very good statistical accuracy. The dynamics given by a single particle in a liquid metal owe to self-diffusion and cage diffusion. Presented are quasielastic neutron scattering studies of various liquid metals at low momentum transfers. The first part of this thesis is devoted to the investigation of a new (and unpredicted) contribution to the hydrodynamics of liquid metals. We present a literature review of published experiments to verify the presence of this new mode in liquid metals, followed by a possible explanation for its presence in terms of collision-induced magnetism. Next, we present a neutron scattering study at low momentum transfers using liquid gallium to verify the existence of this new contribution. The contribution turns out to be non-magnetic in origin, so another set of neutron scattering experiments is carried out, determining that the contribution should be attributed to multiple scattering processes in liquid gallium (though these same experiments suggest that this contribution is not a multiple scattering effect in liquid lead and mercury). In the last chapters of the thesis we investigate the potential effects of quantum mechanical diffraction effects on the collision between two ions. To carry out the investigation, we solved the collision between two almost classical particles using the partial wave method. We calculate the importance of this diffraction mechanism in liquid metals and present their influence on the neutron scattering cross-section when measuring the collision between two ions, given by an oscillation in the scattering cross-section.

1
Introduction

Our understanding of the liquid (or molten) state of metals has progressed far within the past decades. Thanks to the advances in both x-ray and neutron scattering sources, it is now possible to measure the dynamics on a microscopic scale with very good statistical accuracy. The interest in understanding liquid metals on a microscopic scale is easy to fathom; liquid metals have all the complexities of simple fluids like Argon, and in addition the sea of conduction electrons interacts with itself and with the positively charged ions. So the key question is how does a liquid behave when it is immersed in a second, penetrating fluid? What new phenomena, compared to ordinary liquids, does this interaction lead to?

The most noticeable property of liquid metals when probed on a small length scale is that a liquid metal can maintain short wavelength sound waves. First, in order to give the reader a general idea of what we mean by a small scale density fluctuation, and how it relaxes back to equilibrium, we sketch a propagating sound mode in Fig. 1.1, top panel. First, the sketch is an exaggeration, and second, we assumed that we are in the classical limit where atoms behave nicely as particles. We can imagine that this disturbance arose spontaneously, or perhaps it was created when the liquid was struck by a neutron in a scattering experiment. For this disturbance to decay, atoms must move from areas of high density to areas of low density. Therefore, when we

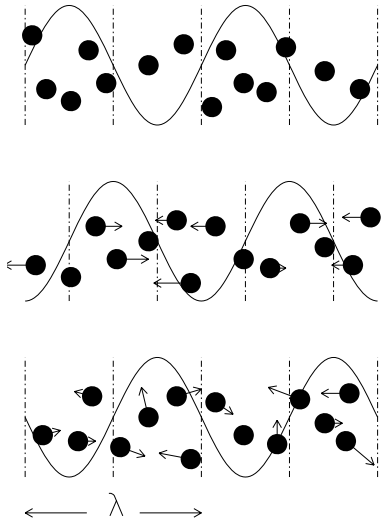

Fig. 1.1 Microscopic density fluctuations

look at the same situation a short time later we find that this density disturbance has created a (longitudinal) velocity disturbance, [Fig 1.1, middle panel]. Another way of saying this is that the density couples to the longitudinal component of the velocity. This velocity disturbance can relax through collisions, but it can also result in a kinetic energy disturbance, or equivalently, a temperature disturbance [Fig. 1.1, bottom panel]. Thus, one can imagine how, on a microscopic scale, various properties associated with the collision between particles contribute to the decay of a density fluctuation.

In normal liquids, a sound wave such as the one sketched in Fig. 1.1 decays rapidly: it can barely propagate for more than half a wavelength before it has decayed. However, in liquid metals, the damping mechanism is not nearly as effective, and sound waves can propagate much further, even the short wavelength sound waves as sketched in the figure. The hypothesis is that the sea of conduction electrons plays a major part in the

diminished amount of damping of the sound waves, diminished compared to simple liquids. The conduction sea becomes a feedback mechanism, reducing the decay rates of density fluctuations such as sound waves. Also, this mechanism seems to permit the sound modes to propagate at a higher velocity than the adiabatic sound velocity, an effect that is observed in virtually all liquid metals. To investigate this hypothesis, a wide range of liquid metals has been studied over the years by means of neutron and x-ray scattering experiments, as well as through molecular dynamics (MD) simulations.

Other than the above mentioned changes to the sound modes in a liquid metal, it was found that liquid metals at first sight behave similar to ordinary liquids on a microscopic scale. Ions diffuse just like uncharged atoms do according to the predictions of Brownian motion. On very short time scales, one can see the effects that the surrounding ions play on the motion of an individual ion/atom. A liquid particle is locked up in a cage formed by its neighbors, and it takes a couple of collisions before it can "escape" its neighbors. This effect is referred to as cage diffusion.

In order to understand how density fluctuations can relax back to equilibrium, one must understand the details of this cage-diffusion process. If an excess of density is present somewhere in the liquid, then this will give rise to pressure waves (that is, to the aforementioned propagating sound modes), as well as to an leveling out of the local density excess through diffusive motions. While it has been known for a while that these pressure waves travel faster than their counterparts in simple liquids, and that they can travel further, it was only recently discovered that the diffusive parts of the motion associated with single ions also showed some unexpected differences when compared to ordinary fluids. The latter has only been noticed relatively recently

because the differences in diffusion mechanisms between normal liquids and liquid metals are present in scattering processes that have a very small cross-section; hence, one had to wait until more powerful neutron and x-ray sources became available.

While the differences in the diffusion mechanism between simple liquids and liquid metals might seem only fairly minor (to be detailed in the following paragraphs) and hardly worth investigating in such detail as is done in this thesis, these differences turned out to present a complete departure from the hydrodynamic behavior that should be valid in all liquids, irrespective of whether they are made up of charged ions or of uncharged atoms.

Hydrodynamics describes the fate of a large scale density fluctuation in a liquid or gas. For instance, when clapping ones' hands, sound waves will propagate away, and the energy that is associated with these sound waves decreases linearly with the frequency of the sound. At the very longest wavelengths (or equivalently, at the lowest frequencies), the energy of these sound waves approaches zero.

The diffusion processes can also easily be pictured on large length scales. On the one hand there is collective diffusion. In words, a local increase in particle number will lead to higher local speeds and, therefore, to more particles leaving the region. In equations, if we have a local increase in the number of particles near a position r at time t, $\Delta\rho(r,t) = \rho(r,t) - \rho_{eq}$, then the density ρ will even out if more particles are leaving this region than are coming in. In other words, $\partial/\partial t[\rho(r,t)] \sim \bigtriangledown v(r,t)$, with $v(r,t)$ the velocity of the region near r at time t. However, for the velocity to be non-zero in the first place, there must have been a gradient in the density: $v(r,t) \sim \bigtriangledown\rho(r,t)$. Combining, we find: $\partial/\partial t[\rho(r,t)] \sim \bigtriangledown^2\rho(r,t)$. The constant of proportionality is called

the diffusion constant D, and the equation $\partial/\partial t[\rho(r,t)] = D \bigtriangledown^2 \rho(r,t)$ is known as Fick's law.

In the above diffusion process, the original particles that caused the increase in density do not necessarily have to make it to the other side of the room, hence the name collective diffusion. When particles do make it to the other side of the room, this process is called self-diffusion. An example of this self-diffusion process on a large scale is opening a bottle of perfume and waiting for the smelly molecules to actually reach the other end of the room. The quicker this happens, the larger the coefficient of self-diffusion D_s.

The above processes exhaust what we can expect to observe on a large length scale. When probing such large length scales, encompassing thousands of molecules and thousands of collisions, one should not directly observe the cage diffusion motion associated with a single atom trying to escape the cage of its neighbors, rather one should observe the indirect effects of atoms being trapped as a fairly small value of the self-diffusion coefficient. Yet paradoxically, in liquid metals one seems to directly observe the motion of individual atoms, even when probing the system on hydrodynamic length scales: neutron scattering experiments revealed the existence of a mode, separate from the standard hydrodynamic modes, associated with the very rapid motion of individual ions. If true, this would represent a breakdown of the laws of hydrodynamics. While the overall cross-section for this new mode is small compared to that of the standard hydrodynamics modes, the relative discrepancies are quite startling: the new mode had an intensity 50 times larger than what could be expected based on Molecular Dynamics computer simulations [1].

The first part of this thesis is devoted to the investigation of this new (and unwanted) contribution to the hydrodynamics of liquid metals. We present a literature review of published experiments to verify the presence of this new mode in liquid metals, followed by a possible explanation for its presence in terms of collision-induced magnetism. Next, we present a series of neutron scattering experiments investigating whether a magnetic contribution is present or absent in liquid gallium. We find that despite various neutron scattering experiments pointing to its existence, there is no such contribution present in Ga, but rather that the additional mode should be attributed to multiple scattering processes. At the same time, these experiments strongly indicate that the new contribution is not due to multiple scattering effects in liquid Hg and Pb, lending credence to the notion that paramagnetic metals can indeed sustain short lived magnetic moments that are brought about by inter-ionic collisions.

In the last chapters of the thesis we investigate the potential effects of quantum mechanical diffraction effects on the collision between two ions. The reason for this investigation is that liquid Ga appears to behave quite differently from the heavier liquid metals like Hg. While inter-ionic collisions in liquid Hg are very similar to collisions between uncharged atoms, recent experiments by Scopigno *et al.* [2] suggest that in liquid Ga, one can see the precursor to the type of bonding that occurs in the solid phase. We investigated whether this is indeed the case, or whether the appearance of such a precursor is in fact due to remnant quantum effects.

To carry out the latter investigation, we solved the collision between two almost classical particles using the partial wave method. The basic idea is that according to quantum mechanics, there is the possibility of particles diffracting around each

other, a process that should influence the cage-diffusion mechanism. We calculated the importance of this diffraction mechanism in liquid metals like lithium, aluminum, sodium and gallium, and we present their influence on the neutron scattering cross-section when measuring the collision between two ions; that is, when doing neutron scattering experiments at high momentum transfers.

The outline of the thesis follows as thus: In Chapter 2, we present the neutron scattering technique, both for polarized and unpolarized neutron scattering, as it pertains to liquid metals, and we discuss how various contributions to the decay of density fluctuations should show up in the angle-dependent cross-section. In Chapter 3, we re-interpret literature data on liquid metals to show the ubiquity of an additional mode to the hydrodynamical regime, and we introduce our model for a collision induced magnetic moment. In Chapter 4, we detail neutron scattering experiments we performed at the Missouri Research reactor MURR and at the Canadian Center for Neutron Scattering on liquid gallium. Chapter 5 is devoted to the data analysis of these experiments, focusing on multiple scattering corrections, followed by our conclusions regarding the presence of a magnetic contribution to the neutron scattering cross-section in liquid metals.

In Chapter 6, we discuss the partial wave method that we employ to solve the collision between two ions, and in Chapter 7 we present the results of this method when applied to various liquid metals. We end with a summary/outlook chapter.

2
Scattering Theory

2.1 Basic neutron properties

The neutron has many properties that make it ideal for scattering experiments. First, the momentum of the neutron is such that the associated de Broglie wavelength ($\lambda_{deB} = h/(2m_nE)^{1/2}$) is of the same order of the interatomic spacing in both liquids and solids. The ensuing coherent interference effects resulting from the neutron being scattered by the ions in the sample give information on the structure of the sample. Second, the neutron is an uncharged particle, so it can penetrate far into the sample before it is scattered or absorbed. This property is essential for probing samples with a large atomic mass that cannot easily be measured using x-ray scattering, where the scattering is so strong that essentially the surface properties are being measured. Also, since the neutron is not scattered by *paired* electrons nor conduction electrons in the sample, but rather by the nucleus via the strong nuclear force, the nuclear scattering gives information about the relative positions of the atoms in the sample instead of information about the extent of the electron cloud. Third, scattering experiments in which the neutron transfers energy to the sample yield information on the elementary excitations of the system.

In addition, the neutron has a magnetic moment. Because of this magnetic moment, a neutron spin scatters from *unpaired* electrons in magnetic atoms. As a result, mag-

netic elastic scattering experiments yield information about the density distribution of unpaired electrons as well as the arrangement of electron spins. Magnetic inelastic scattering experiments reveal the magnetic excitations leading to information on time-dependent spin correlations. In general, the magnetic and nuclear cross-sections for the neutron being scattered by a sample are of the same order of magnitude.

2.2 Graphical representation of neutron scattering

This section illustrates how neutron scattering reveals the basic quantities of interest, specifically, how a neutron can be used to map out the sound wave dispersion, how it gives information about both collective and self-diffusion phenomena, and how it can be used to probe paramagnetic scattering by liquids. The subsequent section provides the basic equations as they pertain to liquid metals, but in this section we give a graphical illustration of the scattering mechanism and the relevant cross-sections in liquid metals.

Neutron scattering is an interference technique. What is observed in scattering experiments is the interference pattern between the incident neutron and the scattered neutron. Thus, use of the wave properties of a neutron make it possible to understand how it can "see" multiple atoms at the same time, revealing their spatial arrangement.

A neutron impinging upon the sample can be represented by a plane wave, with its wavelength λ given by its momentum p: $\lambda = h/p$. This incident plane wave will scatter from the atomic nuclei that make up the sample, as shown in Fig. 2.1. The outgoing neutron, consisting of a superposition of scattered waves, will be detected far away from the sample. A neutron has a good chance of being detected in a direction where these scattered waves interfere constructively, and a very low chance in the direction

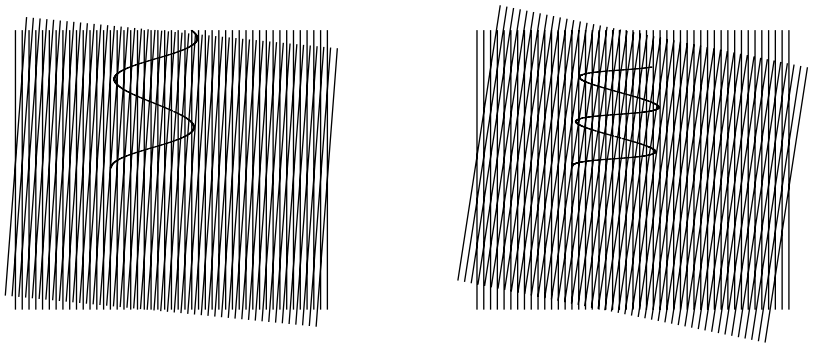

Fig. 2.1 Scattering consists of an incoming plane wave and an outgoing plane wave. The wavelength associated with the plane waves is given by the distance between the vertical lines, the wave crests. The incoming (moving from left to right, also from left to right) and outgoing (moving at an angle) plane waves give rise to an interference pattern that shows up as the white, almost horizontal lines. The distance between successive white lines corresponds to the probing wavelength, which has been plotted in the figure as the sinusoidal shape. The probing wavelength depends both on the wavelength of the plane waves and on the scattering angle. The latter is illustrated in the figure by comparing a scattering angle of 5^o (left half of figure) and 10^o (right half).

where those scattered waves interfere destructively. By the time the outgoing neutron is detected, it is so far from the scattering centra that it can, once again, be represented by a plane wave. This outgoing plane wave is shown in Fig. 2.1.

From Fig. 2.1 we can determine what spatial arrangement of the atoms would give rise to constructive interference in a particular direction. In this figure the areas of the sample that correspond to equal path differences, or integer multiples thereof, show up as white bands. Atoms that are located within these white bands, as shown in Fig. 2.2, interact with the neutron through the strong nuclear force and would all give scattered waves with identical phases, leading to strong constructive interference. If there is no one-to-one correspondence between the atomic positions and the white bands, then there would be destructive interference. The distance between the white bands corresponds to the probing wavelength λ_{probe}, which depends on both the incident

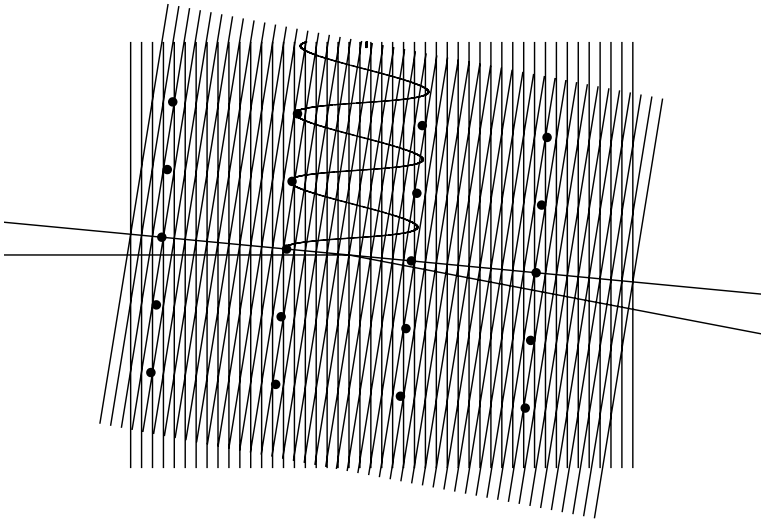

Fig. 2.2 When the interference pattern produced by the incoming wave and outgoing wave corresponds to a natural distance in the sample, there is constructive interference. If the probing wavelength λ_{probe} exactly matches the lattice spacing d, and if the sample is oriented in just the right way as shown in the figure, then the scattering process depicted might actually occur, and a detector placed in the direction of the outgoing wave can detect a scattered neutron (or photon in x-ray scattering).

wavelength of the neutron λ and the scattering angle 2θ.

In fact, Fig. 2.2 corresponds to Bragg scattering by a single crystal, and it gives rise to Bragg peaks in the diffraction pattern. That is, one will only observe scattered particles at very well defined scattering angles. In the case of liquids, constructive interference may still occur; however, the condition for constructive interference will become fuzzier, resulting in smeared-out peaks. Scattered particles will likely be found at most angles, but there will still be angular ranges with more scattered particles found than average. This represents the structure in a liquid that arises from the fact that liquid particles do not sit on top of each other.

In liquids, at very small scattering angles there are very few scattered neutrons. The

reason for this can be seen by inspecting Fig. 2.1. Small scattering angles correspond to large probing wavelengths; however, the distances between the white ridges would correspond to many times the average atomic separation in liquids. Hence, there will not be any correlation in position between them. Therefore, the neutrons scattered by these different regions in the liquid will not be in phase. There is a roughly equal chance that they will be in phase or out of phase. As a result, there is not constructive interference at low scattering angles, and we detect very few neutrons.

At the other extreme, if λ_{probe} corresponds to the average distance between the atoms in the liquid, then there will be a fair bit of constructive interference, it is expected that quite a few neutrons will be scattered at the corresponding angle. Finally, if the probing wavelength becomes much smaller than the interatomic spacings, then only interference stemming from the scattered waves of one atom will be observed. The neutrons observed at the corresponding scattering angles will now yield information about the behavior of single atoms.

The above is summarized in Fig 2.3. The solid, oscillating line is the static structure factor $S(q)$ of liquid mercury. q is a measure of how much momentum p is transferred to the liquid by the neutron, and it is directly related to the probing wavelength: $\hbar q = p = h/\lambda_{probe}$. At large λ_{probe} (small q) there is very little possibility of constructive interference, and $S(q)$ is close to zero. When $\lambda_{probe} \approx d_{average}$, with $d_{average}$ the average separation between the atoms, then more constructive interference occurs than average, and we observe a peak in $S(q)$. For dense liquids such as mercury, peaks also correspond to the next nearest neighbor distances. For very small λ_{probe} (large q), the scattering effects from a single atom are observed, and $S(q)$ will reach a constant

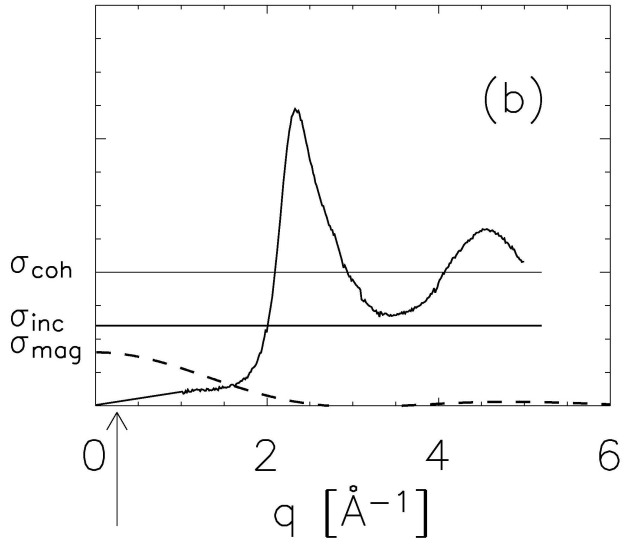

Fig. 2.3 Schematic representation of the components that make up the scattering by a liquid as a function of (reduced) momentum transfer $q = 2\pi/\lambda_{probe}$: the incoherent, the magnetic, and the coherent contributions. The relative strength of the three contributions depends on the momentum transfer and the element-dependent cross-sections $\sigma_{coherent}$, $\sigma_{incoherent}$ and $\sigma_{magnetic}$.

value that depends on how strongly a neutron scatters by a single atom. The measure for this, to be detailed in the subsequent sections, is the coherent cross-section σ_{coh}.

As mentioned, the neutron also has a magnetic moment, which gives rise to two additional scattering mechanisms. Most, but not all, nuclei possess an angular momentum, giving rise to scattering through the electromagnetic force. The phase of the scattered neutron depends on the orientation of the nuclear moment. Because the nuclear moments of neighboring atoms do not line up in any pattern at temperatures of interest in liquids, there is no constructive interference from this scattering mechanism. Instead, we only get information about a single atom, independent of the actual probing wavelength. This process is incoherent scattering, and the cross-section for this process (σ_{inc}) is both element and isotope dependent. This scattering mechanism

is shown in Fig. 2.3 by a horizontal line at height σ_{inc}.

The second scattering process arising from the intrinsic angular moment of the neutron is magnetic scattering. If an ion has unpaired electrons, then the total angular moment of such an unpaired electron will interact with the neutron. The strength of this scattering mechanism for unpaired electrons is comparable to the nuclear cross-section. Even for magnetic ions that are not lined up in any way with their neighbors, a strong dependence on λ_{probe} exists, owing to the scattering off of the electron cloud, which is much larger than the size of the nucleus. Therefore, once λ_{probe} becomes comparable to the size of this cloud, we see a diminished scattering cross-section, because neutrons scattered by one side of the cloud are slightly out of phase with neutrons scattered by the opposite side, corresponding to different path differences in the constructive interference requirement. Once λ_{probe} is much smaller than the size of the cloud, constructive interference is no longer possible and the cross-section becomes zero. All this is shown in Fig. 2.3: the magnetic cross-section at very large λ_{probe} is given by σ_{mag} which in turn depends on the size of the electronic angular moment; when λ_{probe} decreases, so does the magnetic scattering cross-section. The overall decrease of the cross-section as a function of q is known as the magnetic form factor, which is the Fourier transform of the shape and size of the electron cloud.

2.2.1 Inelastic scattering

A neutron can also transfer some of its energy to the sample, or even gain some energy from its interaction with the sample. This process, in which the neutron transfers any amount of energy E, is referred to as inelastic neutron scattering, and the information

gained about the liquid in this process is contained in the dynamic structure factor $S(q, E)$. In the graphical depiction of Fig. 2.1 this would correspond to the scattered neutron having a different wavelength from the incoming neutron and to a slight change in the interference pattern. For instance, a neutron can create a sound wave such as the one depicted in Fig. 1.1, provided the probing wavelength matches the wavelength of the sound mode and provided the energy transferred to the liquid corresponds to the energy of the sound wave. Thus, when one measures the likelihood that a neutron scatters while transferring a certain amount of momentum and energy, one finds strong resonances when these amounts correspond to those of sound waves. This is shown in Fig. 2.4.

The process corresponding to collective diffusion [see Chapter 1] presents as resonance centered around $E = 0$. Such lines are referred to as quasi-elastic lines. Because diffusive processes do not have any particular direction, and because they are not propagating, they must be centered around $E = 0$. The width Γ of the resonances gives information about the time scale that these processes persist for according the Heisenberg relation: $\Gamma = 2\pi/\Delta t$.

The incoherent nuclear scattering mechanism and the magnetic scattering mechanism can also be probed as a function of energy transferred. Since these processes are caused by the scattering by a single atom in liquids, we do not find collective behavior such as propagating waves. Rather, they are seen as lines centered around $E = 0$. As before, the width in energy of these somewhat blurry resonances give information about the time scales involved.

Since the cross sections of all three basic scattering mechanisms are independent

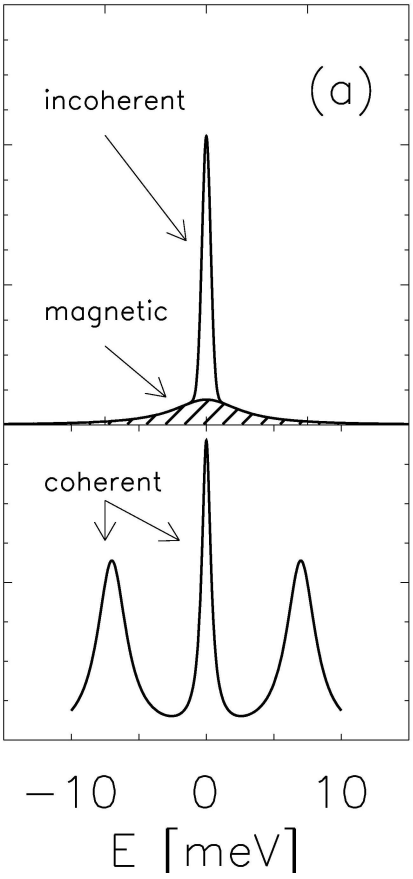

Fig. 2.4 Schematic representation of the components that make up the scattering by a liquid at low q, as a function of energy E transferred by the neutron: the incoherent, the magnetic, and the coherent contributions. The incoherent contribution consists of a sharp central line representing the self-diffusion and a broad central line representing cage diffusion (the cage diffusion mode too small to be seen in the picture: $< 1\%$ of the total intensity). The magnetic contribution shows itself as a broad central line, roughly q independent. The intensity is element dependent, but it is typically of the same order of the coherent contribution. The coherent contribution consists of the Rayleigh-Brillouin triplet at low q. Similar to the incoherent contribution, these three peaks sit on top of a broad cage diffusion mode whose intensity is too small to be visible in the picture.

of each other, the weighted sum of all three is measured. We distinguish the individual processes by their angular dependence, as shown in Fig. 2.1. In addition, coherent scattering can be distinguished from the incoherent and magnetic cross-sections if we also

measure whether the neutron angular moment has flipped or not during the scattering process. The strong nuclear interaction does not affect the neutron's spin, but the incoherent and magnetic scattering processes can affect the spin. This method, called polarized neutron scattering, is actually what was used for our scattering experiments on liquid Ga when investigating whether a magnetic cross-section is present or not. Combining all our knowledge, we find that the likelihood of a neutron being scattered while transferring a certain amount of energy and momentum to the sample is directly proportional to the dynamical processes that take place in the liquid; that is, it is a direct measure of what we want to learn about the liquid. In the next sections we derive the basic equation for the scattering likelihood of a neutron by a liquid made up of identical atoms:

$$\sigma_{total}(q,E) \sim \frac{\sigma_{coh}}{4\pi} S_{coh}(q,E) + \frac{\sigma_{inc}}{4\pi} S_{inc}(q,E) + \frac{\sigma_{mag}}{4\pi} S_{mag}(q,E) \qquad (2.1)$$

First, a quick review of the neutron instrumentation that is used to map out the inelastic scattering is helpful.

2.2.2 Triple axis spectrometer for measuring inelastic scattering

The triple axis spectrometer was invented by B. Brockhouse at Chalk River, Canada. For this, he was awarded the Nobel prize in 1995. The triple axis spectrometer allows the user to measure inelastic scattering events at constant momentum transfer. It derives its name from the three axes of rotation (indicated by the dotted circles in Fig. 2.5) that can be varied during the experiment. The advantage over a time of flight machine is that it is very flexible in setup because every angle can be varied, which allows for easy adjustment of sample parameters such as tilt angles.

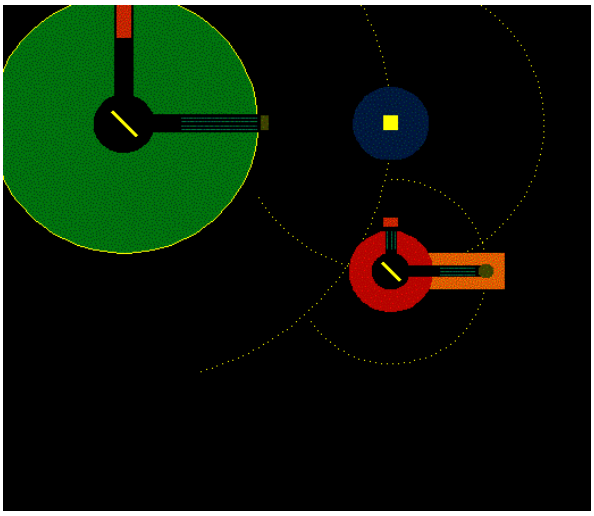

Fig. 2.5 Schematic of a triple-axis spectrometer. The sample table (blue), the analyzer housing (red) and the detector (orange) can all move independently, allowing for precise control of $E = E_i - E_f$, and $q = k_i - k_f$.

One of the disadvantages over a time-of-flight instrument is that the background can vary because of varying degrees of shielding when the arms of the spectrometer are moved during the course of the experiment. Also, in general, the 3-axis spectrometer has only one detector. This is both an advantage and disadvantage. On the one hand, the resolution can easily be fine tuned to the desired accuracy. On the other hand, the count rate can be low. As such, inelastic time-of-flight machines and triple axis spectrometers are often complementary to each other: low-dimensional magnets are best measured on a time of flight spectrometer, whereas three dimensional systems are still best studied on a triple axis.

The incident energy E_i is selected by the monochromator crystal (inside the green drum in the figure), and the final energy E_f is determined by the analyzer crystal (inside the red drum in the figure). The incident and final momentum of the neutron

are determined by both the incident and final energies, as well as by the incoming and final directions of the neutron. A computer programs calculates the appropriate angles corresponding to a scattering event where a certain amount of energy $E = E_i - E_f$ and a certain amount of momentum $q = k_i - k_f$ are transferred to the sample. For the unpolarized scattering experiments described in this thesis we used highly oriented pyrolytic graphite as both our monochromating and analyzing crystals.

By using monochromator and analyzer crystals that only reflect neutrons with a certain spin orientation, one can use a triple axis spectrometer to differentiate between magnetic scattering and nuclear scattering. We used such a setup for the experiments described in Chapter 4.

2.3 Definition of cross-section

In general, scattering is a process where an object (be it a neutron, proton, x-ray, etc.) interacts with another object. Experimentally, a scattering process is studied through the cross-section. The cross-section is a measure of the number of scattering events during the experiment over the whole volume of the scattering region. The value for the cross-section would be sufficient if there were no angular dependence on the scattering, but in general, the scattering from a material has strong angular dependence. It is useful to measure small solid angles to get an idea of the size of the cross-section at a particular angle. If the solid angle is small enough, it could measure a single point in momentum and/or energy. This measurement will give information on the structure of the sample material (e.g., nearest neighbor distance, crystal structure, diffusion time, etc.). This small solid angle measurement is called the differential cross-section [3]. Neglecting spin at this time, the differential cross-section is defined as

$$\frac{d\sigma}{d\Omega} = \frac{N(\theta,\phi)}{\Phi d\Omega} \tag{2.2}$$

for a beam of particles incident on a sample, where $N(\theta,\phi)$ is the number of particles scattered per second into a solid angle $d\Omega$ in the direction (θ,ϕ), Φ is the incident flux (the number of particles through a unit area perpendicular to the incident beam), and $d\Omega$ is the solid angle representing the size of the detector. An equation with the solid angle $d\Omega$ is a better representative of a real-life experiment that can still be treated mathematically. The total scattering cross-section can now be defined as

$$\sigma_{tot} = \frac{N}{\Phi}, \tag{2.3}$$

where N is the number of particles scattered per second. These two equations can be related to one another by:

$$\sigma_{tot} = \int_{\text{all directions}} (\frac{d\sigma}{d\Omega}) d\Omega. \tag{2.4}$$

As an aside, when the system is not dependent on angles (θ, ϕ) (as in the case of incoherent scattering), the total cross-section can be written as

$$\sigma_{total} = 4\pi(\frac{d\sigma}{d\Omega}). \tag{2.5}$$

It is also possible to set up a cross-section describing scattering events in terms of energy. This cross-section is called the partial differential scattering cross-section and is defined as

$$\frac{d^2\sigma}{d\Omega dE'} = \frac{N(\theta,\phi,E)}{\Phi d\Omega dE'}, \tag{2.6}$$

where $N(\theta,\phi,E)$ is the number of particles scattered per second into the solid angle $d\Omega$ in the direction (θ,ϕ) with a final energy between E' and $E'+dE'$. The above equation can be related to Eq. 2.2 (and further to Eq. 2.3) by

$$\frac{d\sigma}{d\Omega} = \int_0^\infty (\frac{d^2\sigma}{d\Omega dE'})dE'. \tag{2.7}$$

The cross-sections are the quantities that are measurable in experiment and can be used to obtain information about properties of the sample. Unless otherwise stated, the scattering particle is limited to the neutron from this point forward.

2.4 Differential cross-section

As the cross-section is the main result of any experiments, a more rigorous definition of the differential cross-section is necessary. As before (Eq. 2.2), the differential cross-section [3] can be rewritten as

$$(\frac{d\sigma}{d\Omega})_{\lambda\to\lambda'} = \frac{1}{\Phi}\frac{1}{d\Omega}\sum_{\mathbf{k}'ind\Omega} W_{\mathbf{k},\lambda\to\mathbf{k}',\lambda'} \tag{2.8}$$

$$= \frac{2\pi}{\hbar}\rho_{\mathbf{k}'}| < \mathbf{k}'\lambda'|V|\mathbf{k}\lambda > |^2 \tag{2.9}$$

with the use of Fermi's Golden Rule (see Appendix A.1), where λ, λ' are the initial and final states of the system, $\Phi = \frac{1}{Volume}\frac{\hbar}{m}k$ is the incident flux of the neutrons, W is the number of transitions per second from $\mathbf{k}$,λ to $\mathbf{k}$',λ', and $\rho_{\mathbf{k}'}$ is the number of momentum states in the solid angle $d\Omega$ per unit energy range for neutrons in a state $\mathbf{k}'$. Here, the notation $(...)_{\lambda\to\lambda'}$ represents the summation of all scattering processes that take the system from λ to λ'. Eq. 2.8 can now be written as

$$(\frac{d\sigma}{d\Omega})_{\lambda\to\lambda'} = \frac{k'}{k}(\frac{m}{2\pi\hbar^2})^2| < \mathbf{k}'\lambda'|V|\mathbf{k}\lambda > |^2 \tag{2.10}$$

with the substitution of the density of states, $\rho_{\mathbf{k}'}$ (see Appendix A.2). With a more specific potential, $V = \sum_j V_j(\mathbf{x}_j)$, where $\mathbf{x}_j$ is the separation distance and $V(\mathbf{x}) =$

$\frac{2\pi\hbar^2}{m}b\delta(\mathbf{x})$ is the Fermi pseudopotential where b is the scattering length, the differential cross-section can be written as (see Appendix A.4)

$$(\frac{d\sigma}{d\Omega})_{\lambda\to\lambda'} = \frac{k'}{k}|\sum_j b_j < \lambda'|e^{i\mathbf{q}\cdot\mathbf{R}_j}|\lambda > |^2, \tag{2.11}$$

where b_j is the scattering length of the j^{th} atom.

2.5 Partial differential cross-section

The partial differential cross-section follows from Eq. 2.10 and conservation of energy. In experiments, the only quantity that changes is the final momentum **k'**, while **k**, λ, and λ' are fixed. This leads to the conservation relation $E + E_\lambda = E' + E_{\lambda'}$, where E and E' are the initial and final energies of the neutron and E_λ and $E_{\lambda'}$ are the initial and final energies of the scattering system. Because the energy conservation can be written as a delta function, the partial differential cross-section is

$$(\frac{d^2\sigma}{d\Omega dE'})_{\lambda\to\lambda'} = \frac{k'}{k}|\sum_j b_j < \lambda'|e^{i\mathbf{q}\cdot\mathbf{R}_j}|\lambda > |^2\delta(E_\lambda - E_{\lambda'} + E - E'), \tag{2.12}$$

such that

$$\delta(E_\lambda - E_{\lambda'} + E - E') = \frac{1}{2\pi\hbar}\int_{-\infty}^{\infty} e^{i(E_\lambda - E_{\lambda'})t/\hbar}e^{-i\omega t}dt, \tag{2.13}$$

where $\hbar\omega = E - E'$. The partial differential cross-section can be further simplified by changing to the Heisenberg picture, where the operators do not change over time. The Hamiltonian is introduced such that the eigenfunctions are the states λ and λ' with corresponding energies E_λ and $E_{\lambda'}$ for all states (See Appendix B.1), then Eq. 2.12 can be written as

$$\begin{aligned}&(\frac{d^2\sigma}{d\Omega dE'})_{\lambda\to\lambda'}\\ &= \frac{k'}{k}\frac{1}{2\pi\hbar}\sum_{jj'} b_{j'}b_j\int_{-\infty}^{\infty} < \lambda|e^{-i\mathbf{q}\cdot\mathbf{R}_{j'}}|\lambda' >< \lambda'|e^{iHt/\hbar}e^{i\mathbf{q}\cdot\mathbf{R}_j}e^{-iHt/\hbar}|\lambda > e^{-i\omega t}dt.\end{aligned} \tag{2.14}$$

Summing over the final states λ' while keeping the initial states λ fixed and summing over all states (See Appendix B.2) gives

$$\frac{d^2\sigma}{d\Omega dE'} = \frac{k'}{k}\frac{1}{2\pi\hbar}\sum_{jj'} b_{j'}b_j \int_{-\infty}^{\infty} e^{-i\omega t}dt \sum_{\lambda} p_\lambda < \lambda|e^{-i\mathbf{q}\cdot\mathbf{R}_{j'}}e^{iHt/\hbar}e^{i\mathbf{q}\cdot\mathbf{R}_j}e^{-iHt/\hbar}|\lambda >, \tag{2.15}$$

where p_λ is the probability that the system is in a state λ. With the introduction of the Heisenberg time-dependent operator $\hat{R}_j(t)$ (See Appendix B.3) we can now take the thermal average (See Appendix B.4)to rewrite Eq. 2.15 in more familiar terms:

$$\frac{d^2\sigma}{d\Omega dE'} = \frac{k'}{k}\frac{1}{2\pi\hbar}\sum_{jj'} b_{j'}b_j \int_{-\infty}^{\infty} < e^{-i\mathbf{q}\cdot\hat{R}_{j'}(0)}e^{i\mathbf{q}\cdot\hat{R}_j(t)} > e^{-i\omega t}dt. \tag{2.16}$$

Eq. 2.16 shows the benefit of expressing the delta function in energy in terms of an integral. The equation can be seen as the correlation of one particle at time zero with another particle at time t. This equation is a common form for the partial differential cross-section.

2.6 Coherent and incoherent cross-sections

Because the system does not have the same value for the scattering length for each nucleus in the system, there will be an average distribution of scattering lengths. This situation occurs due to small changes in nuclear spin or isotope concentration. So, the average scattering length can be written as $\overline{b_j} = \sum_j f_j b_j$, where f_j is the probability that the value of b_j exists. So, from Eq. 2.16, the partial differential cross-section can be written as

$$\frac{d^2\sigma}{d\Omega dE'} = \frac{k'}{k}\frac{1}{2\pi\hbar}\sum_{jj'} \overline{b_{j'}b_j} \int_{-\infty}^{\infty} < e^{-i\mathbf{q}\cdot\mathbf{R}_{j'}(0)}e^{i\mathbf{q}\cdot\mathbf{R}_j(t)} > e^{-i\omega t}dt. \tag{2.17}$$

Assuming no correlation between the values of the scattering length for different nuclei, the partial differential cross-section can be split into two terms:

$$(\frac{d^2\sigma}{d\Omega dE'})_{coherent} = \frac{\sigma_{coh}}{4\pi}\frac{k'}{k}\frac{1}{2\pi\hbar}\sum_{jj'}\int_{-\infty}^{\infty} < e^{-i\mathbf{q}\cdot\mathbf{R}_{j'}(0)}e^{i\mathbf{q}\cdot\mathbf{R}_j(t)} > e^{-i\omega t}dt \qquad (2.18)$$

$$(\frac{d^2\sigma}{d\Omega dE'})_{incoherent} = \frac{\sigma_{inc}}{4\pi}\frac{k'}{k}\frac{1}{2\pi\hbar}\sum_{j}\int_{-\infty}^{\infty} < e^{-i\mathbf{q}\cdot\mathbf{R}_{j}(0)}e^{i\mathbf{q}\cdot\mathbf{R}_j(t)} > e^{-i\omega t}dt \qquad (2.19)$$

where $\sigma_{coh} = 4\pi(\bar{b})^2$ and $\sigma_{inc} = 4\pi(\overline{b^2} - (\bar{b})^2)$.

The coherent term in the partial differential cross-section gives rise to interference effects as there is a correlation of positions between different nuclei at an initial and final time. These interference effects give information about the structure of the sample as well as information about the collective motion of the atoms (sound waves). The incoherent scattering term only depends on the correlation between the same atom over time, so it does not give coherent interference effects. As there are no coherent interference effects due to incoherent scattering, there is no structure information present. Incoherent scattering is used to study diffusive motion because one atom is studied over time. The ideal system, where there is no incoherent scattering, would be the case if all of the scattering lengths were equal so $\bar{b}^2 = \overline{b^2}$, which would only give the coherent scattering term. The incoherent term is an added to the ideal case in order to simulate a real system.

2.7 Liquids

The liquid phase is interesting in that it does not behave like the simple approximations of the gas or solid phase. While over small time scales, the particles in a liquid behave like free particles, they are still close enough to nearby atoms that there is correlated motion after a very short time. Also, the liquid phase is mobile enough that an approximation for a crystalline solid would not be sufficient either.

At this point we introduce the intermediate function and its Fourier transforms. As there is no angular dependence in liquids, **q** becomes a scalar. Using Eq. 2.18, the intermediate function is

$$I(q,t) = \frac{1}{N}\sum_{jj'} < e^{-iqR_{j'}(0)} e^{iqR_j(t)} > \tag{2.20}$$

where N is the number of nuclei in the scattering system. The Fourier transform of Eq. 2.20 in space is the time-dependent pair-correlation function,

$$G(r,t) = \frac{1}{(2\pi)^3}\int I(q,t)e^{-iqr}dq. \tag{2.21}$$

Likewise, the Fourier transform of Eq. 2.20 in time is the scattering function,

$$S(q,\omega) = \frac{1}{2\pi\hbar}\int I(q,t)e^{-i\omega t}dt. \tag{2.22}$$

The scattering function is the quantity measured in experiments. Going back to the coherent partial differential cross-section (Eq. 2.18), the equation can be simplified to

$$(\frac{d^2\sigma}{d\Omega dE'})_{coherent} = \frac{\sigma_{coh}}{4\pi}\frac{k'}{k}NS(q,\omega). \tag{2.23}$$

Important to note is that the scattering function is proportional to the partial differential cross-section, so the calculations are a bit easier. From a similar argument the incoherent partial differential cross-section is

$$(\frac{d^2\sigma}{d\Omega dE'})_{inc} = \frac{\sigma_{inc}}{4\pi}\frac{k'}{k}NS_i(q,\omega), \tag{2.24}$$

where $S_i(q,\omega)$ is the incoherent scattering function:

$$S_i(q,\omega) = \frac{1}{2\pi\hbar}\int I_s(q,t)e^{-i\omega t}dt, \tag{2.25}$$

where $I_s(q,t)$ is the self-intermediate function. This function represents the correlation that one particle has with itself and is written as

$$I_s(q,t) = \frac{1}{N}\sum_j < e^{-iqR_j(0)} e^{iqR_j(t)} > . \tag{2.26}$$

Now we can complete Eq. 2.1 by introducing magnetism. We can write Eq. 2.10 to include a spin-state σ (not to be confused with the cross-section), as:

$$(\frac{d\sigma}{d\Omega})_{\sigma\lambda\to\sigma'\lambda'} = \frac{k'}{k}(\frac{m}{2\pi\hbar^2})^2 | < \mathbf{k}'\sigma'\lambda'|V|\mathbf{k}\sigma\lambda > |^2. \tag{2.27}$$

By evaluating the bra-ket term for the spin and orbital parts separately in the above equation and applying the dipole approximation, then using the fact that what we want is a paramagnetic contribution (no spin correlation between different ions), we get [3]:

$$\frac{d\sigma^{magnetic}}{d\Omega} = n\frac{2}{3}(\gamma r_0)^2[\frac{1}{2}g(LJS)F(q)]^2 e^{-2W(q)} J(J+1), \tag{2.28}$$

where n is the fraction of the ions that have a collision induced angular momentum hJ, $g(LJS) = 3/2 + [S(S+1) - L(L+1)]/[2J(J+1)]$ describes how the intrinsic angular momentum of the electron hS and its orbital angular momentum hL add up to the magnetic moment $\mu_B g(LJS)J$ (μ_B is one Bohr magneton), $F(q)$ is the magnetic form factor, $W(q)$ is the Debye-Waller factor, and $(\gamma r_0)^2$=0.291 barn is the strength of the interaction with the neutron. So, integrating over all angles

$$\sigma_{mag} = 4\pi n\frac{2}{3}(\gamma r_0)^2[\frac{1}{2}g(LJS)F(q)]^2 e^{-2W(q)} J(J+1). \tag{2.29}$$

Both the magnetic form factor and the Debye-Waller factor fall off as $q \to \infty$, so σ_{mag} is only present as low q, unlike incoherent scattering, which is independent of q.

3
Unexplained broad mode in liquid metals

As mentioned in the introductory chapter, neutron scattering experiments on liquid metals do show evidence for a mode in the excitation spectra at low momentum transfer that violates the hydrodynamical predictions. This mode was first noticed by Badyal *et al.* [4] in inelastic neutron scattering experiments on liquid mercury under ambient conditions. Here, we look at the existence and strength of this additional contribution in various liquid metals, and we describe the proposed magnetic scattering mechanism in a diamagnetic metal to explain its existence. This chapter is *reproduced* from Patty *et al.* [5].

3.1 Introduction

During the past decades the properties of a range of elemental liquid metals have been studied by means of neutron scattering [1,4,7,10,11,13–21,24–26,28–31,33,36–38,40,41] and X-ray scattering experiments [2, 8, 9, 12, 22, 23, 27, 32, 34, 35, 39]. Unlike ordinary simple fluids, liquid metals can support short-wavelength sound waves far outside the hydrodynamic regime; simple fluids only support very strongly damped density fluctuations beyond the hydrodynamic region [6]. In other words, a density disturbance decays much faster in a simple fluid than it does in a liquid metal under comparable thermodynamic conditions. Typically, a short-wavelength sound wave in a simple

liquid does not propagate beyond one wavelength [6]. Presumably, this difference can be attributed to the presence of two interacting systems in a liquid metal: the positively charged ionic liquid and the negatively charged conduction sea. This notion has stimulated the study of the decay mechanism of the density fluctuations, by means of neutron and X-ray scattering experiments, as well as by molecular dynamics (MD) computer simulations in a range of liquid metals, such as Hg [1, 4, 7–9], Cs [10–12], K [13–15], Rb [16,17], Na [18–23], Li [24–27], Pb [28–32], Al [33–35], and Ga [2,36–39]. These studies have, by and large, confirmed the role of the electron sea as a feedback mechanism, serving to reduce the decay rates of disturbances and ensuring that density fluctuations can propagate at a higher velocity than the adiabatic sound velocity.

These studies also showed that similar to ordinary liquids, cage diffusion plays an important part in the decay mechanism of density fluctuations [6, 7, 42–45]. Cage diffusion occurs when an atom bounces off neighboring atoms, thereby confining the atom to a "cage." This is in contrast to self-diffusion, the process in which the atom moves through the sample and which is characterized by a net displacement from its starting position over a period of time [6]. In MD simulations, where one follows the position of an atom over time, cage-diffusion and self-diffusion show up as two distinct time scales [1]. Cage-diffusion accounts for a small decrease in correlation between the initial and subsequent position of an atom; this initial decrease in correlation occurs within a few picoseconds. The overall demise of correlation is given by the self-diffusion process, which takes place on a much longer time scale [6] and is determined by the coefficient for self-diffusion D_s. These two diffusive processes can also be observed by means of quasi-elastic neutron scattering [4]. Neutron scattering is sensitive to the

motion of individual atoms because an atom moves during the time it takes the neutron to interact with it [3]. This motion shows itself as a spread in energy of the scattered neutron wave-packet. Rapid movement (cage-diffusion) results in a large spread in energy; slow movement (self-diffusion) results in a spread with small characteristic energy-width. Both processes have indeed been observed in liquid metals. For instance, in liquid mercury [1,4,7], the scattered neutron intensity originating from a single atom (the so-called incoherent scattering contribution [3]) corresponds to a superposition of two Lorentzian lines. One line is sharp (in energy), corresponding to self-diffusion, and one line is broad, corresponding to cage-diffusion. A Lorentzian line in energy corresponds to an exponential decay in time [3] of the correlation between the initial and subsequent position of an atom.

A comparison between the neutron scattering data and the MD simulations on liquid Hg revealed a serious discrepancy regarding the effectiveness of the cage-diffusion mechanism [1, 4, 7]. While both studies agreed on the characteristic time scale for the cage-diffusion process, according to the neutron scattering study [4] cage diffusion accounted for up to 20% of the loss in correlation in the position of an atom, compared to only 0.4% as observed in the MD results [7]. In order to explain this discrepancy, Badyal *et al.* [4] suggested that a mercury ion might have a fluctuating magnetic moment, resulting in an enhanced neutron scattering cross-section. The idea here is straightforward (see Fig. 3.1): in a liquid, atoms can approach each other very closely. On such a close approach, an electron from a filled inner shell of the metallic ion can be ejected into the Fermi-sea (Fig. 3.1.b), resulting in an unpaired electron, and hence in a magnetic moment (Fig. 3.1.c). Once the ions move away from each other again, the

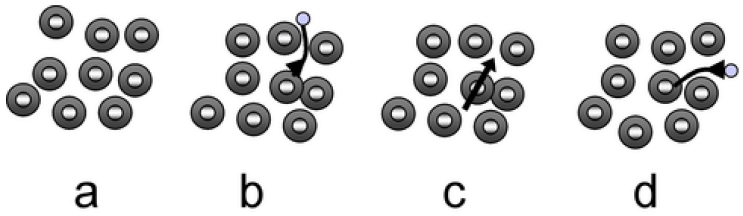

Fig. 3.1 Schematic representation of how cage diffusion can lead to short-lived, fluctuating magnetic moments. (a) A metallic liquid with ions showing completely filled shells. The Fermi sea is not shown. (b) On close approach of two ions, an electron is ejected out of an orbital. (c) The resulting unpaired electron leads to a magnetic moment. (d) This moment disappears as the ions move away from each other and an electron from the sea is recaptured.

shell can be re-completed (Fig. 3.1.d). One can thus expect a magnetic moment to pop in and out of existence on the same time scale as the rattling motion of an atom inside its cage. This process automatically leads to a pathway for the neutron to scatter from the atom via the electromagnetic force [3], augmenting the interaction via the strong nuclear force and resulting in an enhanced cross section for the cage-diffusion process. From the strength of the magnetic interaction [3], it can then be determined what fraction of the time an ion has an unpaired electron.

In this paper we show that the cage-diffusion process in liquid metals is indeed accompanied by a fluctuating magnetic moment. We do this by revisiting published neutron scattering data on Hg, Cs, K, Rb, Na, Li, Pb, Al, and Ga. We observe a small effect in the alkali metals, but find that the ions in Ga and Hg have unpaired electrons for up to 20% of the time. Not only do these magnetic moments provide an additional means for studying cage-diffusion by means of neutron scattering, they provide an additional long-range interaction mechanism for the ions in the liquid.

3.2 Theory

In this section we briefly review the various contributions that make up the neutron scattering cross section of a liquid. We use the data by Badyal *et al.* [4] on mercury to illustrate the various contributions, and to demonstrate under what conditions one can observe the proposed fluctuating magnetic moments.

A neutron interacts with the nucleus of an atom via the strong nuclear force and with the magnetic moments of electrons present in the system via the electromagnetic force [3]. Thus, the total number of neutrons with initial energy E_i that are scattered every second into a solid angle $\mathrm{d}\Omega$ having final energies between E_f and $E_f + dE$ is given by the double differential cross section and can be separated into a nuclear and a magnetic term [3]:

$$\frac{d^2\sigma_{total}}{d\Omega dE} = \frac{d^2\sigma_{nuclear}}{d\Omega dE} + \frac{d^2\sigma_{magnetic}}{d\Omega dE}. \tag{3.1}$$

For mono-atomic systems, such as the ones considered in this paper, the nuclear contribution for single scattering events is given by

$$\frac{d^2\sigma_{nuclear}}{d\Omega dE} = \frac{k_f}{k_i}\frac{\sigma_{coh}}{4\pi}S_{coh}(q,E) + \frac{k_f}{k_i}\frac{\sigma_{inc}}{4\pi}S_{inc}(q,E) \tag{3.2}$$

$S_{coh}(q,E)$ is the dynamic structure factor and represents the collective response of the liquid as a function of momentum $\hbar q$ and energy E transferred from the neutron to the liquid, while $S_{inc}(q,E)$ describes the dynamics of a single atom [3]. The cross-sections σ_{coh} and σ_{inc} are element dependent; σ_{inc} arises because the strong interaction depends on the spin state of the nucleus and the number of neutrons in the nucleus. Thus, the nuclear scattering cross-section carries information about the collective behavior of the

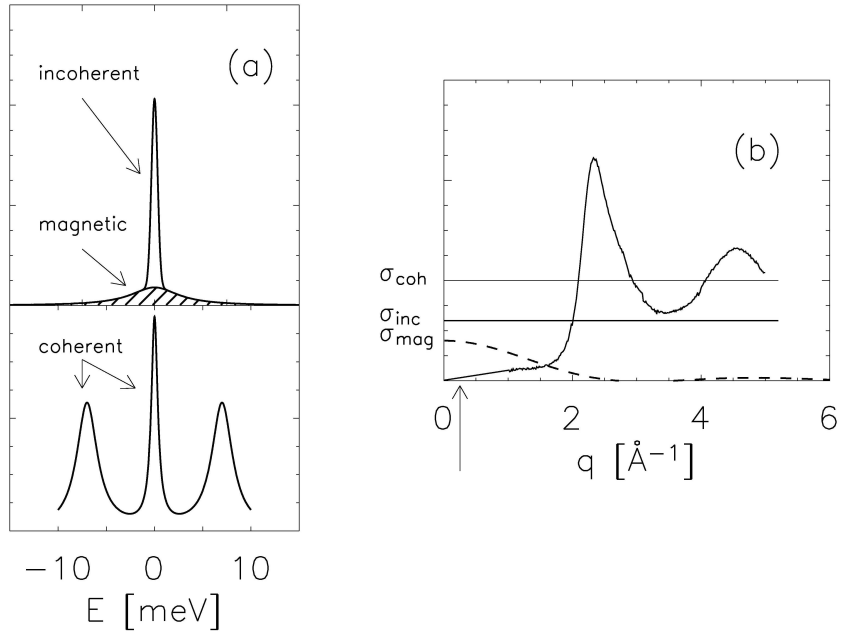

Fig. 3.2 (a) Schematic representation of the components that make up the scattering by a liquid at low q: the incoherent, the magnetic, and the coherent contributions. The incoherent contribution consists of a sharp central line representing the self-diffusion and a broad central line representing cage diffusion (the cage diffusion mode is too small to be seen in the picture: $< 5\%$ of the total intensity). The magnetic contribution shows itself as a broad central line, roughly q independent. The intensity is element dependent, but it is of the same order of the coherent contribution, typically. The coherent contribution consists of the Rayleigh-Brillouin triplet at low q. Similar to the incoherent contribution, these three peaks sit on top of a broad cage diffusion mode whose intensity is too small to be visible in the picture. (b) Schematic depicting the relative strength of the three contributions, which depends on the momentum transfer and the element-dependent cross-sections. The arrow indicates the low q value used in part (a) where the magnetic contribution is most prominent [48].

atoms, such as sound waves, and information about the motion of individual atoms, such as self-diffusion.

The static structure factor $S(q)$ is given by the sum-rule [3]

$$S(q) = \int S_{coh}(q, E) dE, \tag{3.3}$$

while the incoherent dynamic structure factor satisfies a similar sum-rule

$$1 = \int S_{inc}(q, E) dE. \tag{3.4}$$

The various contributions are illustrated in Fig. [3.2]. In neutron diffraction experiments aimed at measuring $S(q)$, the energy integration in Eq. 3.3 is carried out by the neutron detector. Because of the term k_f/k_i in Eq. 3.2, this procedure leads to small errors in the determination of $S(q)$; however, these errors are small under suitable experimental conditions and can be corrected for using standard methods [3]. A further source of errors is that Eq. 3.2 is only valid for neutrons that are scattered once by the sample. Again, by choosing sufficiently small samples, the errors introduced by multiple scattering events and events in which a scattered neutron is absorbed by the sample can be corrected for [46]. Therefore, provided these corrections have been carried out, one can check the accuracy of the data reduction procedure by comparing the measured cross-sections σ_{coh} and σ_{inc} to the known values. Even in the case where the absolute values of σ_{coh} and σ_{inc} cannot be inferred from the experiment, their ratio can still be determined using the fact that $S(q)$ oscillates around 1 for large q.

The magnetic contribution to the scattered intensity is only visible in neutron scattering experiments on liquids provided that atoms with unpaired electrons exist [3]. The angular momentum associated with these unpaired electrons, hJ, interacts with the intrinsic magnetic moment of the neutron. The conduction electrons present in liquid metals do not contribute to the scattering at finite q; an electron moves so fast compared to the neutron that the scattered waves only add up coherently at q=0, the forward direction. However, if an electron is localized around an atom, all scattered waves originate from the region of the partially filled orbital, and the scattered waves

can be observed for a range of q-values. For this reason the form factor for magnetic scattering $F(q)$, which describes the variation of scattered intensity with q and which is given by the spatial extent of the electron cloud, falls off more rapidly with increasing q than the form factor for nuclear scattering [the so-called Debye-Waller factor $W(q)$]. The latter reflects the fact that nuclear scattering originates in the much smaller volume of the nucleus.

The number of ions with unpaired electrons at any given moment determines the magnetic cross-section for a liquid with fluctuating magnetic moments. The total number of neutrons that are scattered per second per metallic ion into solid angle dΩ is given by the paramagnetic approximation for the differential cross section [3]

$$\frac{d\sigma^{magnetic}}{d\Omega} = n\frac{2}{3}(\gamma r_0)^2[\frac{1}{2}g(LJS)F(q)]^2 e^{-2W(q)}J(J+1). \tag{3.5}$$

In this equation, n is the fraction of the ions that have a collision induced angular momentum hJ, $g(LJS) = 3/2 + [S(S+1) - L(L+1)]/[2J(J+1)]$ describes how the intrinsic angular momentum of the electron hS and its orbital angular momentum hL add up to the magnetic moment $\mu_B g(LJS)J$ (μ_B is one Bohr magneton), and $(\gamma r_0)^2$=0.291 barn is the strength of the interaction with the neutron. Eq. 3.5 offers a good approximation of the strength of the magnetic scattering provided that the characteristic energy width of the quasi-elastic scattering as determined by the underlying cage-diffusion mechanism is small compared to the incident energy of the neutron [3]. This is the same requirement that allows one to determine $S(q)$ from a liquid without doing an energy analysis of the scattered neutron, and we will therefore assume that this requirement is satisfied for all published datasets discussed in this paper.

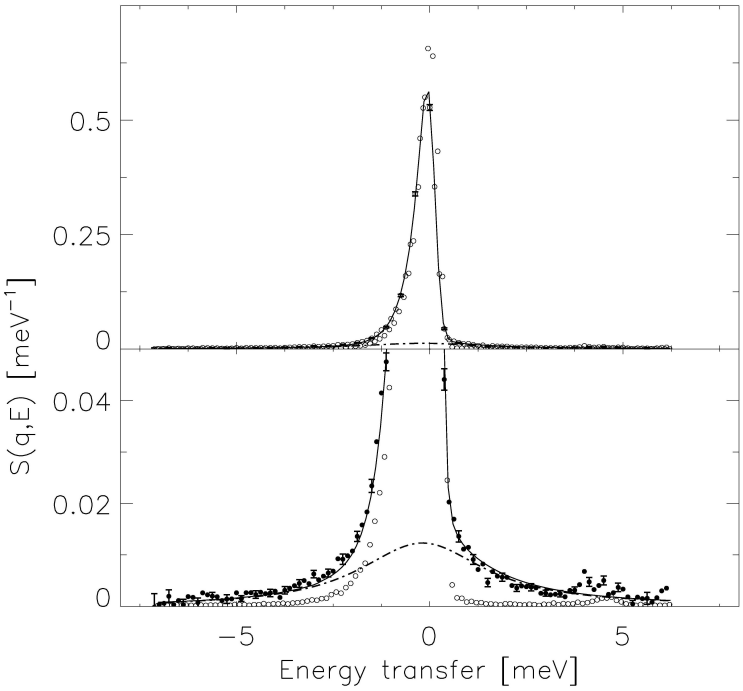

Fig. 3.3 The dynamic structure factor of liquid mercury [4] at small momentum transfer (solid circles) and a vanadium reference sample (open circles) showing the resolution of the neutron scattering spectrometer. The solid line is a fit to two Lorentzian lines, taking the asymmetric spectrometer resolution function into account. The bottom figure is an enhancement of the top figure. One observes a sharp (in energy, hence slow in time) central mode reflecting self-diffusion, and a broad mode (dash-dotted curve) reflecting the fast rattling motion of an atom inside the cage formed by its neighbors. The intensity of this broad mode (clearly absent in the vanadium spectra) was found to be larger [4] by a factor of 20 than could be expected from nuclear sum rules on the scattering. Hence, the intensity was attributed to a paramagnetic cross section, reflecting an unpaired *d* electron on a time scale determined by cage diffusion. (Figure reproduced from Ref. [4]).

Analyzing quasi-elastic neutron scattering experiments on liquid Hg at room temperature, Badyal *et al.* [4] observed that the scattered signal at small momentum transfers consisted of two contributions (see Figs. 3.2 and 3.3), attributable to self-diffusion and cage-diffusion, respectively. However, the relative strength (area under the curves in Fig. 3.3) of the cage-diffusion contribution compared to the self-diffusion

contribution was found to be 22% (corresponding to a differential cross section of $\sim 1.5/4\pi$ barn). A relative strength of the order of 0.3% was expected based on MD simulations [7] and on an order of magnitude calculation [4]. Given that the strength of the quasi-elastic coherent contribution for small q-values (given by sum-rules at $\sim 0.01/4\pi$ barn) was negligible [3, 47], and given that the characteristic energy width (3 ps^{-1}) corresponded to the time scale of the cage diffusion process (1/3 ps), the authors [4] concluded that the broad quasi-elastic line did indeed correspond to cage-diffusion but with a magnetically enhanced cross-section (depicted in Fig. 3.2). Using Eq. 3.5 (S= 1/2, L=2 and J=5/2 and $F(q)$=$e^{-W(q)}$= 1 for small q) and noting that crystal electric field effects are absent in a liquid, we find that 20% of the Hg-ions have an unpaired d-electron. Should the observed magnetic signal originate from an unpaired s-electron, then the corresponding fraction of magnetic ions would be 82%. We return to this latter possibility in the discussion.

Thus, a significant fraction of the mercury ions has a magnetic moment; this moment can interact with its neighbors via the magnetic dipole interaction, via the direct exchange interaction, and via polarization of the conduction electrons. The dipole interaction likely only adds up to a small correction to the interatomic potential at small distances, but it becomes the dominant interaction mechanism at large distances; therefore, it might well contribute to the ability of a liquid metal to sustain propagating soundwaves with short wavelengths. Likewise, the polarization of the conduction electrons by the atomic magnetic moments provides a direct interaction mechanism between the ionic liquid and the conduction electrons. It is the presence of the two interacting systems that is presumably responsible for the existence of well-defined

Table 3.1 The observed magnetic cross-section σ_{magn} and the corresponding fraction n of ions with a magnetic moment, calculated for the most likely quantum numbers of the unpaired electron using Eq. 3.5.

Element	$T/T_{melting}$	S	L	J	$g(LJS)$	σ_{magn} [b]	n [%]	Ref.
Li	1.03	1/2	0	1/2	2	0-0.01	0-1	[24]
Al	1.003	1/2	0	1/2	2	0.16	9	[33]
		1/2	1	3/2	1.33		4	
Ga	1.08	1/2	0	1/2	2	0.4	22	[37]
		1/2	2	5/2	1.2		5.2	
	1.08	1/2	0	1/2	2	0.88	48	[36]
		1/2	2	5/2	1.2		12	
	3.17	1/2	0	1/2	2	0.78	42	[36]
		1/2	2	5/2	1.2		10	
	3.20	1/2	0	1/2	2	0.5	27	[37]
		1/2	2	5/2	1.2		6.5	
Cs	1.02	1/2	1	3/2	1.33	0.11	2.7	[10]
Hg	1.25	1/2	0	1/2	2	1.5	82	[4]
		1/2	2	5/2	1.2		20	
Pb	1.02	1/2	0	1/2	2	0.7	38	[31]
		1/2	2	5/2	1.2		9	

short wavelength sound waves. For this reason, we have re-analyzed existing neutron scattering data [10, 13, 24, 31, 33, 36, 37] on liquid metals in order to investigate the presence of magnetic moments in non-magnetic liquids. We note that short-lived magnetic moments do not contradict the overall diamagnetic response of a liquid metal: macroscopic measurements take place on a much larger time scale than the lifetime of a collision-induced atomic moment.

Fluctuating magnetic moments can betray their presence in various ways in neutron scattering experiments. In diffraction experiments the additional cross-section would lead to an increased signal at smaller q-values, decaying with q according to $|F(q)|^2$. This additional signal would be on top of the angle independent incoherent cross-section and the weakly angle dependent multiple scattering cross-section.

Thus, whether the proposed signal is actually visible in published data depends on the strength of the incoherent cross section and on the details of the data reduction procedure. It is easiest to identify the magnetic cross section in quasi-elastic neutron scattering experiments (as in the liquid mercury experiments [4]); however, we did not find data sets in the literature suited to the latter approach. Finally, it is unclear a priori how an increase in temperature and density would affect the magnetic cross section. This increase would allow for closer approach of the ions thereby increasing the overlap of the filled orbitals; however, the life-times of the induced moments would likely decrease as well resulting in a signal that would be too spread out in energy to be reliably observable in neutron scattering experiments.

3.3 Results

Our investigation is limited to published studies that show the raw data and detail the correction procedure, or to studies where the incoherent scattering contribution is absent. Surprisingly, this leaves very few data sets on liquid metals. In most investigations the data are only presented after subtraction of the contribution identified as incoherent scattering. This subtraction procedure would also have eliminated the magnetic contribution, should it have been present. Evaluation of the published neutron scattering data on the much studied alkali metals shows that the percentage of ions having a magnetic moment is likely to be much smaller than what was observed in liquid mercury. In most cases it is not possible to come to an unambiguous conclusion whether this magnetic contribution is present or not. On the other hand, the group 3 and 4 metals Al, Pb and Ga show a large effect similar to liquid mercury. All results are collected in Table I.

Before discussing the neutron scattering results in detail, we note that inelastic X-ray scattering experiments [2, 8, 9, 12, 22, 23, 27, 32, 34, 35, 39] on a variety of liquid metals do not show evidence for an additional mode. Given the accuracy of recent experiments and the fact that only the coherent contribution is measured in X-ray scattering experiments, this rules out the possibility that any additional mode observed in neutron scattering experiments is part of the coherent scattering (Fig. 3.2). This is as expected from MD simulations [7, 38]: while the decay in correlation due to cage-diffusion is visible in the coherent dynamics as a decline in correlation that happens over a short period of time, its intensity (magnitude of the decline) is so small (< 0.5 % at small q-values [48]) that it cannot be observed as a separate mode in the coherent contribution. Thus, the effects of cage-diffusion can be observed in the *linewidth* of the scattering spectra [35, 39], but cage-diffusion does not show up as a *separate* contribution (mode) to the scattering.

3.3.1 The alkali metals

Bodensteiner et al. [10] observed a discrepancy between the value for the incoherent scattering cross-section as measured in their inelastic neutron scattering experiments on liquid cesium at 308 K and the commonly accepted value. After having accounted for all corrections to the normalization of the neutron scattering data, Bodensteiner *et al.* [10] inferred a (total) incoherent cross section of 0.33 b instead of the literature value of 0.22 b. Assuming that 0.22 b is indeed the correct value for the incoherent cross-section, this would imply a magnetic cross-section of 0.11 b, or $d\sigma^{magnetic}/d\Omega = 0.11/4\pi$. Presumably, a collision would leave a cesium ion temporarily with an

iodine configuration (S=1/2, L=1, J= 3/2 and $g(LJS)$= 4/3), yielding n= 2.7% (see Eq. 3.5). Unfortunately, since uncorrected spectra at the smallest q-values ($q < 0.5$ Å^{-1}) were not published in this study [10], we could not infer whether the supposed magnetic cross section indeed corresponded to a quasi-elastic spectrum characterized by a cage-diffusion linewidth.

From the current literature results, it is inconclusive whether liquid potassium [13–15], liquid rubidium [16, 17], or liquid sodium [2, 18–22] display magnetic cross-sections. Either the data at low q are not accurate enough, or not enough details of the data correction procedure have been given to test our hypothesis. Bearing in mind the results for liquid cesium, the magnetic cross-section of $\sim$ 0.1 b might just be too small to be observable in sodium (σ_{inc} = 1.67 b) and rubidium (σ_{inc} = 0.48 b). However, the paramagnetic cross-section might have been observed in liquid potassium (σ_{inc} = 0.27 b) in a series of quasi-elastic neutron scattering experiments [13]. Cabrillo et al. [13] combined a high (energy) resolution study on liquid K at 343 K with a lower resolution experiment to model the full dynamic response of potassium down to small $q \sim 0.4$ Å^{-1}. Doing so, they were able to show that the quasi-elastic component at small q consisted of two contributions, one corresponding to self-diffusion and one to a process with a lifetime τ $\sim$3 ps. Qualitatively, this is similar to the observations for cage-diffusion in liquid mercury. Unfortunately, the authors did not give the ratio between the narrow and broad component, making it impossible to infer n from their data. In fact, the authors did not attribute this broad mode to cage-diffusion. Instead, it was assumed to be part of the coherent scattering contribution. The latter is inconsistent with their modeling of the rest of the scattered intensity [13],

which already completely exhausted the coherent sum-rule (Eq. 3.3). Given this, and given the very weak dependence of τ on q for $q < 1.3$ Å^{-1}, we believe that this broad mode represents cage-diffusion. However, whether it is a cage-diffusion process combined with a fluctuating magnetic moment cannot be inferred from this study (as published).

Neutron scattering results for liquid lithium leave open the possibility of a magnetic cross-section being present albeit that the results are somewhat inaccurate owing to the large absorbtion cross-section. For instance, Torcini *et al.* [24] report $S(q = 0)$= 0.04 at 450 K, while the expected $S(q = 0)$ from the compressibility sum-rule is 0.03, thus indicating the presence of a small magnetic cross-section. However, not all studies are in agreement with these neutron scattering data (probably due to the large absorbtion cross-section for neutrons). Therefore, we can only give an estimated range for the fraction n of ions with an unpaired electron. Based on the work of Torcini *et al.* [24], we find the fraction n to be in the range $0 < n < 1\%$, for S=1/2, L=0, J=1/2 and $g(LJS)$=2.

In all, the alkali metals do not show unambiguous evidence for the existence of the proposed magnetic cross-section. However, it is interesting to note that small angle x-ray scattering experiments on liquid lithium indicated the presence of an additional cross-section [25], which the authors tentatively attributed to increased correlation between the valence electrons. The mechanism proposed in this paper would offer an explanation for the observed [25] increased correlation. Nonetheless, the evidence for a collision-induced fluctuating moment in the alkali metals is somewhat weak. Much better evidence for its existence comes from scattering experiments on group 3 and

4 metals, which display an enhanced cross-section, similar to the results for liquid mercury.

3.3.2 Group 3 and 4 metals

Liquid lead is a good candidate to analyze for the possible presence of a magnetic cross-section since Pb has a negligible incoherent cross-section; therefore, any significant scattering at small momentum transfers (where the coherent cross-section is very small) is indicative of a paramagnetic signal. Reijers *et al.* [31] measured the static structure factor of liquid lead at 613 K under ambient pressure (see Fig. 3.4). From Eqs. 3.2 and 3.3, we find that the expected neutron scattering intensity at small momentum

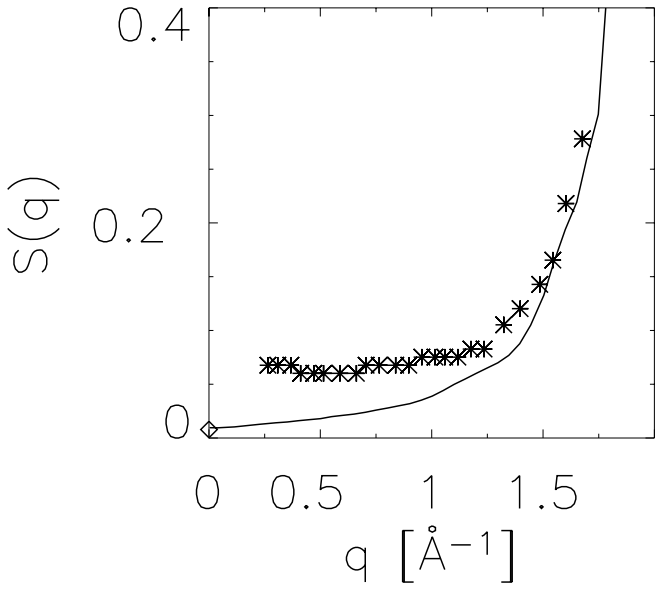

Fig. 3.4 The static structure factor of liquid lead as measured by X-ray scattering data [32] at 623 K (solid line) and neutron scattering data [31] at 613 K (stars). Note the difference between the two data sets at small momentum transfer; the X-ray scattering data approach $S(q = 0) = 0.008$ (open diamond), while the neutron scattering data approach a constant value well in excess of $S(q = 0)$, indicative of a magnetic contribution to the scattering.

transfers due to coherent scattering is given by $\sigma_{coh}/4\pi S(q=0)$, with $S(q=0) =$ 0.009 [49] and σ_{coh}= 11.16 b. The $S(q=0)$ extrapolated value from the liquid lead experiment is 0.07 (see Fig. 3.4), implying an additional neutron scattering intensity of $0.7/4\pi$ b. Using Eq. 3.5 with S= 1/2, L=2, J= 5/2 and $g(LJS)$= 1.2, the fraction n of ions with an unpaired electron is 9%. Assuming the additional cross-section originates from s-electrons (S= 1/2, L=0, J= 1/2 and $g(LJS)$= 2), we find n= 38% (See Table I).

Liquid aluminum also displays a paramagnetic cross-section. Iqbal *et al.* [33] performed a study on liquid aluminum at 936K (see Fig. 3.5). In this study on a liquid with negligible incoherent cross-section, the authors normalized their data to $S(q \rightarrow \infty)$= 1; however, the data had not been corrected for multiple scattering effects, which can constitute a major part of the scattering at small q. Based on the dimensions of their cylindrical cell, we have calculated [4, 46] the multiple scattering contribution (dashed line in Fig. 3.5) assuming the energy dependence of $S(q, E)$ to be given by a Lorentzian line shape with half width determined by the coefficient for self-diffusion (D_s= 0.4 Å^2/ps [50]). After subtracting the multiple scattering contribution and renormalizing the data accordingly, we find that the neutron scattering data consistently lie above the X-ray data [34] at small q, and that the neutron scattering data do not appear to reach the $q \rightarrow 0$ limit S(q=0) = 0.013 [51]. Since a paramagnetic contribution represents a very small correction to X-ray scattering data, we take the difference $\Delta S = 0.11$ between the neutron and X-ray $S(q)$ measurements at $q < 1.5$ Å^{-1} as the strength of the paramagnetic signal, i.e., $d\sigma^{magnetic}/d\Omega = \Delta S\sigma_{coh}/4\pi = 0.16/4\pi$ b. This corresponds (Eq. 3.5) to a fraction n= 4% assuming the fluorine electronic

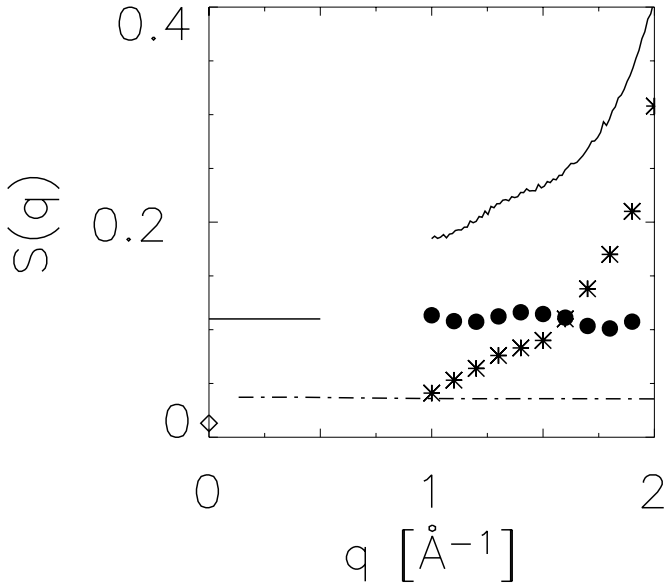

Fig. 3.5 The static structure factor of liquid aluminum just above the melting point as measured by neutron scattering [33] (solid line) and X-ray scattering [34] (stars). The difference between the two data sets is considerably larger than the calculated multiple scattering contribution to the neutron scattering data (dashed-dotted curve). After correcting for these multiple scattering effects, the remaining difference between the two data sets (solid circles and horizontal line) is only weakly dependent on q, indicative of an incompletely filled electronic shell with small radius. The data point at q=0 (open diamond) is the compressibility limit taken from thermodynamic data [51].

configuration for paramagnetic Al-ions; a sodium configuration would correspond to n= 9% (See Table I). Again, very accurate inelastic X-ray scattering experiments on liquid Al [35] did not find evidence for an additional mode (a fourth contribution in addition to the three modes shown in Fig. 3.2), ruling out the possibility that the additional scattering is part of the coherent contribution.

Another liquid metal for which we can verify the presence of an additional component to the cross-section is liquid gallium. In fact, gallium is probably the most compelling case of the ones presented in this paper. Bellissent-Funel *et al.* [36] found in their experiments on liquid Ga at 326 K and 959 K that the observed scattered

intensities were not consistent with the known values for σ_{inc} and σ_{coh}. Since both uncorrected and corrected data were published in this study [36], and since every step of the data reduction procedure was clearly described, we can infer a very accurate estimate of the paramagnetic cross-section for Ga. Using the dimensions of the sample cell used in the experiments [36], we have calculated [4, 46] the multiple scattering contribution (see Fig. 3.6). Taking into account the $S(q = 0)$ values and the fact that the magnetic contribution will be absent at very large q, we find an additional differential scattering cross-section of $0.88/4\pi$ b at 326 K and $0.78/4\pi$ b at 959 K. Assuming this scattering to originate from an unpaired electron with quantum numbers S= 1/2, L=2, J= 5/2 and $g(LJS)$= 1.2, we find n = 12% at T= 326 K and n= 10% at T=959 K. If we assume the scattering to originate from a s-electron (S=1/2, L=0, J= 1/2 and $g(LJS)$= 2), we find n= 48% and n= 42%, respectively (see Table I). Thus, gallium displays a large magnetic cross-section, but its magnitude appears to be only weakly temperature dependent.

More recently, the gallium dynamics have been investigated by means of inelastic neutron scattering [37], inelastic X-ray scattering [2, 39] and molecular dynamics computer simulations [38], allowing us to verify the diffraction-based route and to obtain an independent estimate. The X-ray data, measuring the coherent cross-section, demonstrated that the coherent contribution consists of three peaks (and three peaks only), whose linewidths and relative intensities change as a function of q in a manner that can be modeled using the memory function formalism. Molecular dynamics computer simulations, which were in excellent agreement with the X-ray data [39], showed that the self-dynamics (incoherent scattering) consists of a simple diffusion mode car-

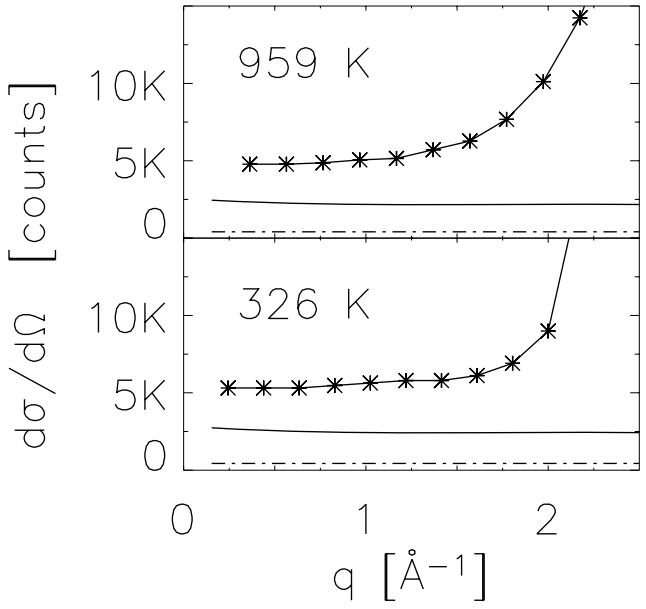

Fig. 3.6 The unnormalized static structure factor of liquid gallium at two temperatures (solid line with stars) as measured by neutron scattering [36]. The calculated incoherent contribution is given by the dash-dotted lines; the sum of the incoherent and multiple scattering contribution (see text) is denoted by the solid lines. The difference (at small q values) between the experimental data points and the solid line is ascribed to paramagnetic scattering.

rying practically all of the intensity (in neutron scattering) at low q (99.6% at q= 0.3 Å^{-1}) plus a cage-diffusion mode (intensity 0.4% at q= 0.3 Å^{-1}) whose importance increases [48] as q^2 for $q < 1$ Å^{-1}.

Interestingly, carefully corrected inelastic neutron experiments clearly showed the presence of a broad mode at q= 0.3 Å^{-1}, whose linewidth corresponded to the expected linewidth for cage-duffusion, but whose intensity was observed to be as much as the intensity of the self-diffusion mode, and easily exceeded that of the two propagating sound modes which carry about 80 % of the intensity of the coherent contribution. Thus, there is a broad mode present in the neutron scattering data, which is not present

in the X-ray scattering data and which exceeds the expected intensity based on simulations by at least two orders of magnitude. We identify this mode as originating from fluctuating magnetic moments on the Ga-ions. We stress that, independent of whether our explanation for this additional intensity stands the test of further experiments or not, the fact remains that there is an additional mode present in liquid gallium, which at small momentum transfers scatters as many neutrons as the known incoherent and coherent scattering mechanisms. This mode is not reproduced in very accurate MD computer simulations. Using the numbers published in Ref. [37] in combination with Fig. 5 in this reference, we can use the strength of the self-diffusion peak to estimate the intensity of the broad quasi-elastic mode. Normalizing to the gallium incoherent cross-section ($\sigma_{inc} = 0.16$ b [52]), we find $\sigma_{magn} = 0.4\pm$ 0.1 b at 320 K and $\sigma_{magn} = 0.5\pm$ 0.1 b at 970 K, below the estimates derived from the diffraction data, but similar in magnitude. These differences likely reflect the accuracy with which the magnetic contribution can be determined based on the diffraction data. The corresponding fraction of magnetic ions are given in Table I. Similar to the case for the diffraction data based estimates, we only observe a weak temperature dependence.

3.4 Discussion

The available neutron scattering data reveal the presence of a broad quasi-elastic mode that is entirely absent in X-ray scattering and which cannot be ascribed to the standard mechanisms for incoherent and coherent scattering. We have argued that this mode is evidence for the existence of short-lived magnetic moments in non-magnetic liquid metals. These moments come in and out of existence on the same time scale as the cage-diffusion motion, as observed in the quasi-elastic neutron scattering experiments

on liquid Hg [1, 4, 7]. The alkali metals show only a weak effect, but the effect is much more pronounced in mercury and in group 3 and 4 metals (see Table I).

The actual percentage of ions with unpaired electrons is more difficult to assess than establishing that such ions with unpaired electrons exist. For instance, it is feasible that the unpaired electron in liquid mercury is either an s-electron or a d-electron. The 6s shell in mercury has been drawn in closer to the nucleus because of the relativistic contraction of the underlying shells, so it is definitely conceivable in a liquid that the 6s shell can be completely filled (for some of the time at least). In other words, the observed paramagnetic intensity could originate from a Hg^{1+} or from a Hg^{3+}-ion. (In liquid lead, it is in fact more likely that the paramagnetic contribution stems from Pb^{3+} than from Pb^{5+}-ions, given the prevalence of lead to form Pb^{2+} in solids.) Should this indeed be the case, then the electrical resistance in liquid mercury does not come solely from electrons being scattered by ions, but also from electrons actually being captured by Hg-ions; far from being unchanging, the Fermi-sea constantly changes in size while interchanging electrons with the ions.

The phenomenon of the additional magnetic cross-section seems to have been mostly overlooked. However, its implications on the interaction mechanisms in a liquid metal cannot be overlooked given the long range of the magnetic dipole interaction and the ability of localized moments to polarize the surrounding conduction electrons. In particular, it would be interesting to see how incorporation of paramagnetic ions and their polarization capability into the interatomic potential used in MD simulations would alter the characteristics of short-wavelength sound propagation.

Finally, this paramagnetic cross-section provides a means of studying the cage-diffusion mechanism at small momentum transfers even in systems that do not exhibit an incoherent cross-section, such as lead and aluminum. In the next chapter we describe polarized neutron scattering experiments on liquid gallium that we carried out in order to investigate whether the observed additional cross-section is indeed magnetic in origin.

4
Experiments at MURR and Chalk River

The results presented in the preceding chapter demonstrate the ubiquity of a low momentum excitation in liquid metals that defies the hydrodynamic sum rules. Here, we investigate whether the broad mode in liquid Ga is of magnetic origin by performing polarized neutron scattering experiments at both the Missouri Research Reactor (MURR) at the University of Missouri and the Canadian Neutron Beam Center at Chalk River. We used a polarized neutron scattering setup since this would allow us to distinguish between magnetic and nuclear scattering, as explained in Chapter 2.

We chose to study gallium out of practical considerations. First, from the results shown in Table 3.1 it is clear that the cross-section of this mode in liquid Ga, being somewhere between 0.4 and 0.8 b, should be sufficiently large to be visible in polarized neutron scattering experiments. Second, Ga melts at room temperature, so the sample environment will be very easy to handle, as opposed to liquid lead. Third, Ga has a low incoherent cross-section, making it much easier to identify any magnetic scattering. Fourth, it is not possible to take liquid mercury into a reactor owing to its easy of vaporization. And finally, Ga is also the odd-one-out in Table 3.1. From the data shown in this table, it looks like the effect increases with increased atomic mass, yet Ga apparently displays a considerable cross-section despite its relative lightness.

4.1 Polarized experiments at MURR

In order to get an indication of whether this mode in Ga corresponded to a magnetic cross-section, we carried out a preliminary polarized experiment at MURR. The experiments were performed using our reflectometer in its polarized setup. This reflectometer operates at constant incident neutron wavelength, while the polarization of the incident beam and polarization analysis of the scattered beam is done by making use of supermirrors. There is no energy analysis of the final neutron energy, rather a detector simply counts all the scattered neutrons. As for the quality of the polarized setup, with the incident and analyzer mirror in place and one flipper placed downstream of the sample position, we found a flipping ratio of 1:7.5. This implies that 1 in 7.5 neutrons that will be detected as corresponding to the desired magnetic cross-section, is in fact a neutron that scattered through the coherent nuclear scattering mechanism but which snuck its way through. Such a low flipping ratio is at the edge of when a polarized setup can be used successfully.

For our first attempt, we used an aluminum sample cell; however, the cell met with disaster - the gallium and the aluminum alloyed easily, destroying both cell and sample. This information was present on the materials safety data sheet (MSDS), but was not read until the cell was destroyed and an explanation was required. For the second experimental setup, a quartz sample cell was used, the inner cell dimensions of which were 5cm x 3.5cm x 4mm (See Fig. 4.1).

One q-value, $q = 0.47\mathring{A}^{-1}$, was measured to good accuracy to see whether further experiments were feasible and needed. Measurements were taken for the empty cell, liquid gallium, and solid gallium for the cases where the flipper was not activated

(hereafter referred to as non-flip) and where the flipper was active (referred to as flip). Using the neutron spin-polarized beam, the non-flip signal consists of the entire coherent signal, 1/3 of the incoherent signal, and 1/3 of the (para)magnetic signal. The flip signal consists of 2/3 of the incoherent signal and 2/3 of the magnetic signal. The idea of using solid gallium as a reference was to be able to eliminate the nuclear incoherent scattering (which would be present in equal amounts in the liquid and solid phase), so that we would be able to identify the magnetic scattering, which should only be present in the liquid phase.

The results for the polarized setup were inconclusive, yet encouraging. The calculated magnetic cross-section (see Chapter 3) was expected to be twice as large as the

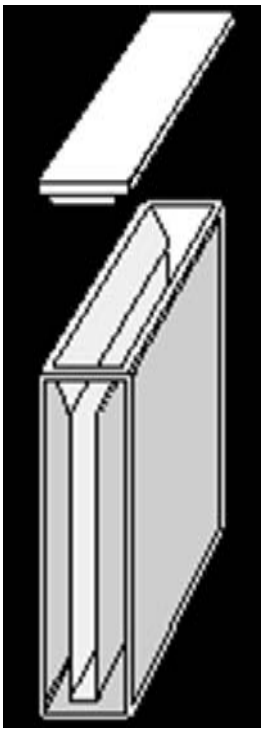

Fig. 4.1 Schematic of the first cell.

Table 4.1 The experimental values for the count rate per 400000 monitor counts for the flip and non-flip channels for samples of liquid and solid gallium contained in a quartz sample cell. The temperature of the liquid was held just above the melting point, the solid was kept just below the melting point at room temperature.

Phase	liquid	solid	difference
flip	10.959±.114	10.873± .156	$2\sigma_{mag}/3$= 0.077± .13
non-flip	11.114± .115	10.730± .155	$\sigma_{coh}^{liq}+2\sigma_{mag}/3$
difference	$\sigma_{mag}/3+ \sigma_{inc}/3- \sigma_{coh}^{liq}$	$\sigma_{inc}/3$	

incoherent cross section. The tabled results for our data are consistent with this, but also that magnetic scattering could still be absent within the margin of error. Since the scattering is dominated by the time-independent background and possibly by the elastic scattering from the sample cell, we decided to perform polarized inelastic neutron scattering experiments using a higher flipping ratio setup. We used our datum to make our case to obtain beam time at the polarized triple axis spectrometer at the Canadian Neutron Beam Center.

4.2 Polarized experiments at Chalk River

We performed polarized neutron scattering experiments using the C5 triple axis spectrometer at the Canadian Neutron Beam Center. The instrument was operated in full polarization mode, employing a Heusler monochromater and analyzer. The final energy of the scattered neutrons was fixed at 14.6 meV, and a PG-filter was used in the scattered beam to prevent higher order neutrons (with energies of $4E_f$ and $9E_f$) from reaching the detector. The flipping ratio in this setup was measured to be 1:28. The sample temperature was controlled using a Peltier cell (see Fig. 4.2), while the sample was contained in a polycrystalline quartz cell of 4 mm interior thickness, the same cell employed for the polarized experiments at MURR. Experimental runs

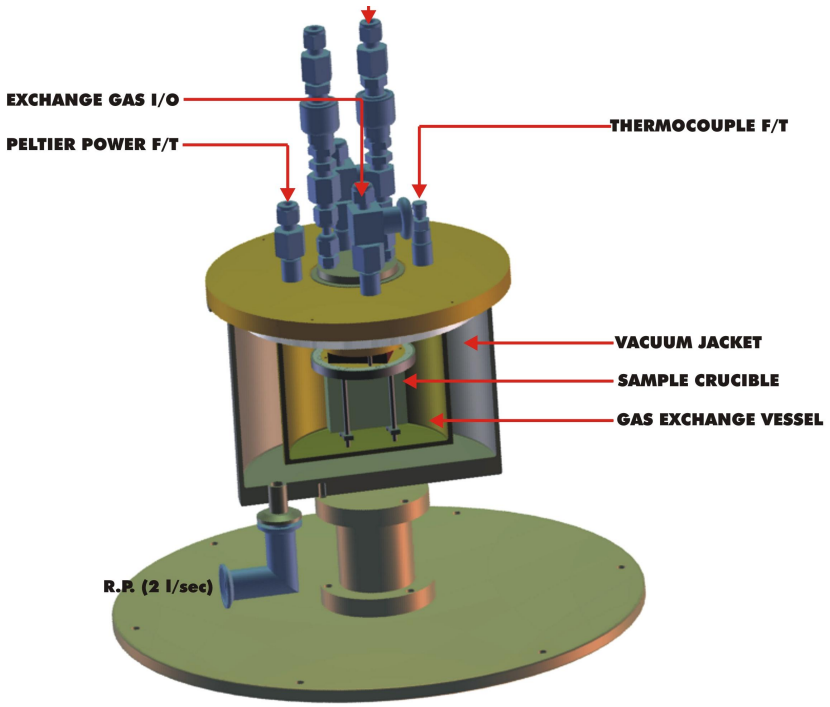

Fig. 4.2 The Peltier cell sample environment used in the Chalk River experiments, with the radiation shields cut away. The Ga sample was contained in a sample cell (marked sample crucible) made of sapphire. We employed neutron absorbing masks so that only the center of the sample cell would be illuminated by the beam. The drawing shows the face of the sample cell upon which the neutrons were incident.

were performed on solid Ga, liquid Ga, empty quartz cell, empty Peltier cell and on a vanadium reference sample.

The data analysis of a polarized experiment with such a high flipping ratio is straightforward. All coherent nuclear scattering, both from the standard hydrodynamic modes in the sample as well as from the unwanted sample cell contributions will end up in the non-flip channel (referring to neutrons that do not flip their spin polarization in the scattering process). The incoherent scattering of the sample associated with single ion motion will be divided between the non-flip channel ($\sim 1/2$) and the flip-channel

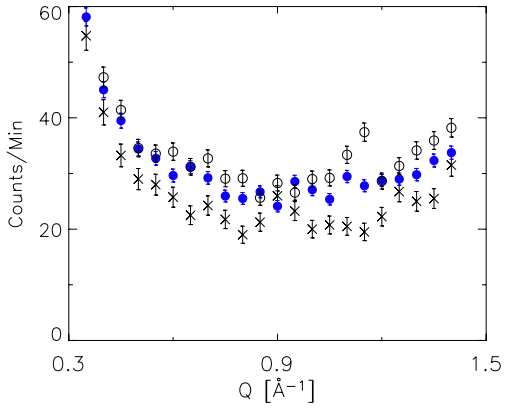

Fig. 4.3 Spin-flip signal for neutrons scattered elastically by Ga. The scattering observed in the solid state (open circles) is very similar to that of the liquid state (closed circles), while both are well separated from the scattering by the empty cell (crosses). This implies that the elastic spin-flip scattering must come from the incoherent Ga cross-section rather than from magnetic scattering (see text).

($\sim$1/2) [3]. Any paramagnetic scattering will be divided between the non-flip channel (1/3) and the flip channel (2/3). Thus, if any magnetic scattering is present, it should show up with twice the intensity in the flip channel compared to the non-flip channel.

Fig. 4.3 shows that our experimental setup was sensitive enough to observe an elastic scattering contribution above the time independent background in the neutron spin-flip channel at low momentum transfers. However, the scattered intensity of both the solid and the liquid state was at the same level. Therefore, since in the non-magnetic solid state all elastic scattering at low q must necessarily be associated with the incoherent cross-section [3], we conclude that the *elastic* scattering in the liquid involving neutron spin-flip events must also be ascribed to the incoherent Ga cross-section.

We did not observe magnetic or incoherent scattering associated with *inelastic* or

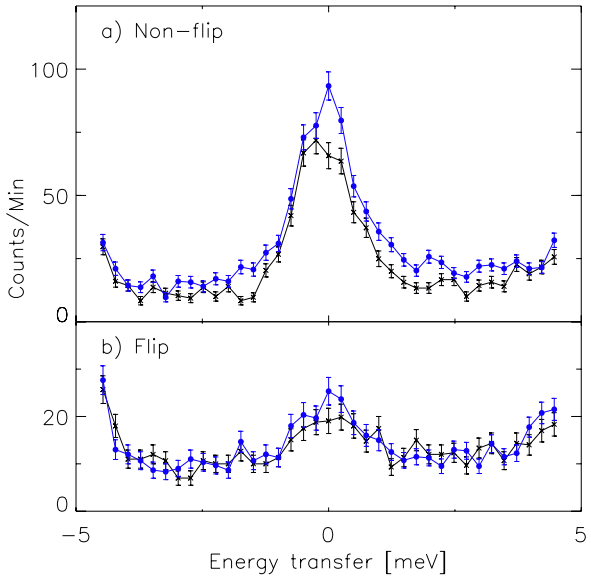

Fig. 4.4 a) The scattered neutron intensity in liquid Ga (solid circles and connecting line) at 303 K for the non-flip channel for q= 0.5Å^{-1} as a function of energy transfer E. The crosses and connecting line represent the empty cell data. b) Same as in a) but now for the spin-flip channel. Note that the spin-flip signal from the liquid does not exceed that of the empty cell for $|E| > 1$ meV, ruling out that the broad signal seen in the non-flip channel is associated with either incoherent or magnetic scattering.

quasi-elastic scattering events at $q = 0.5$ Å^{-1}, although there is a broad quasi-elastic mode in the non-flip channel associated with coherent scattering. This is emphasized in Fig. 4.4, where one can clearly observe scattering in excess of the empty cell scattering in the non-flip channel [Fig. 4.4a]. Because we do not observe the expected doubling of the signal strength in the spin-flip channel [Fig. 4.4b], the origin of this signal in this channel can neither be associated with magnetic scattering nor with incoherent scattering . In fact, the quasi-elastic scattering by the empty cell cannot even be separated from the scattering by the liquid in the spin-flip channel. Therefore, much to our chagrin, we can conclude without any further data analysis that the broad (in

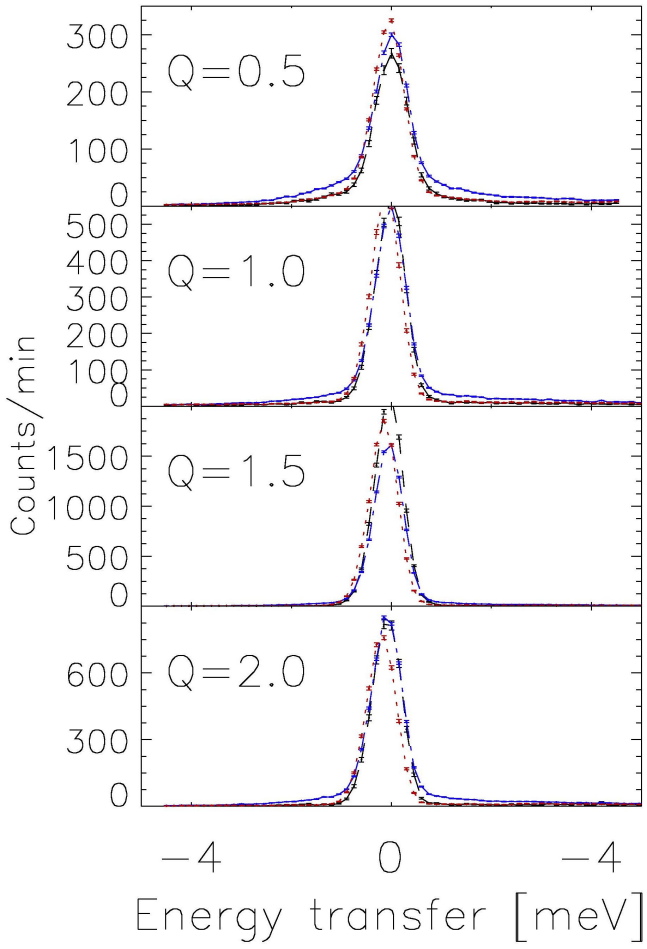

Fig. 4.5 Inelastic scans of Gallium in liquid (dotted-dashed) and solid (dotted) phases, along with the empty quartz cell cell (dashed). The data for the empty cell and for the cell containing solid gallium coincide for $|E| > 0.5$ meV, while the cell filled with liquid is seen to exceed this scattering. This is in agreement with the results of the polarized scattering experiment at C5.

energy) scattering observed in liquid Ga at low q must be coherent in origin.

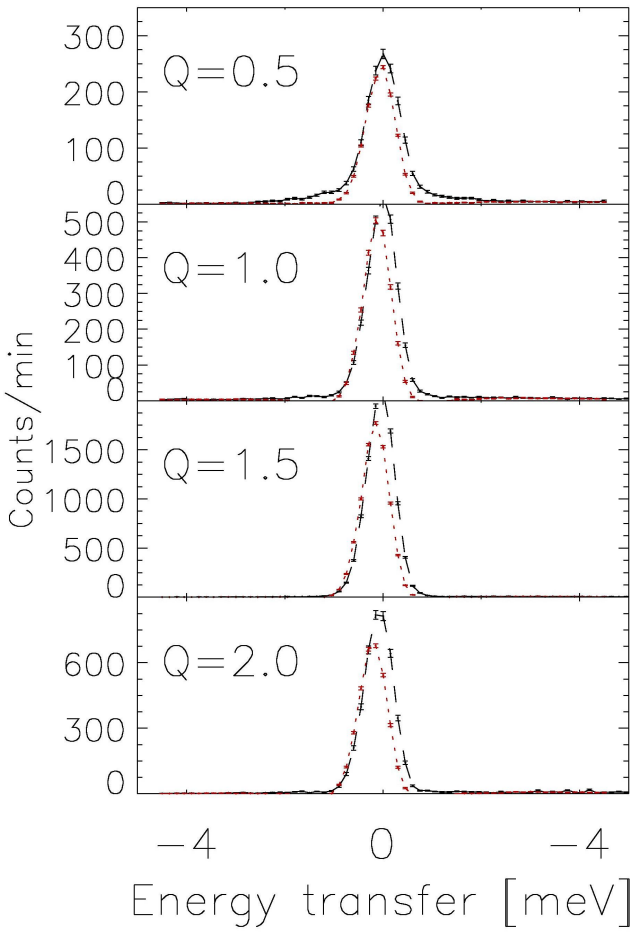

Fig. 4.6 The empty quartz cell scattering measured directly (dashed line) and the empty cell scattering measured indirectly by plotting the difference (dotted line) between the solid in the cell and the solid without the cell (the latter was achieved by solidifying the sample and then breaking the cell). The signal for the empty cell measured directly is above that of the one measured indirectly because the solid actually attenuates the scattering by the empty cell due to absorbtion within the solid. Irrespective of this, comparison between this figure and the previous figure show that the scattering by the quartz cell is too large compared to the scattering by the gallium (especially around q= 1.5 Å^{-1}) to be able to measure the line shapes with any great accuracy.

4.3 Unpolarized inelastic experiments at MURR

Next, in order to identify the origin of the broad coherent scattering at low q for which there does not exist a satisfactory explanation consistent with the $q \to 0$ limit [4,5], we performed a series of quasi-elastic, unpolarized neutron scattering experiments using the TRIAX triple-axis spectrometer at MURR. In order to ascertain whether this broad mode originates in an unknown coherent process in the liquid or whether it originates in an experimental artifact such as multiple scattering, experiments were performed using a range of spectrometer settings, employing two sample cells. All our data strongly suggests that the broad contribution to the spectra is caused by second and third order multiple scattering processes, as detailed in the following.

We first measured gallium in its solid and liquid phases using the quartz cell employed in the C5 polarized experiments. We show the results of some scans in Figs. 4.5 and 4.6. Based upon these results we concluded that the quartz cell produced too much unwanted scattering for our line shape analysis (in particular around q= 1.5 Å^{-1}), so we changed to an aluminum cell for which we collected spectra at both fixed incident and fixed final neutron energies. We used both setups as a check on the accuracy of our data correction procedure which involves corrections for multiple scattering and monitor contamination, both of which depend on the particular mode of operation of the spectrometer.

Both spectrometer operation modes yielded the same results; here we only show the data taken at fixed final neutron energy $E_f = 13.7$ meV for the sample contained in an aluminum sample holder of 3 mm interior thickness. The temperature was controlled by a ribbon heater inside an Al foil heat shield, and a PG-filter was placed in the

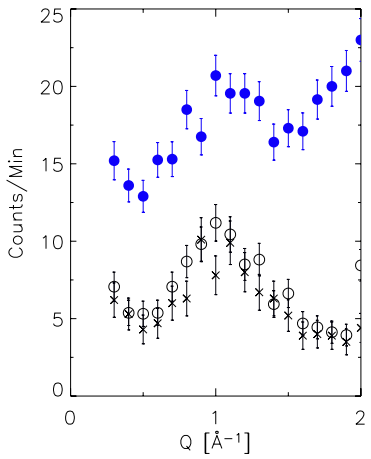

Fig. 4.7 Neutron scattering signal at constant $E = 3$ meV as a function of wave number q. The scattering by the liquid (solid circles) is well separated from that by the solid (open circles) and from the empty cell scattering (crosses). The difference between the top and bottom curves shows that there is very little q-dependence to the excess scattering up to $q = 1.3$ Å^{-1}.

scattered beam. A thin layer of plastic wrap was used to protect the Al cell walls from the corrosive effects of liquid Ga (See Fig. 4.8). The data are shown in Figs. 4.7 and 4.9. From Fig. 4.7 we conclude that the thin plastic wrap did not increase the background scattering.

We detail all the corrections we applied to the data in the following chapter, here we more or less give the results so as to keep our focus on the explanation for the broad scattering mode observed in liquid Ga. We normalized the data onto an absolute scale by using the spectrum measured at $q = 2.52$ Å^{-1}, corresponding to the main peak of the static structure factor $S(q)$. We corrected the spectrum by subtracting the empty cell data (incorporating the lack of attenuation by the absent sample), and we corrected the counting time of the incident beam monitor: while the PG-filter in the scattered beam prevents higher order neutrons from reaching the detector, these neutrons are

still counted by the monitor thereby skewing the spectral intensity to higher energy transfers. Comparing the integrated intensity over all energy transfers to the published value [36], $S(q{=}2.52) = 2.30$ yields the overall normalization factor for all spectra.

Having normalized the data, we can now calculate the contributions to the signal caused by multiple scattering events. Overall, these contributions are small, but they do make up a significant part of the scattering by the liquid at low q since the inherent single scattering contribution is relatively weak in this region. We use Sears' algorithm [46] to evaluate the multiple scattering corrections. We model the single scattering events by

$$S(q,E) = \frac{S(q)\Gamma(q)e^{E/(2k_BT)}}{\pi[E^2+\Gamma(q)^2]}, \tag{4.1}$$

where $S(q)$ is the published [36] static structure factor and $\Gamma(q)$ is the linewidth which we modeled based on x-ray data [2]. Second (and third) order multiple scattering is

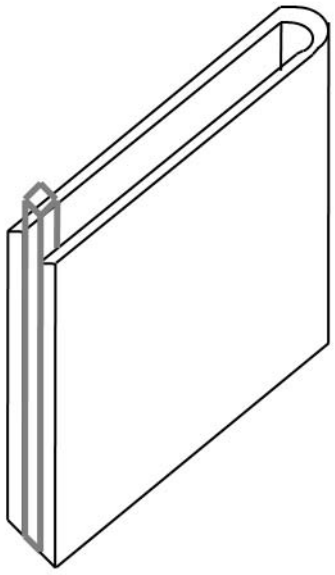

Fig. 4.8 Schematic of the second cell.

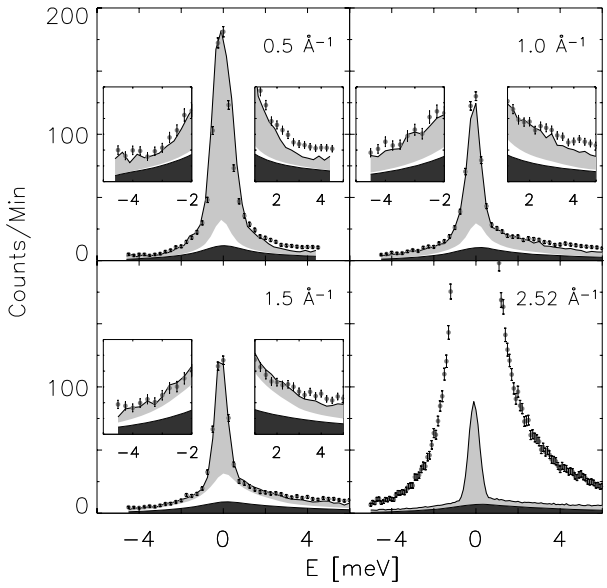

Fig. 4.9 The inelastic neutron scattering spectra of liquid Ga (solid circles) for various q-values shown in the figure. The sum (solid line) of the calculated single scattering (coherent + incoherent, unshaded), multiple scattering (dark shading) and empty cell scattering (light shading) is very close to the observed data points for all q and E, indicating that the broad mode is not associated with single order scattering, but should instead be attributed to higher order scattering. The scattering at 2.52 Å^{-1} is used for the normalization of the data.

evaluated for each (q, E)-point by numerically integrating over all possible paths within the sample volume that would see a neutron scatter twice (three times) and leave the liquid with total momentum transfer $\hbar q$ and energy transfer E. The weight of the paths in the integration is related [46] to the likelihood that a neutron would scatter and/or be absorbed along this path. This way, the calculated scattering events to any order automatically contain the sample attenuation factors, allowing for a direct comparison with experiment. The single, double and triple scattering contributions are displayed in Fig. 4.9. When we add the empty cell scattering (corrected for lack of attenuation by the sample) to our calculations, we find good agreement with the measured spectra

for most q and E values. The only discrepancy that is left is for $E > 2$ meV [see insets] which is caused by the effects of the sapphire filter [located in the neutron beam tube to reduce the fast neutron background]. These filter effects are not satisfactorily modeled by our monitor counting time correction procedure. Note that since this discrepancy is only visible for $E > 0$, it cannot be associated with any scattering events by the liquid. Therefore, based on the overall good agreement, we conclude for liquid Ga that the broad mode at low q previously associated with single scattering events [5, 37, 39] is most likely the result of second and third order multiple scattering processes. Thus, molecular dynamics simulations, neutron scattering experiments and x-ray scattering experiments are in full agreement as to the strength of the cage diffusion signal at low q.

In conclusion, we do not find any evidence in the magnetic, incoherent or coherent cross-section for a separate cage diffusion mode at low q in liquid Ga. Interestingly, this does not rule out its existence as a separate contribution in liquid Hg and Pb: the liquid Hg data which first led Badyal *et al.* [4] to propose the existence of a magnetic cross-section were analyzed in *exactly the same way* as we have analyzed our Ga data, including the same way that multiple scattering corrections were carried out. Therefore, whether short-lived magnetic moments exist in heavy metals is still an open question, as is the question of whether an additional contribution to the neutron scattering cross-section at low q exists. This question can be settled by doing polarized neutron scattering experiments, similar to the ones described here, on liquid Pb.

5

Attenuation, monitor contamination and multiple scattering corrections

In this Chapter we detail the correction that needed to be applied to triple-axis neutron scattering data in order to arrive at a data set that is given by Eq. 2.1. This relationship between the partial differential cross-section and the dynamic structure factor only holds for particles that have been scattered exactly once, and by the sample only. In practice, one has to carry out various corrections before the data represents the relationship given in Eq. 2.1. For instance, some particles that were detected at a particular scattering angle have been scattered more than once. Some particles were scattered, but were absorbed by the sample or by the container. Some particles might be scattered by the container. Perhaps not all particles that are scattered are counted by the detector. Perhaps the number of incident particles is miscounted because the incident beam might have contained particles that have wavelengths given by λ/n that might also have been selected by the monochromating device. Needless to say, the incoming beam is not perfectly monochromatic, the sample is not point sized, and the detectors have finite dimensions, all contributing to a finite experimental resolution.

5.1 Attenuation correction

Somewhat remarkably, most of these corrections do not present a problem, and all of them can be overcome with careful planning of the experiment some numerical analysis

during the analysis stages.

The instrumental resolution function, that causes a broadening of the signal in both q and E, is measured using a reference sample (mostly vanadium, that scatters incoherently) and folded into the model function when fitting the data. In general, the q-resolution is not very important in scattering experiments on liquids, and steps taken to ensure a good enough E-resolution tend to also yield an acceptable q-resolution.

Sample containers are generally chosen so as to give a minimal amount of background scattering, and empty sample container runs are a standard part of any experiment. In our case, we had to repeat our experiments since our nominally low-scattering single crystal quartz container turned out to be cheap glass and we had to settle for an aluminum container. Since our sample also absorbs some of the neutrons, we had to take into account the fact that an empty sample chamber scatters more than a filled chamber since the liquid might absorb some of the neutrons that otherwise would have yielded detectable events.

One can use a computer program to calculate the severity of this attenuation problem as a function of energy and momentum transfer, even for a sample container of irregular shape. Since our sample container is fairly regular, and since its cross section (3x4" - width x height) is much larger than the size of the neutron beam (1x2"), we can approximate our container by an infinite slab, for which we can calculate the attenuation correction exactly in the case of elastic scattering. Below we give the results for this special case in our data correction (where neutrons are scattered inelastically). We solved the relevant integrals numerically.

During our experiment, the orientation ϕ_0 (the angle between the incident neutron

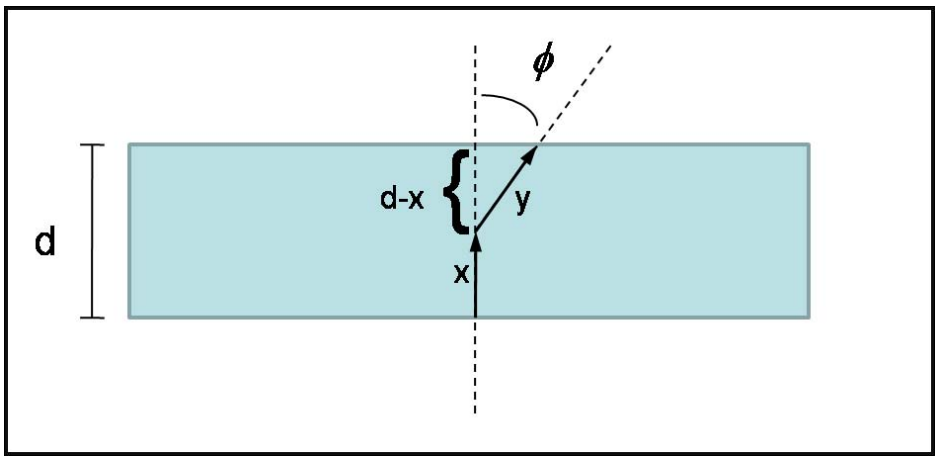

Fig. 5.1 Schematic of the single scattering in a slab of material of thickness d. The scattering angle is ϕ, the incident neutron travels a distance x in the sample before scattering. Then the neutron travels a distance y after scattering to leave the sample to get to the detector. As the integral is carried out from zero to d, the component of y in the direction of d must be used.

beam and the vector perpendicular to the surface of the sample cell) of our sample slab with respect to the incident beam changed with scattering angle ϕ in such a way that the sample is angled at half the angle of the detector arm, i.e., ϕ_0 is kept at $\phi/2$. The attenuation from a slab of material with $\phi_0 = 0^o$ (see Fig. 5.1) is given by

$$A_s(E_0, \phi) = \frac{1}{d} \int_0^d e^{-\sigma\rho(\frac{d-x}{\cos\phi})} e^{-\sigma\rho x} dx, \tag{5.1}$$

which yields

$$A_s(E_0, \phi) = (\frac{1}{d\sigma\rho(\frac{1}{\cos\phi} - 1)})(e^{-d\sigma\rho} - e^{-d\sigma\rho/\cos\phi}), \tag{5.2}$$

where d is the sample thickness, σ is $\sigma_{coh} + \sigma_{inc} + \sigma_{abs}\sqrt{25.3/13.7}$ for neutrons of fixed energy $E = 13.7$ meV, and ρ is the sample number density. With ϕ_0 included (See Fig. 5.2), the integral becomes

$$A_s(E_0, \phi) = \frac{1}{d} \int_0^d e^{-\sigma\rho(\frac{d-x}{\cos(\phi-\phi_0)})} e^{-\sigma\rho x/\cos\phi_0} dx, \tag{5.3}$$

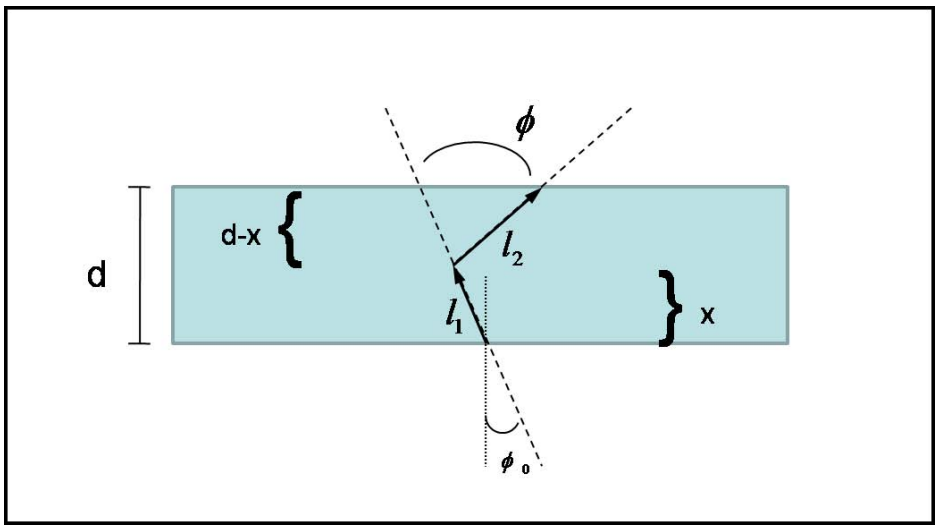

Fig. 5.2 Schematic of the single scattering in a slab of material of thickness d at an angle ϕ_0. All variables are the same as in Fig. 5.1, and ϕ_0 is the angle that the slab makes with the perpendicular to the neutron beam.

Fig. 5.3 A plot of the attenuation at a typical ϕ_0 value of 15 degrees. Note that the signal dies off at 105 degrees (90+15).

which yields

$$A_s(E_0,\phi) = \left(\frac{1}{d\sigma\rho\left(\frac{1}{\cos(\phi-\phi_0)} - \frac{1}{\cos\phi_0}\right)}\right)\left(e^{-d\sigma\rho/\cos\phi_0} - e^{-d\sigma\rho/\cos(\phi-\phi_0)}\right). \tag{5.4}$$

We applied these attenuation corrections in two ways. When we subtracted the empty sample cell from the filled sample cell, we first removed the time independent background signal (measured independently with the sample cell removed entirely) from the empty cell data. Then we multiplied the empty cell data by the attenuation correction, after which we added the time independent background signal back to the attenuated empty cell data. The resulting data set was then subtracted from the cell with sample, yielding the sample scattering.

However, this sample scattering still includes self-attenuation of the sample; more

neutrons hit the front of the sample than the back. To correct for this, the sample data (minus the modified empty cell data) were divided by the attenuation correction, yielding a sample signal that would have been measured had all parts of the sample been illuminated equally. Note that this signal still includes multiple scattering events.

5.2 Monitor contamination correction

One correction that for some reason or another is frequently overlooked is associated with the counting of the incident number of particles. This is a problem that does not occur on time-of-flight spectrometers such as those that are found at neutron spallation sources, but it is a potential problem at reactor sources and synchrotron facilities since it changes the observed line shape of $S(q, E)$.

When a single crystal is used to select one particular wavelength λ from a beam of particles of all wavelengths, particles with wavelengths λ/n are also selected. These unwanted particles will also make it to the sample and scatter. However, by using filters such as graphite in the case of neutrons, these particles can still be prevented from making it to the detector. The problem in here is that those particles will still have been detected by the incident beam monitor which is used to normalize the scattered intensity to the incident number of particles. The result is that the measured line shape as a function of energy transfer will be distorted. Note that this will only happen if the spectrometer is operated such that the incident energy of the particle is allowed to vary, while only scattered particles of a certain energy are allowed to make it to the detector. This is the standard mode of operation for most spectrometers, because by keeping the final energy fixed, one does not have to worry about the changing efficiency of the detector as a function of particle energy. In addition for neutron

scattering experiments, the monitor efficiency is inversely proportional to the incident wave number of the particle, thereby effectively taking care of the k_f/k_i term in the expression for the cross-section [Eq. 2.1]. Thus, the measured signal will be directly proportional to $S(q, E)$, rendering the experiment much easier to perform.

The severity of this monitor contamination problem depends on the incident energy and on the filters that are present in the incident beam. For instance, for a neutron with incident energy of 5 meV at a thermal reactor source, neutrons up to $\lambda/5$ present a problem. As an example, for the Si(1,1,1) reflection at the N5 beam line at the NRU reactor at Chalk River, only 20% of the monitor counts at 5 meV correspond to the desired neutrons, the remainder is all due to higher order neutrons. For higher incident energies, the problem rapidly diminishes.

There are three ways around this problem (x-rays do not suffer this problem, but polarizing an x-ray beam is more difficult than polarizing a neutron beam). First, if only $\lambda/2$ contamination would present a problem, then one can use a Si monochromator and use a reflection that does not allow second order scattering such as the Si(1,1,1) reflection frequently used in neutron scattering experiments or the Si(11,11,11) reflection that is used at the DI16 beamline at the ESRF. The second way around it only works in neutron scattering experiments. One employs a velocity selector, which is a spinning collimator that only allows neutrons of a certain range of velocities to pass through; neutrons that go too slow or too fast will be absorbed by the velocity selector. The third solution is simply to measure the contamination. This is the one we employed for our gallium experiments. By placing well characterized absorbers of varying thickness in front of the monitor, one can determine the contamination. We

detail this procedure for a neutron scattering experiment using indium absorbers.

In a neutron scattering setup for a given monochromator reflection, one measures the monitor count rate $R(\lambda_i)$ as a function of incident energy E_i, corresponding to an incident wavelength λ_i. Because of higher order neutrons also reaching the monitor, this count rate $R(\lambda_i)$ is given by

$$R(\lambda_i) = \sum_{j=1}^{N} \phi(\lambda_i/j)(1 - e^{-C\lambda_i/j}) = C \sum_{j=1}^{N} \phi(\lambda_i/j)(\lambda_i/j). \tag{5.5}$$

Here, C is a measure of the efficiency of the monitor, which is a small number by design. $\phi(\lambda)$ is the neutron flux for neutrons of wavelength λ that will make it to the monitor. The constant C will be eliminated since only the ratio $\phi(\lambda_i)/\sum_{j=1}^{N} \phi(\lambda_i/j)$ is needed to perform the monitor correction. Next one places a thin piece of neutron absorbing material before the monitor, such as a tin foil of known thickness, and one repeats the measurement of the monitor count rate. Subsequently, one doubles the thickness of the foil, and so on, until one has as many foil measurements (m) as there are higher orders of contamination present in the incident beam ($m = N$). For m layers of foil of thickness d, the monitor count rate is given by

$$R(\lambda_i, m) = C \sum_{j=1}^{N} \phi(\lambda_i/j)(\lambda_i/j)e^{-mb/j} \tag{5.6}$$

with the foil parameter b is given by the number density of the foil n_f, the absorbtion cross-section of an atom in the foil σ_{abs} at neutron energy E_i, and its thickness $b = dn_f\sigma_{abs}(E_i)$. All measurements can be written in matrix form as $M\phi(\lambda_i/j) = R(\lambda_i, m)/C$, with the matrix elements given by

$$M_{j,m} = (\lambda_i/j)e^{-mb/j}. \tag{5.7}$$

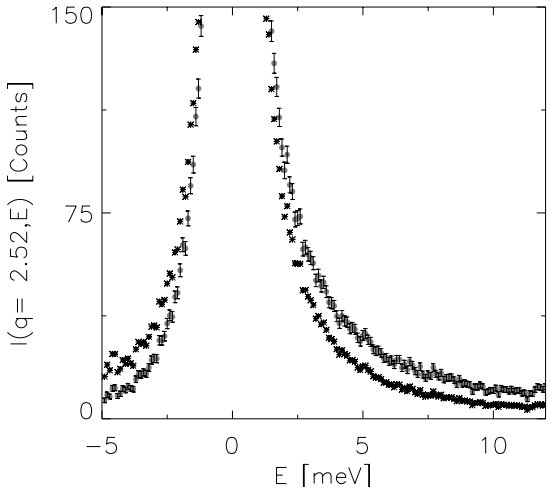

Fig. 5.4 The scattered intensity (solid circles) for liquid Ga at 293 K for q= 2.52 Å^{-1} as measured at a thermal source triple-axis spectrometer. This particular q-value corresponds to the peak in the static structure factor. Applying the measured monitor correction leads to a substantial change in line shape (stars), illustrating the need to account for this correction before modeling the line shapes.

Next one finds the desired ratios for each λ_i by applying the least squares formalism:

$$\phi(\lambda_i/j)/\phi(\lambda_i) = (M^T \cdot M)^{-1} M^T [R(\lambda_i, m)/R(\lambda_i, 0)]. \tag{5.8}$$

We illustrate the importance of the monitor correction in Fig. 5.4 for our data on liquid Ga taken on TRIAX when operated at fixed final energy of 13.7 meV, and the incident neutron energies were selected using the PG(0,0,2) reflection. As can be seen in this figure, even with sapphire and PG/Si filters in the incident beam, the line shape distortion due to monitor contamination is rather substantial. Once the monitor correction has been characterized for one particular setup that depends on the collimators that are in place during an experiment, one can then deduce the characteristics of the various filters. With this information, one can then calculate the monitor correction for other spectrometer setups and make reasonable guesses of the

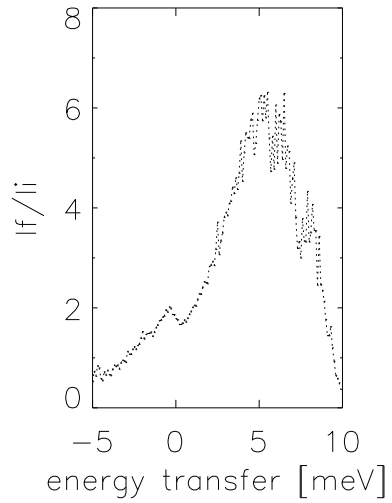

Fig. 5.5 The monitor correction ratio with respect to energy transfer obtained by direct division of the scattered intensity measured for liquid Ga at q= 2.52Å^{-1} for fixed final energy of the scattered neutron (If) and fixed initial energy of the neutron (Ii).

severity of the correction when using different monochromators.

Finally, another way of getting a quick check on whether the monitor contamination procedure is needed or not is by comparing data taken at fixed initial neutron energy to data taken at fixed final neutron energy. We show the result for this in Fig. 5.5 where we directly compare data for gallium. These data were not corrected for anything and hence they will likely only be reliable for $|E|$ <5; nonetheless, this clearly illustrates the severity of the monitor correction problem.

5.3 Multiple scattering correction

The direct correspondence between the partial differential cross-section and the dynamic structure factor as given in Eq. 2.1 is only valid for particles that have been scattered once. In an actual scattering experiment, this single scattering condition can never be met. For instance, if a sample scatters 10% of the incident particles, then

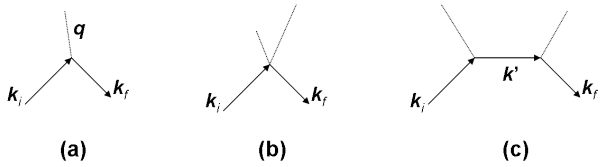

Fig. 5.6 When a particle with incident wave vector $\mathbf{k}_i$ (arrow) gets scattered by a sample it can excite a density disturbance of momentum $\mathbf{q}$ (dotted line, part a), or it can excite multiple disturbances (part b). The latter is referred to as the multi-phonon component. A particle can also undergo multiple scattering events before exiting the sample (part c), a process referred to as multiple scattering.

roughly 10 % of the scattered particles will be scattered once more. If instead one opts for an experimental setup where only 1 % of the particles are scattered, then the multiple scattering problem will be of far lesser importance; however, one has to measure for 10 times longer, and the single scattering signal might even disappear in the background noise. Whatever the setup, multiple scattering will present the largest headache at the low momentum transfers since the cross-section for single scattering is quite small here. Hence, at small momentum transfers, multiple scattering might constitute most of the detected signal, and one has to correct the data in order to re-establish the connection between the cross-section and the dynamic structure factor.

Multiple scattering events should not be confused with multi-phonon scattering. We clarify the difference in Fig. 5.6. In a multi-phonon process, two excitations are created simultaneously in the scattering event. The multi-phonon contribution might be an unwanted contribution since it could interfere with determining the density of states in a solid or with determining the weight of the single-phonon scattering. Nonetheless, it is a part of the dynamic structure factor, unlike multiple scattering events. In liquids, only ^{4}He has been shown to exhibit multi-phonon scattering.

In order to correct for multiple scattering effects, one needs to know both the geometry of the sample, as well as the dynamic structure factor $S(q, E)$. Provided the sample does not scatter more than $\sim$ 10-20% of the incoming particles, one can calculate the multiple scattering correction in a straightforward manner. For instance, as a first step one can model $S(q, E)$ by $S(q, E) = S(q)\Gamma_q/\pi(\Gamma_q^2 + E^2)$. Here the linewidth Γ_q is given by the coefficient of self-diffusion D_s as $\Gamma_q = D_s q^2$. The reason why this initial guess for $S(q, E)$ works remarkably well is because most of the multiple scattering events come from scattering processes corresponding to large values of $S(q)$ where the decay time of the excitations is dominated by the properties of individual atoms. In general, the multiple scattering signal shows very little dependence on scattering angle. Once the multiple scattering correction has been determined using this initial, somewhat crude model, a new iteration can be performed where one can use the actual data minus multiple scattering correction as a better estimate for $S(q, E)$.

The multiple scattering correction, given an initial estimate of $S(q, E)$, is calculated using a computer. On the one hand, one can use a Monte Carlo routine to generate random scattering events for a particle that enters the sample from one side with a certain initial energy and leaves the sample in a fixed direction with a given change in energy. The weight of the scattering events is determined by $S(q, E)$. On the other hand, one can follow the procedure developed by Sears (Sears 1975) and use the computer to integrate over all multiple scattering possibilities. We describe the latter procedure in some detail since it is very easy to carry out on liquids, yielding corrections to data that not only include corrections for when a particle scatters twice, but also for when it scatters more than two times; it also includes corrections for the attenuation

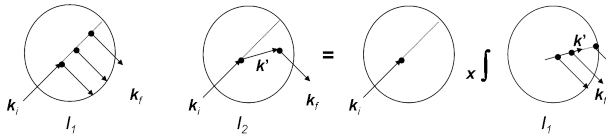

Fig. 5.7 Some of the potential paths that a particle can take when it is scattered multiple times by the sample. At every scattering event we have conservation of momentum and energy.

by the sample as a function of scattering angle and energy transfer. The procedure is the same for both neutron and x-ray scattering experiments.

To calculate the relative strength of the multiple scattering correction for a particle with incident energy E_i and wave vector $\mathbf{k}_i$ exiting the sample with final energy E_f and wave vector $\mathbf{k}_f$ (see Fig. 5.7) the procedure is as follows. First one comes up with a reasonable model for the dynamic structure factor $S(q, E)$ as described in the preceding paragraphs. Next, one first calculates the strength of the single scattering contribution as shown in Fig. 5.7. In this figure, the length of the path that the particle would take if it were not scattered at all is designated L_0. The particle is then forced to scatter somewhere along this path, at point x, transferring a fixed amount of energy $E = E_i - E_f$ and momentum $\hbar q = |\hbar\mathbf{k}_i - \hbar\mathbf{k}_f|$. The length of the path that the scattered particle has to cover before exiting the sample is calculated and designated $L_f(x)$. The weight $W(x)$ of this particular scattering event is

$$W(x) = e^{-x\Sigma(E_i)} S(q = |\mathbf{k}_i - \mathbf{k}_f|, E) e^{-L_f(x)\Sigma(E_f)}, \tag{5.9}$$

with $\Sigma(E)$ given by $\Sigma(E) = n(\sigma_{abs}(E) + \sigma_{coh} + \sigma_{inc})$. The scattered intensity I_1 corresponding to all possible paths for single scattering in a liquid of number density n is then given by

$$I_1(\mathbf{k}_i, \mathbf{k}_f, E_i, E_f) = n\sigma \int_{x=0}^{x=L_0} dx W(x). \tag{5.10}$$

Note that by replacing $S(q, E)$ by 1 in Eq. 5.9, one would get the formalism for calculating the attenuation correction. Second order multiple scattering is calculated in an analogous manner. The initial path L_0 is subdivided as before, but now the particle is allowed to scatter in any direction and emerge with an intermediate energy E' and wave vector $\mathbf{k}$' (see Fig. 5.7). After the first scattering event the same procedure is followed (as in single scattering) by calculating the length of the path L' between the point of scattering and the exit point and forcing the particle to scatter once more along this path to end up with a final energy of E_f and wave vector $\mathbf{k}_f$. One then integrates over all intermediate scattering states to get the scattered intensity I_2 corresponding to particles that have been scattered exactly twice:

$$I_2(\mathbf{k}_i, \mathbf{k}_f, E_i, E_f) = n\sigma \int \frac{d\hat{\mathbf{k}}'}{4\pi} dE' dx S(|\mathbf{k}_i - \mathbf{k}'|, E_i - E') e^{-x\Sigma(E_i)} I_1(\mathbf{k}', \mathbf{k}_f, E', E_f). \tag{5.11}$$

In this equation, I_1 is calculated with the starting point of the particle's trajectory inside the sample, as shown in Fig. 5.7. Comparing I_1 to I_2 yields the ratio of double scattering to single scattering for a particular momentum and energy transfer. Thus, one can carry out a multiple scattering correction even when the data have not been absolutely normalized. The above procedure is easy to implement on a computer, and calculation of I_3 can be done in a similar recursive way where I_3 is expressed as an integral over I_2. Modern computers have enough power to calculate second order multiple scattering in a minute, and up to third order multiple scattering corrections in a couple of hours. Hence, there is no longer a need to use approximate methods. Calculations up to third order are sometimes necessary when trying to obtain information on the single scattering cross-section at low momentum transfers since single scattering

can be so weak that it is comparable in strength to the third order multiple scattering contribution. This turned out the be the case for our gallium data at low momentum transfer.

5.3.1 Single and multiple scattering model for liquid gallium

We employ the method outlined in the preceding to liquid gallium. We used a simple Lorentzian scattering function as our model for $S(q, E)$. The area of the Lorentzian is given by published data of the static structure factor of liquid Ga, and the linewidth Γ of the Lorentzian was taken to be given by the coefficient of self-diffusion $D_s$for large momentum transfers ($\Gamma = D_s q^2$) and by the measured width (from x-ray scattering experiments) for smaller momentum transfers. The advantage of using a single Lorentzian line to describe the scattering is that the energy convolution in Eq. 5.11 can be calculated analytically, cutting down on the computational overhead.

We show the results for the calculated first, second, and third order scattering by liquid gallium in Figs. 5.8, 5.9, 5.10. Note the dip in scattered intensity for scattering angles close to 90^o as a result of having performed the multiple scattering correction for ϕ_0=0. When we calculate the multiple scattering contribution for different ϕ_0, we simply divide the data shown in these figures by the appropriate attenuation correction for ϕ_0=0, after which we multiply the data sets by the attenuation correction for $\phi_0 \neq$0.

In order to compare these calculations to the measured spectra we need to convert the constant scattering angle of these calculations to the constant momentum transfer that was employed in the experiments. We do this using $q^2 = k_i^2 + k_f^2 - 2k_i k_f \cos\phi$ and $E = (\hbar/2m)(k_i^2 - k_f^2)$. Thus, the particular ϕ-values corresponding to a q-value is

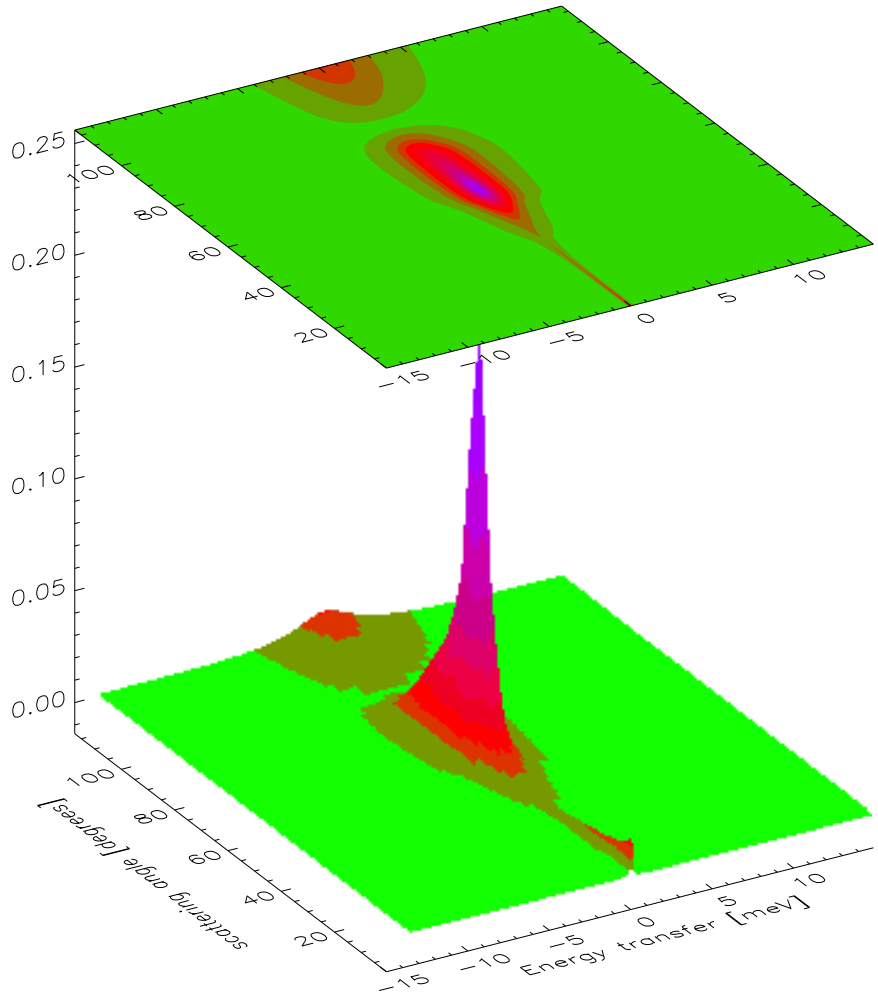

Fig. 5.8 The calculated first order scattering based on a Lorentzian model for single scattering. The 3-D plot is energy transfer vs. scattering angle vs. intensity. The top plot is a contour plot of the bottom.

given by

$$\phi = \cos^{-1}[\frac{(\frac{E_i}{2.0718}) + 2k_f^2 - q^2}{2k_f\sqrt{(\frac{E_i}{2.0718}) + k_f^2}}], \tag{5.12}$$

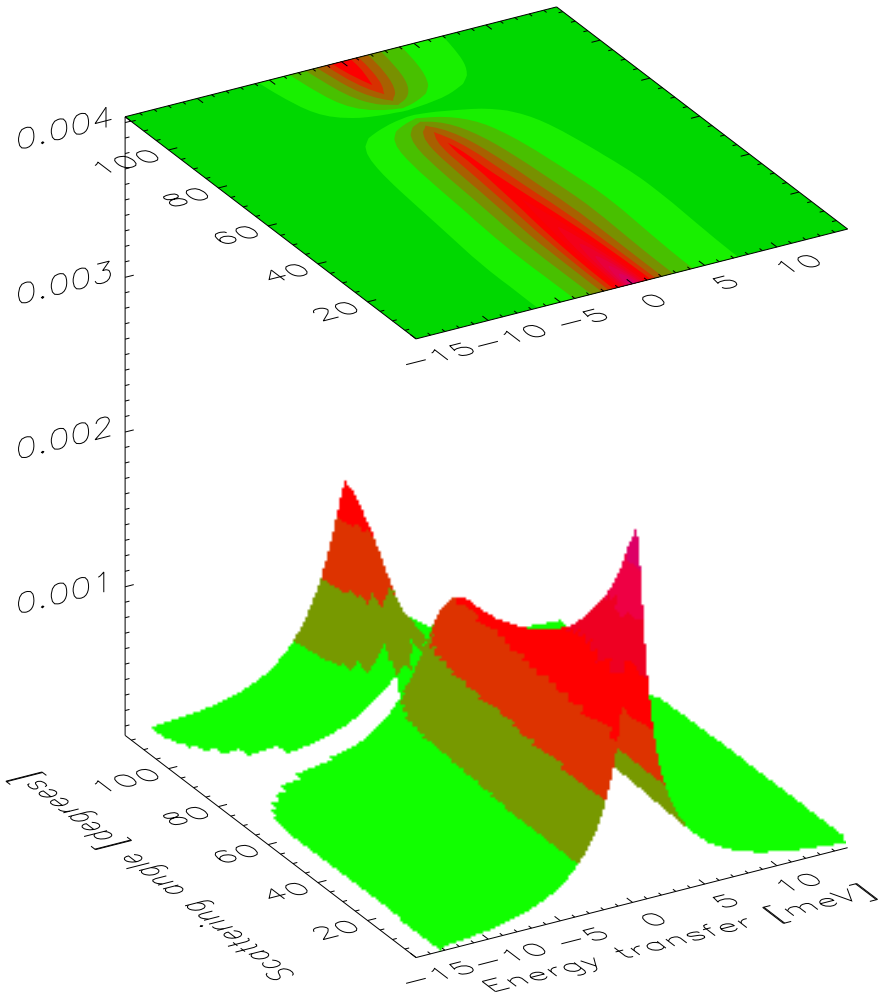

Fig. 5.9 The second order scattering calculated based on a Lorentzian model for single scattering.

where $k_f = \sqrt{E_i/2.0718}$ with $E_i = 13.7$. This convention was chosen because the final energy was fixed in the experiment shown in Chapter 4.

The next step needed is the absolute normalization of the data, which can be achieved by comparison to the literature data for the static structure factor. In our

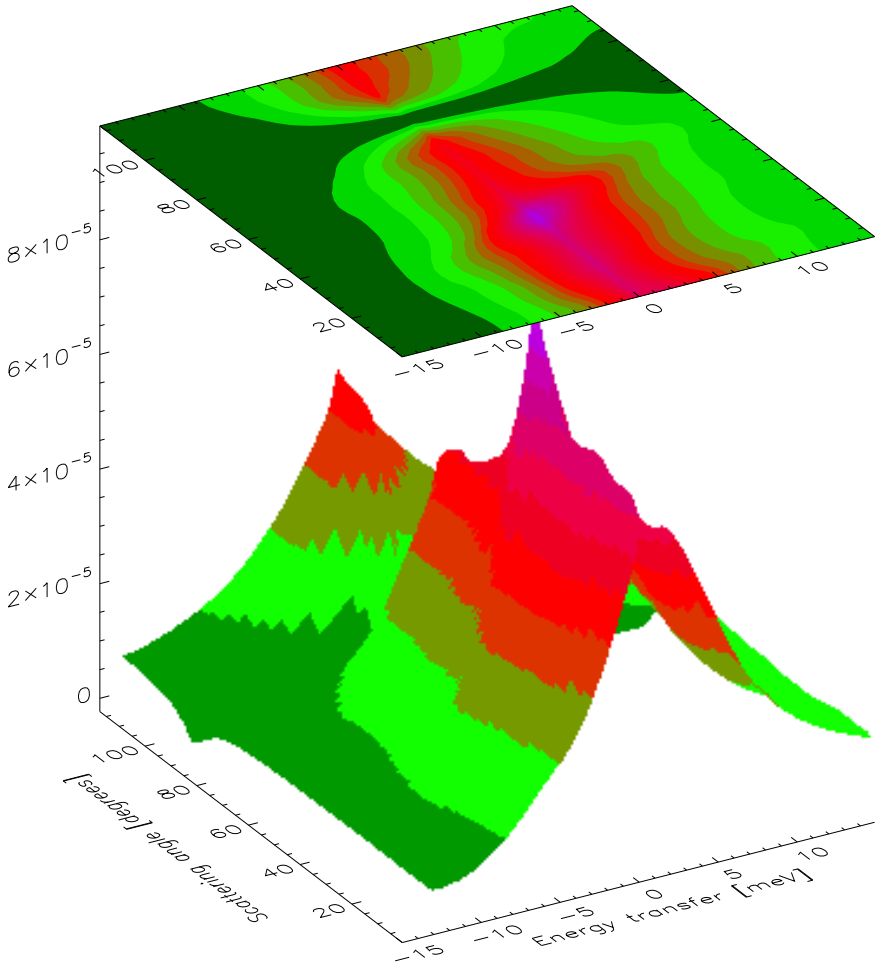

Fig. 5.10 The third order scattering calculated based on a Lorentzian model for single scattering.

case we used the inelastic data for a q-value corresponding to the peak (q=2.52 $\mathrm{\AA}^{-1}$) of the static structure. The integrated inelastic data

$$\int I(q = 2.52\mathring{A}^{-1}, E)dE \tag{5.13}$$

is divided by the peak height of 2.3 obtained from the literature [36], yielding the

overall normalization factor. Because we were not able to measure the full energy transfer spectrum at q=2.52 Å^{-1}, a Lorentzian fit of the data was performed to get the large (positive and negative) energy transfers, and then the integral was performed on the fit. This resulted in a normalization factor between spectrometer counts per monitor and absolute units of $N = 1583.315/2.300$.

Lastly, we folded detailed balance into the model. The probability of initially having the scattering system in a higher energy state is less than the system being in a lower energy state. The relation is given by:

$$S(q, -\omega) = e^{-\hbar\omega\beta} S(q, \omega), \tag{5.14}$$

where $\beta = \frac{1}{k_b T}$. However, this relationship was not put in the model for $S(q, E)$ since this would prevent the analytic convolution of two Lorentzian line shapes. Instead, we multiplied the model after the fact by the detailed balance function $e^{-E*(11.58/2/300)}$.

Next, we convoluted the model (single plus double plus triple scattering) at a given q-value with the measured energy resolution function, $\sqrt{\frac{4\ln 2}{\pi \times 0.7^2}} e^{-E^2 \frac{4\ln 2}{0.7^2}}$. Then, the empty cell signal (times the monitor correction) is added to the signal calculated signal. These are the comparisons that were shown in Fig. 4.9.

5.3.2 Fixed E_i samples

For experiments performed in the fixed initial energy setup, the corrections are different from the fixed final energy setup. First, the model should be multiplied by $\frac{k'}{k}$ which is $\sqrt{\frac{E_i - energy}{E_i}}$. The detector efficiency changes when the initial energy is fixed, and the final energy varies because the detector is moving. The faster moving neutrons will not be absorbed by the helium in the detector as readily as the slower moving neutrons.

The absorption of a neutron in a cylindrical detector is given by:

$$\begin{aligned} P_{detection} &= x \sum_{m=0}^{\infty} [\frac{x^{2m} \cdot \pi/4}{(m+1)!m!2^{2m}} - \frac{x^{2m+1}2^{2m+1}m!(m+1)!}{(2m+1)!(2m+3)!}] \\ &= x \cdot \frac{\pi}{4} - x^2\frac{1}{3} + x^3\frac{\pi}{32} - x^4\frac{1}{45} + ... \end{aligned} \tag{5.15}$$

where $x = \sigma_{abs}(E)\rho d$, and $\sigma_{abs}(E) = \sigma_{abs}\sqrt{\frac{25.3meV}{E_f}}$. The model is divided by this correction. We find similar results when applying this model to the data at fixed E_f. See Fig. 5.11 for results for the quartz cell at fixed E_i with the aforementioned corrections applied. The addition of the empty cell signal to the single and multiple scattering equals the measured signal.

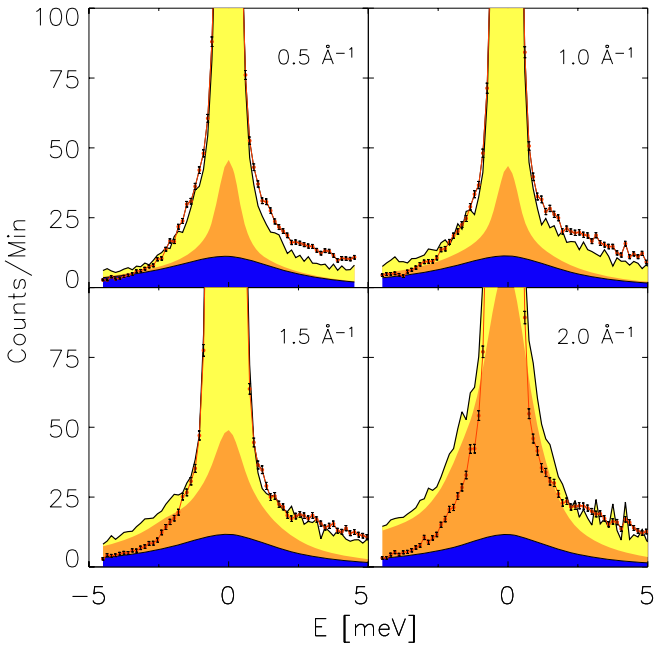

Fig. 5.11 The inelastic neutron scattering spectra of liquid Ga (solid circles) for various q-values shown in the figure. The sum (solid line) of the calculated single scattering (coherent + incoherent, orange), multiple scattering (blue) and empty cell scattering (yellow) is very close to the observed data points for all q and E, indicating that the broad mode is not associated with single order scattering, but should instead be attributed to higher order scattering. The scattering at 2.52 Å^{-1} is used for the normalization of the data (See Fig. 4.9).

6
Partial Wave Method

This and the following chapter deal with the investigation of potential quantum effects in classical liquids. In the preceding chapters, we have been investigating the processes related to cage-diffusion. The one most important parameter in cage diffusion is how easy it is for an atom to escape the cage formed by its neighbors. Classically, this involves the collision between two particles, and this is what one calculates in molecular dynamics computer simulations. Quantum mechanically, the process is more complicated since the colliding atoms will have (remnant) wave characteristics that could give rise to interference effects, ultimately leading to a velocity dependent probability that a particle can escape its cage. In this and the next chapter, we investigate if and when one should include quantum interference effects when studying the collision between two atoms in a liquid. We find that quantum interference effects likely play a much more prominent role, as evidenced by glory scattering (to be discussed), than one would expect *a priori* based upon the temperature of the liquid and the mass of the atoms.

6.1 Introduction

Classically, the collision between two atoms (See Fig. 6.1) is a straight-forward problem to solve, provided the interaction potential $V(r)$ is known. For a central force-field, the probability that an incoming particle is deflected over an angle θ can be calculated.

If the potential is conservative, the collision can be treated as an elastic collision in the center of mass system: the incoming particle has a reduced mass μ, and the only relevant velocity is the relative velocity v. In the following, we will assume that the potential is spherically symmetric and conservative.

It is well known that helium atoms exhibit quantum interference effects, and that these effects show up in neutron scattering experiments. In Figs. 6.2 and 6.3 we show the half width and peak position of response function of liquid helium at high momentum transfers (high compared to the first peak in the static structure factor). The linewidth is a measure of how easy it is for one helium atom to slide by another, the mechanism one encounters in the cage-diffusion process. At these large momentum transfers, the linewidth is largely determined by the motion of a single particle, allowing us to link the linewidth directly to the ease of cage-diffusion. A large linewidth corresponds to a short residence time, and hence it implies a large cross-section for one helium atom being deflected over a small angle when colliding with another atom. After all, a small deflection angle implies that the colliding helium atom has made it

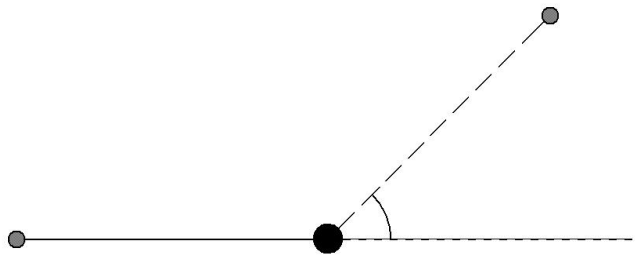

Fig. 6.1 Schematic representation of two particles scattering: the incoming particle collides with the scatterer (which is considered here as fixed in place). The incoming particle is then deflected over an angle θ compared to its previous direction.

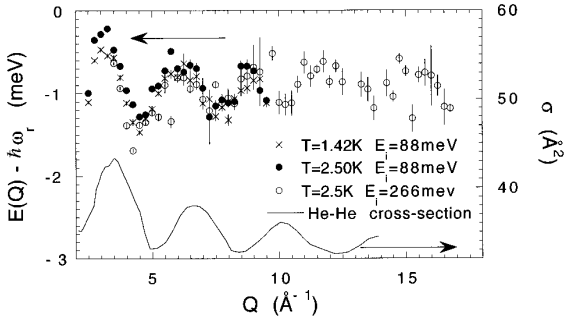

Fig. 6.2 Figure reproduced from From Andersen *et al.* [59]. Shown are the oscillations in the linewidth of neutron scattering spectra (points) together with the calculated velocity dependent cross-section for ^{4}He-^{4}He scattering. The agreement between the phase of the calculated oscillations and the observed changes in linewidth show that in order to fully understand cage diffusion one has to take quantum effects into account. In order to relate the relative velocity to momentum transfer, the authors used $mv = \hbar Q$.

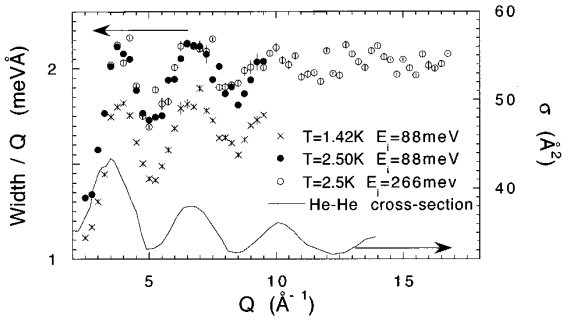

Fig. 6.3 Figure reproduced from From Andersen *et al.* [59]. Shown are the oscillations in the peak position of neutron scattering spectra (points) together with the calculated velocity dependent cross-section for ^{4}He-^{4}He scattering. Note that the peak position and the calculated cross-section are out of phase with each other.

past the obstructing atom (see Fig. 6.4).

Clearly, for light particles like helium that approach each other with low relative velocity, classical physics is no longer sufficient to describe the collision. As is demonstrated in the figure, it is necessary to use quantum mechanics to solve the problem. What is less clear, however, is whether one would also have to take quantum effects

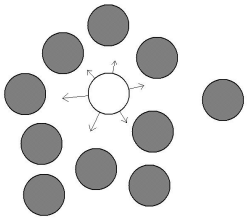

Fig. 6.4 An atom can make it out of its cage if it undergoes a collision with its neighbor resulting in a small deflection angle. A large deflection angle would essentially make it bounce back into the cage.

into account for heavier atoms like sodium and gallium. In these chapters, we answer this question, but a good indication that quantum interference effects might well play a role comes from x-ray scattering experiments on liquid gallium by Scopigno *et al.* [2]. Scopigno observed oscillations in the linewidth of the gallium response function at high momentum transfers. Scopigno found that these oscillations could be described by using an analytical approximation for the dynamics of hard-spheres (a classical system). This is shown in Fig. 6.5.

While the agreement between experiment and hard-sphere approximation is extremely good, it is also unphysical. In order to get the good agreement, Scopigno had to use a hard-sphere diameter that is unphysical: the hard-sphere diameter used was so large that it would correspond to a liquid in which the volume occupied by the hard-sphere atoms would exceed the available volume. However, these oscillations are reminiscent of what was observed in liquid helium (see Fig. 6.2). Therefore it is possible that what is being observed in experiment is distorted somewhat by quantum interference effects. For instance, in liquid gallium it could well be that there are some small remnant interference effects that might affect the oscillations to such an extent that

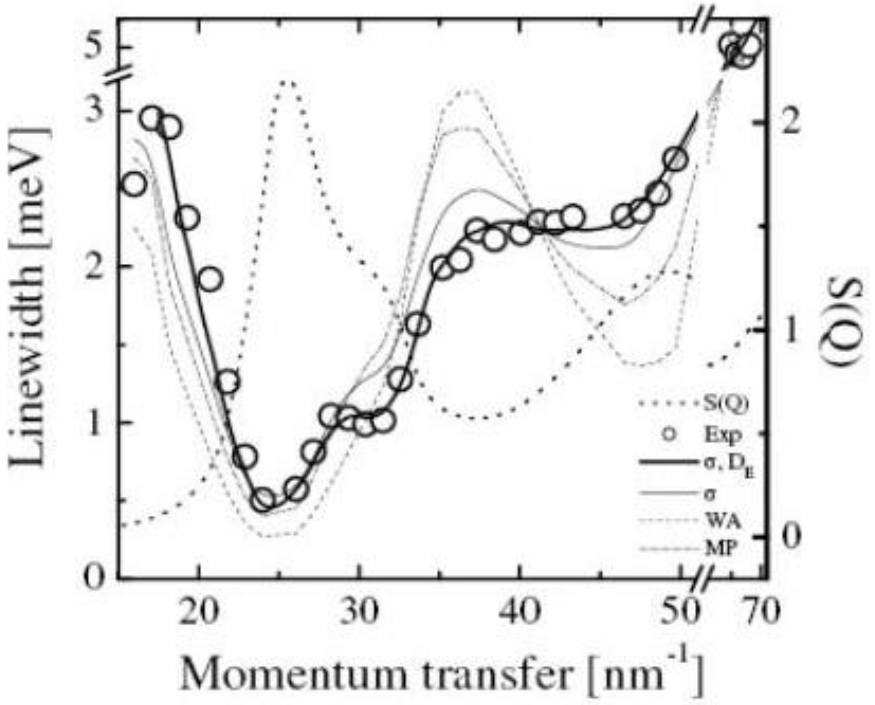

Fig. 6.5 This figure has been reproduced from Scopigno *et al.* [2]. One can clearly observe oscillations in the half width of the response function of gallium, up to momentum transfers well beyond where oscillations in the static structure factor are still observable. The solid line through the points are the results of a hard-sphere approximation using an unrealistic hard-sphere diameter.

they can only be described by a classical model that is unphysical. If such interference effects are present in gallium, we expect them to be small since the mass of gallium greatly exceeds that of helium. In the next chapter, liquid gallium is investigated to decide whether part of these oscillations do indeed reflect quantum mechanical interference effects, akin to what has been observed in liquid helium. Given the much larger mass of gallium it is by no means clear whether quantum mechanics play a role or not. One thing to note is that the temperature of the liquid plays no role. In the colli-

sion process relevant to cage diffusion only the relative velocity is important, not the overall thermal velocity. Another indication that a quantum mechanical description is required for liquid gallium is that similar measurements of liquid mercury [2] did not require unphysically large hard-sphere diameters. Since Hg atoms are much heavier, quantum mechanical effects are expected to be much smaller compared to Ga atoms.

In order to solve the two atom collision problem quantum mechanically, the radial Schrödinger equation,

$$\frac{d^2G_l(r)}{dr^2} + (k^2 - U(r) - \frac{l(l+1)}{r})G_l(r) = 0, \tag{6.1}$$

needs to be solved for the wavefunction $\Psi(\mathbf{r}) = G_l(r)/r$, which is the sum of the incoming and scattered wave:

$$\Psi(\mathbf{r}) \sim e^{i\mathbf{q}\cdot\mathbf{r}} + f(\theta)\frac{e^{iqr}}{r} \tag{6.2}$$

where $f(\theta)$, the scattering length, only depends on one angle because of assumed cylindrical symmetry. Here, $k = \sqrt{2\mu E_i/\hbar^2}$ and $U(r) = (2\mu/\hbar)V(r)$, where μ is the relativistic mass, E_i is the initial energy, and V(r) is the spherical potential.

The scattered wave is spherically symmetric, but the probability that it can be detected depends on the scattering angle: $P \sim |f(\theta)|^2$. The scattering length depends on the range of the potential (in other words, on the size of the particles) and on the relative velocity v. The aim is to calculate $f(\theta)$ by solving the Schrödinger equation. For realistic potentials this can only be done numerically.

The average time an atom stays trapped in the cage formed by its neighbors (See Fig. 6.4) depends on the difference between forward and backward scattering amplitudes $|f(0\,\mathrm{deg})|^2 - |f(180\,\mathrm{deg})|^2$. Since $f(\theta)$ depends on the relative velocities of the

two atoms, the oscillations as a function of momentum, such as observed in liquid helium and potentially liquid gallium, could well be influenced by these interference effects.

Next, the quantum mechanical collision problem as well as the partial waves method, employed to solve said problem, are described. For a spherically symmetric potential, a separation of angular and radial variables simplifies the problem. The solution of the Schrödinger equation can then be written in terms of a series expansion in angular momentum quantum numbers l, with a differential wave equation for the radial wavefunction $\Psi_l(r)$ that needs to be solved for each value of l. The azimuthal quantum number m is not featured in the solution since the scattering problem has a cylindrical symmetry.

The solution to the collision problem is standard [55]; however, since the calculation is on the borderline between the classical and quantum regimes, the solution will require an expansion up to very large values of l. First, the incoming plane wave is expanded in terms of spherical waves (See Appendix E.1 for more details):

$$e^{i\mathbf{q}.\mathbf{r}} = \sum_{l=0}^{\infty}(2l+1)(i)^l j_l(qr)P_l(\cos\theta) \tag{6.3}$$

where j_l is the spherical Bessel function of order l, and P_l are the Legendre polynomials. The terms in this expansion for which $j_l(q,R)$ is significantly different from zero are kept, with R the range of the interatomic potential. For each l (partial wave), the corresponding radial wave equation is solved in the presence of potential $V(r)$. The solution is sketched in Fig 6.6. For large r, the effect of the potential is to introduce a phase shift η_l (that depends on the relative velocities of the atoms), and the solution

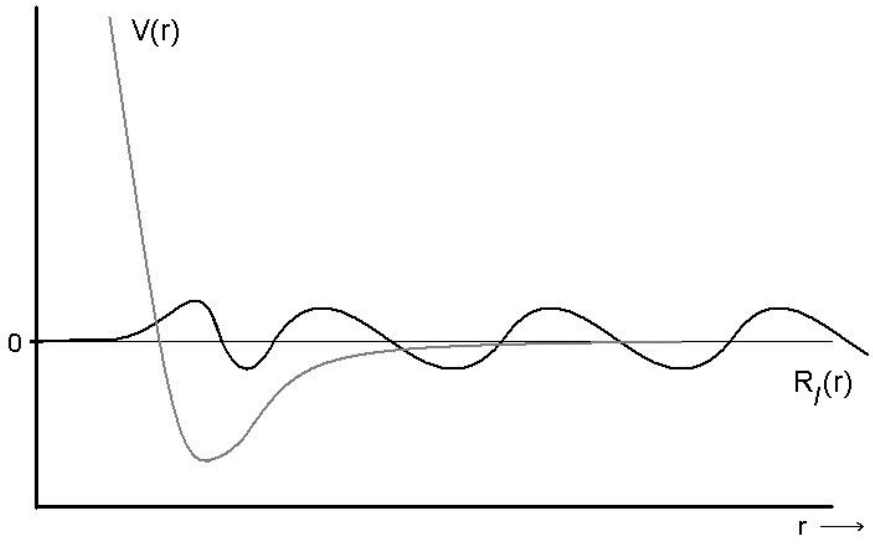

Fig. 6.6 Schematic of potential $V(r)$ (dashed line) and the radial wave function (solid line), $R_l(r)$, solved for $V(r)$. For large r (where the potential is small), the only change to the radial wave function is a phase shift.

to the collision problem can be written [55] as (See Appendix E.2):

$$f(\theta) = \frac{1}{2q}\sum_{l=0}^{\infty}(2l+1)e^{i\eta_l}\sin\eta_l P_l(\cos\theta). \tag{6.4}$$

From this, the differential cross-section $\frac{d\sigma}{d\Omega} = |f(\theta)|^2$ is calculated, as well as the total velocity-dependent cross-section,

$$\sigma = \int d\Omega |f(\theta)|^2 = \frac{1}{4q^2}\sum_{l=0}^{\infty}(2l+1)\sin^2\eta_l. \tag{6.5}$$

Thus, in order to determine whether quantum mechanics play a role in cage diffusion, we only need to determine the phase shifts η_l for a given potential, where the phase shift is the difference between the radial wavefunction with the potential present and absent. All this is illustrated in Fig. 6.6 where one can see that the only effect of the

scattering potential with finite range on the incoming particle is to change the phase of its wave function (compared to the non-interacting particle).

Next we take a closer look at what processes give rise to oscillations in the cross-section.

6.2 Glory scattering

Glory scattering is the phenomenon in which the cross-section for a particle being deflected over a particular angle is very large. We are particularly interested in the so-called forward glory, a process where the particle suffers a very small deflection angle during a scattering event. First, we briefly describe the terminology and the main scattering characteristics using classical scattering theory. For this, we follow the description by Goldstein [58].

Consider a classical system of particles impingent upon a target as shown in Fig. 6.7. The impact parameter s is defined in the figure; classically the impact parameter is given by $l = mvs = s\sqrt{2mE}$ for a fixed target. If the target is not fixed, we have to replace the mass m by the reduced mass μ. When we solve the problem quantum-mechanically, the angular momentum l becomes quantized.

If we assume that every particle with the same impact parameter will scatter with the same deflection angle θ, then we can calculate the number of incident particles between the rings s and $s + ds$, which should be equal to the number of particles scattered between a given solid angle θ and $\theta + d\theta$:

$$I \times 2\pi s ds = I \times \sigma(\theta) 2\pi \sin\theta d\theta \tag{6.6}$$

$$s ds = \sigma(\theta) \sin\theta d\theta \tag{6.7}$$

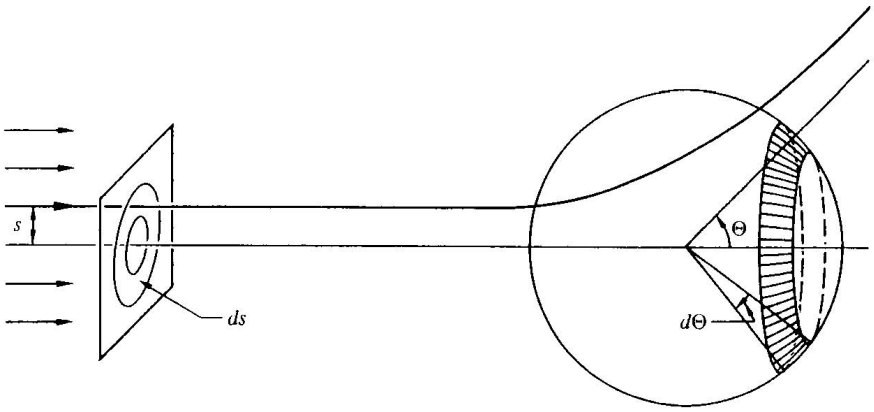

Fig. 6.7 This figure has been reproduced from Goldstein [58], and it shows the scattering of an incident beam of particles by a center of force.

$$\sigma(\theta) = \frac{s}{\sin\theta}\frac{ds}{d\theta} = f(\theta), \tag{6.8}$$

where I is the unit incident intensity. It can be seen that the cross-section diverges for a two different conditions. First, when the $\sin\theta$ term goes to zero. This implies that $\theta = 0$ or π, which corresponds to either an event that resulted in zero deflection angle, or to a back-scattering event. These two processes are referred to as the forward and the backward glory, in analogue to the situation in optics. The second way to get a divergent cross-section is when $ds/d\theta$ goes to infinity, though it is usually seen in models as $d\theta/ds = 0$. This happens when a large number of impact parameters will result in the same deflection angle. At that angle, there are essentially an infinite number of values of s that will contribute to the cross-section, and as those s's are nonzero, the cross-section becomes infinite. This phenomena is called rainbow scattering or normal glory scattering. These glories are shown schematically in Fig. 6.8.

On inspection of Eq. 6.1 one sees that the effective potential of the scattering

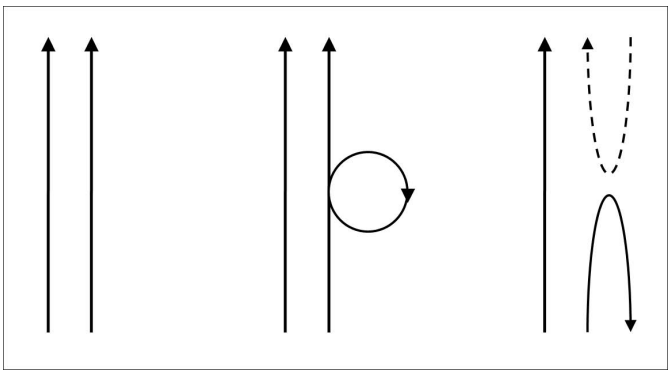

Fig. 6.8 Schematic representation of glory scattering. The left picture represents normal glory scattering, the middle picture is higher-order glory scattering (where the particle orbits before scattering), and the right picture represents hard-sphere backward glory scattering. Here, the solid line is the primary particle and the dashed line is the secondary particle.

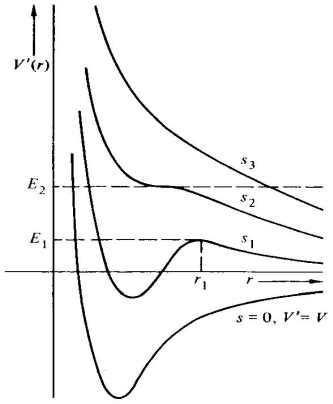

Fig. 6.9 This figure has been reproduced from Goldstein [58], and it shows the effective potential resulting from a combination of a two-body interaction combined with an impact parameter s.

problem is the two-body interaction potential with the addition of a centrifugal term $\sim l^2$ (classical), or $\sim (l+1)l$ (quantum mechanical). Depending on the value of l, or equivalently, on the value of the impact parameter s, this leads to the effective potential shown in Fig. 6.9. Depending on the energy (velocity) of a particle, various

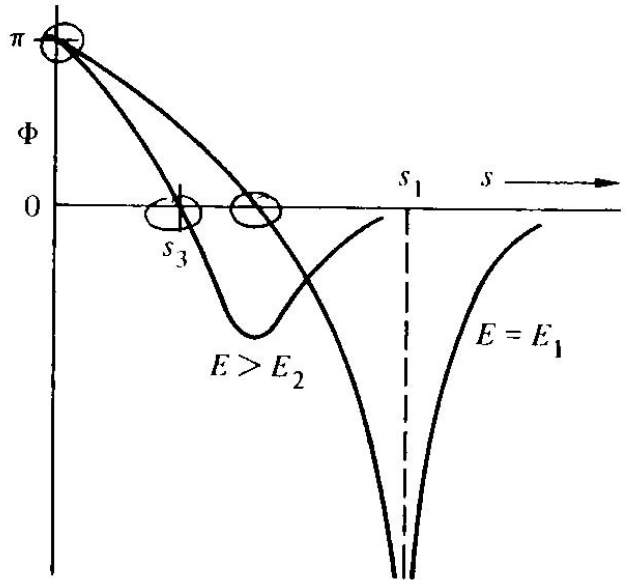

Fig. 6.10 This figure has been reproduced from Goldstein [58], and it shows a schematic of deflection angle ϕ versus impact parameter s for the potential shown in Fig. 6.9. In here the deflection angle can exceed 2π, while the scattering angle θ relevant to the cross section is defined to be less than π.

scenarios will occur. Take for instance the curve marked s_1 in Fig. 6.9 and consider a particle that has energy E_1. This particle has barely enough energy to make it up the 'hump', and its radial velocity will approach zero. However, its angular velocity will not be affected, and the particle can end up orbiting the force center. If it does emerge, it will have been deflected over a very large angle, likely more than 2π. This situation is sketched in Fig. 6.10.

For larger impact parameters, the centrifugal 'hump' becomes less and less important: it will reach some critical value (marked by s_2 and E_2 in Fig. 6.9, above which the effective potential looks like a simple repulsive potential. However, consider the

case for a particle with energy $E > E_2$. We will no longer find any orbiting such as we found for $E = E_1$, and we will more likely encounter a smeared out divergence (the negative minimum between s_3 and s_1 for the curve labeled $E > E_2$ in Fig. 6.10). For the impact parameter corresponding to this minimum we will find a so-called rainbow glory, corresponding to a divergence in $f(\theta)$ caused by $d\theta/ds = 0$. Also, since the angle of deflection must be 180 degrees for an impact parameter of zero (head on collision), there must be a point on the curve where we would find a zero deflection angle. This point is marked s_3 in Fig. 6.10. Here the cross section will also diverge because the term $\sin\theta$ will now be zero. These types of divergences survive in the quantum mechanical treatment, and the positions of the divergences depend on the particle energies. As mentioned before, these glories are important to the cage diffusion mechanism since a zero deflection angle implies that it is easier for a particle to escape its cage. Also, a rainbow glory at a finite scattering angle will be important, depending on whether this angle is larger or smaller than 90 degrees.

Next, we describe the numerical method of solving Eq. 6.1, and we verify that computer programs successfully reproduce published calculations. Then, in the next chapter, we will apply our program to various liquids in order to ascertain the importance of quantum effects to the cage-diffusion mechanism and whether one can observe these effects through neutron scattering experiments.

6.3 Runge-Kutta-Gill method for solving differential equations

The method used to solve the Schrödinger equation is the quartic Runge-Kutta-Gill method, referred to hereafter as the RKG4 method. This method involves an iterative solving of four equations (hence quartic) to estimate the slope of the solution to a

differential equation. The iterative solution is given by [56]

$$y_{n+1} = y_n + \frac{1}{6}[k_1 + (2-\sqrt{2})k_2 + (2+\sqrt{2})k_3 + k_4] + O(h^5), \tag{6.9}$$

where the final value is fed into the initial value for the next iteration, thereby mapping the solution. In the above equation the k's are

$$k_1 = h * f(x_n, y_n) \tag{6.10}$$

$$k_2 = h * f(x_n + \frac{1}{2}h, y_n + \frac{1}{2}k_1) \tag{6.11}$$

$$k_3 = h * f[x_n + \frac{1}{2}, y_n + \frac{1}{2}(-1+\sqrt{2})k_1 + (1 - \frac{1}{2}\sqrt{2})k_2] \tag{6.12}$$

$$k_4 = h * f[x_n + h, y_n - \frac{1}{2}\sqrt{2}k_2 + (1 + \frac{1}{2}\sqrt{2})k_3], \tag{6.13}$$

where h is the iteration step size, x is the variable, y is the solution, and

$$\frac{dy}{dx} = f(x, y) \tag{6.14}$$

for first order differential equations. For second order differential equations, like the Schrödinger equation, it is necessary to break the Schrödinger equation into two coupled ordinary differential equations and solve them simultaneously. The solution to the radial wave equation can be used to calculate the distance d_{max} in space where the potential goes to zero, which is where the wavefunction no longer has an increase in the distance between the zero-points. This solution is calculated for each l value, and $d_{max}(l)$ is obtained. To calculate the phase change η_l, $d_{max}(l)$ goes into

$$\eta_l = \arctan[\frac{j_l(k * d_{max}(l))}{n_l(k * d_{max}(l))}] \tag{6.15}$$

where j_l is the spherical Bessel function, and n_l is the spherical Neumann function. These phase values can then be used to calculate the differential cross-section using [55]

$$\frac{d\sigma(\theta)}{d\Omega} = \frac{1}{4k^2}\{[\sum_l (2l+1)\sin(2\eta_l)P_l(\cos\theta)]^2 + [\sum_l (2l+1)(\cos(2\eta_l)-1)P_l(\cos\theta)]^2\} \tag{6.16}$$

where $P_l(\cos\theta)$ are the Legendre polynomials of $\cos\theta$. The total cross-section it given by

$$\sigma = \frac{4\pi}{k^2}\sum_l (l+\frac{1}{2})\sin^2\eta_l. \tag{6.17}$$

Oscillations in the differential cross-section in Eq. 6.17 at a given k value consistent with experiments indicate that quantum mechanics should be used. A potential and sample material from Bernstein [57] was used as a trial, and the results are reproduced below.

6.4 Bernstein trial for RKG4 approximation

Using the Lennard-Jones potential [referred to as L-J (12, 6)]

$$V(r) = 4\epsilon((\sigma/r)^{-12} - (\sigma/r)^{-6}), \tag{6.18}$$

where $r = \sigma$ corresponds to the zero of the potential, and ϵ is the attractive well-depth. Switching to dimensionless variables $x = \sigma/r$ and $V(x) = V(r)/\epsilon$, the Schrödinger equation is iteratively solved using the Runge-Kutta-Gill approximation method. The Schrödinger equation used is

$$\frac{d^2y}{dx^2} + (K - Z)By = 0, \tag{6.19}$$

where $Z = V(x) + \frac{l(l+1)}{Bx^2}$ and $B = (2\mu/\hbar^2)\epsilon\sigma^2$; μ is the reduced mass relevant to lquid atoms that are not fixed in position. Above, $K = E/\epsilon = A^2/B$ where E is the initial relative kinetic energy, $A = k\sigma$ a dimensionless parameter, and $k = \sqrt{2\mu E/\hbar^2}$. Using Bernstein's [57] B value of 125.0 representing hydrogen molecules being scattered by

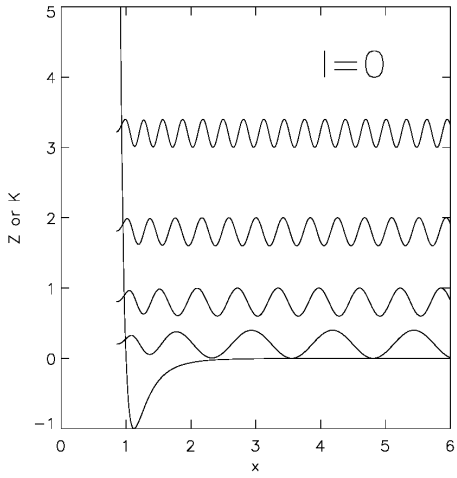

Fig. 6.11 l=0 radial wave solutions at K-values 0.2, 0.8, 1.8, and 3.2 to the Schrödinger equation as well as the reduced effective potential.

Mercury atoms, the solutions of the Schrodinger equation for l values 0, 10, 15, and 20 are reproduced excellently in Figs. 6.11-6.14. For an A value of 5, corresponding to K=0.2, l values 10, 11, 12, and 15 are reproduced in Fig. 6.15 to show tunneling through a centrifugal barrier. A variety of solutions were calculated for different A and l values. The phase shift, given by

$$\eta_l = arctan[j_l(Ax_n)/n_l(Ax_n)] \tag{6.20}$$

where j_l and n_l are the radial Bessel and Neumann functions, respectively, and x_n is the distance where the potential becomes negligible, is reproduced in Figs. 6.16 and 6.17.

Using the previously calculated phase shifts, the differential cross-section per angle can be calculated by

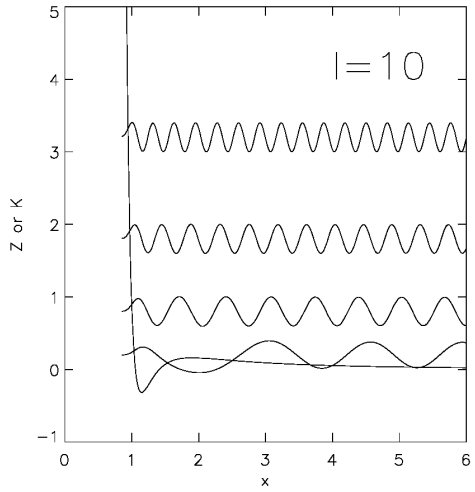

Fig. 6.12 l=10 radial wave solutions at K-values 0.2, 0.8, 1.8, and 3.2 to the Schrödinger equation as well as the reduced effective potential.

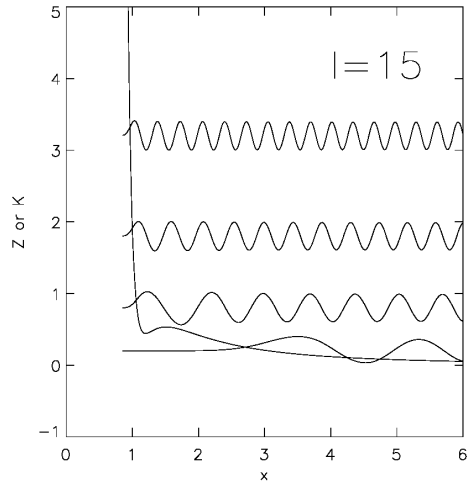

Fig. 6.13 l=15 radial wave solutions at K-values 0.2, 0.8, 1.8, and 3.2 to the Schrödinger equation as well as the reduced effective potential.

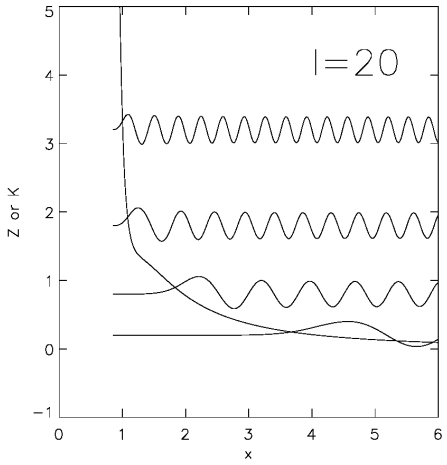

Fig. 6.14 l=20 radial wave solutions at K-values 0.2, 0.8, 1.8, and 3.2 to the Schrödinger equation as well as the reduced effective potential.

$$\frac{d\sigma(\theta)}{d\Omega} = \frac{1}{4k^2}\{[\sum_l (2l+1)\sin(2\eta_l)P_l(\cos\theta)]^2 + [\sum_l (2l+1)(\cos(2\eta_l)-1)P_l(\cos\theta)]^2\}. \tag{6.21}$$

The differential cross-section versus θ (a measure of $f(\theta)$ is reproduced in Fig. 6.18. In this figure one can clearly observe the various glories.

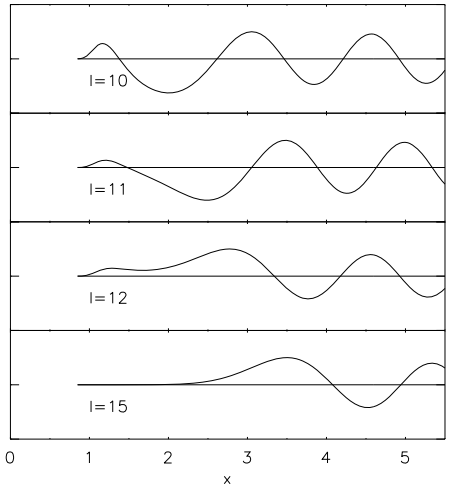

Fig. 6.15 Shown is the presence of an abrupt change in phase shift corresponding to barrier penetration between $l = 11$ and $l = 12$ with A=5.

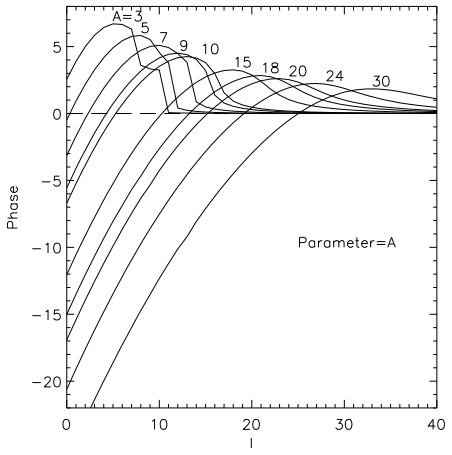

Fig. 6.16 The calculated phase constant vs. the angular momentum quantum number for various A-values.

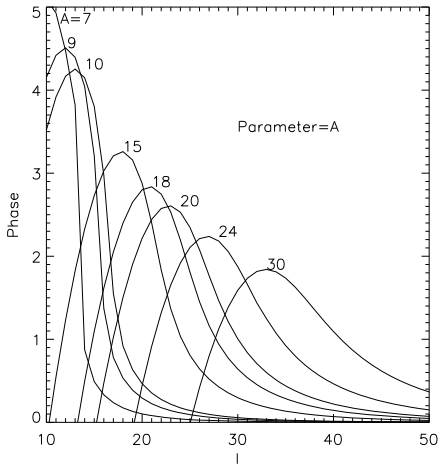

Fig. 6.17 Zoom of Fig. 6.16.

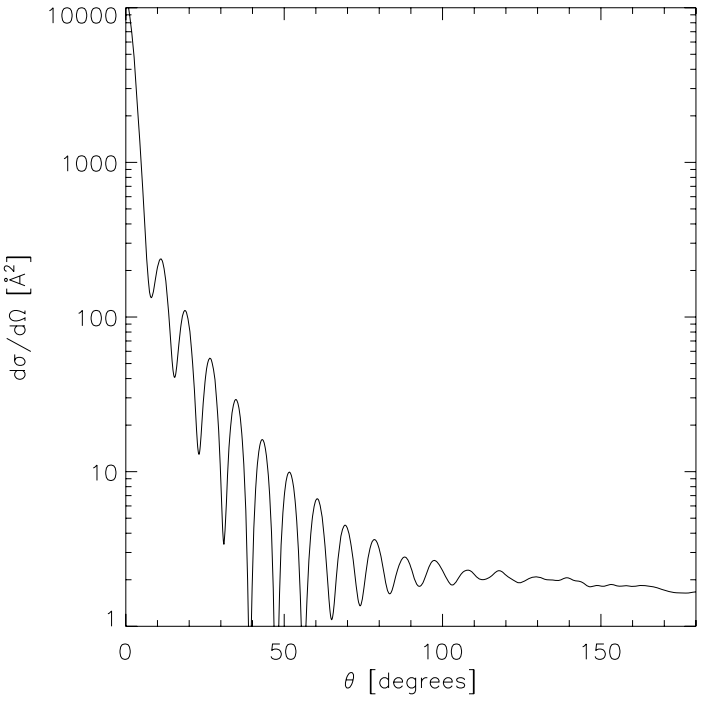

Fig. 6.18 Quantum calculation of differential cross-section vs. angle at A=18.

7
Quantum interference effects in various liquid metals

7.1 Introduction

Using the RGK4 method as outlined in the previous chapter, we calculated the phase shifts and corresponding cross-sections relevant to the cage-diffusion process for various potentials over a wide velocity range for liquid He, Li, Na, Ga, and Pb. The purpose of this chapter is not to find perfect agreement with linewidth oscillations observed in neutron scattering experiments, rather the goal is to ascertain whether quantum interference effects are relevant or not. In order to obtain exact agreement one would require detailed knowledge of the interaction potential, something that is not necessarily known. For instance, the interaction potentials relevant to liquid gallium differ by a as much as a factor of 10 in well depth, from $\sim$ 300 K to 4000 K.

From Mott and Massey [55], the cross-section is given by

$$\sigma = \frac{4\pi}{k^2} \sum_{l}^{\infty} (2l+1) \sin^2 \eta_l, \tag{7.1}$$

where η_l is the phase shift at angular momentum l. From this one can also calculate the cross-sections most relevant to diffusion and viscosity, given by

$$\sigma_D = \frac{4\pi}{k^2} \sum_{l}^{\infty} (l+1) \sin^2(\eta_{l+1} - \eta_l) \tag{7.2}$$

and

$$\sigma_{visc} = \frac{2\pi}{k^2} \sum_{l}^{\infty} \frac{(l+1)(l+2)}{l+\frac{3}{2}} \sin^2(\eta_{l+2} - \eta_l), \tag{7.3}$$

respectively. In each of these cases, the summations go from zero to infinity, but the RKG4 program cannot calculate an infinite number of l values. There is an upper limit to how many l values are used in the summation, based on the size of the reduced mass of the system and the relative velocity ($v = \frac{k\hbar}{m}$). As the mass increases, the number of l values with non-zero phase shifts increases.

An approximate way to calculate the phase shifts is to change the summation to an integral [55],

$$\eta_l = -\frac{1}{2} \int_{(l+1/2)/k}^{\infty} \frac{U(r)}{\sqrt{k^2 - \frac{(l+1/2)^2}{r^2}}} dr, \tag{7.4}$$

where $U(r) = 2\mu V(r)/\hbar^2$, V(r) is the pair potential, μ is the reduced mass, and k is the wave number. This integral method is expected to be most accurate for large reduced masses or high relative velocities, where it would be unfeasible to calculate phase values at very high l values. We use the method for a few values of k to obtain its exact range of validity through comparison to the RKG4 method.

In addition, for identical particles it is necessary to symmetrize the scattering length $f(\theta)$ [60] between the incoming and scattering particle:

$$f_{\pm}(\theta) = \frac{1}{\sqrt{2}}[f(\theta) \pm f(\theta_B)]. \tag{7.5}$$

The $\sqrt{2}$ factor yields the required normalization, and θ_B is the back-scattering angle given by $\theta_B = \pi - \theta$. Since the scattering length depends on the scattering angle through the Legendre polynomial we find

$$P_l(\cos\theta_B) = e^{i\pi l} P_l(\cos\theta). \tag{7.6}$$

This means that for the + term in the scattering length $f_{\pm}(\theta)$, the only contribution comes from the even l terms, as the odd terms will cancel out. So, the cross-section would be

$$\sigma_{+} = \frac{4\pi}{k^2} \sum_{l=0,2,\ldots}^{\infty} (l + 1/2)(1 - \cos 2\eta_l), \tag{7.7}$$

and similar for σ_{-}, but with only the odd terms surviving. Each of these conventions has an associated name: the Bose case is when only the even terms apply, the Fermi case is when only the odd terms apply, and the classical case is when both the even and odd terms apply. Each case will be shown in the following sections as they produce different results for the Glory oscillations.

7.2 Liquid helium

Presented are the phase shift calculations of a liquid helium-helium scattering event using a LJ(12,6) potential with the parameters $\epsilon = 10.8$ K and $\sigma = 2.56\mathring{A}$. We chose helium since this case nicely illustrates the importance of Bose versus Fermi statistics. First, we calculated the $l = 0$, 2, 4 terms (relevant to ^{4}He) of the phase shifts at relative velocities from 10-350 m/s to show the maxima and minima in the cross-section corresponding to glory scattering (see Fig. 7.1).

In order to get a handle on how important the attractive part of the potential is, we recalculated with only the repulsive part of the LJ(12,6) potential, effectively making the scattering nearly a hard-sphere scattering event (see Fig. 7.2). Interesting to note is that the total cross-section becomes nearly constant over the plotted velocity range when the potential is purely repulsive. Thus, the observed glories originate from events shown in Fig. 6.10 (the curve labeled $E > E_2$). From a math standpoint, the slope of

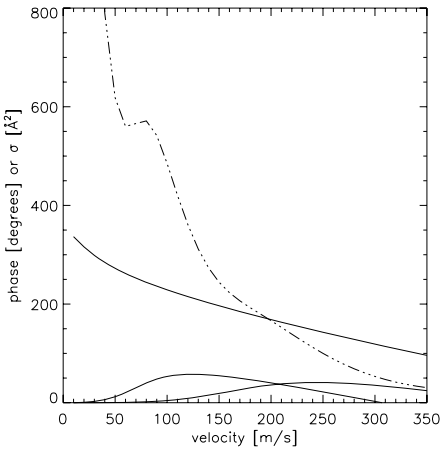

Fig. 7.1 Shown are the first three even l terms of the phase (solid lines) using the LJ(12,6) potential. The cross-section (dotted line) is calculated to show the local minimum which indicates glory scattering.

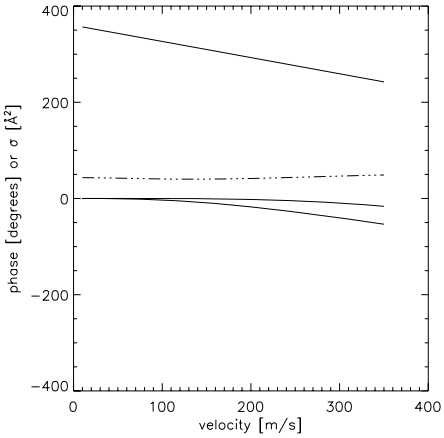

Fig. 7.2 Shown are the first three even l terms of the phase (solid lines) using the repulsive part of the LJ(12,6) potential. The cross-section (dotted line) is also shown.

the $l = 0$ term is less steep with the repulsive potential, so the $\sin^2 \eta_0$ term changes even slower, yielding a nearly constant cross-section.

Next, all phase shifts for $l = 0 \rightarrow 51$ were calculated and the cross-sections (total, diffusion, and viscosity) were determined. The results are shown in Fig. 7.3. It is clear

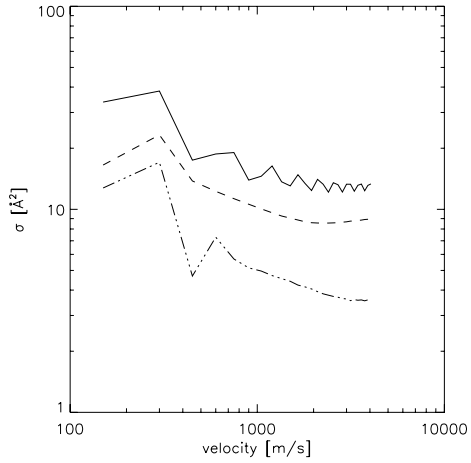

Fig. 7.3 Shown are the total cross-section (solid line), diffusion cross-section (dashed line), and viscosity cross-section (dotted-dashed line) for liquid helium using Bose statistics. Note the glory oscillations in the total cross-section.

that the cross-section oscillates with the velocity. To compare the velocity scale to a neutron scattering experiment one should use $mv = \hbar k$, which for helium would yield that 1000 m/s corresponds to a momentum transfer of 6.3 Å^{-1}. This figure does not reproduce exactly the calculated cross-sections shown in Fig. 6.2 since we used a slightly different interaction potential; however, the period of oscillation exactly matches. Also note that only relatively small changes in the total cross sections amplitude give rise to measurable oscillations in a neutron scattering experiment.

Finally, the total cross-sections are shown for the different statistics, namely Bose, Fermi, and classical (see Fig. 7.4). Notice that the oscillations in the Bose case are out of phase with the oscillations in the Fermi case (^{3}He).

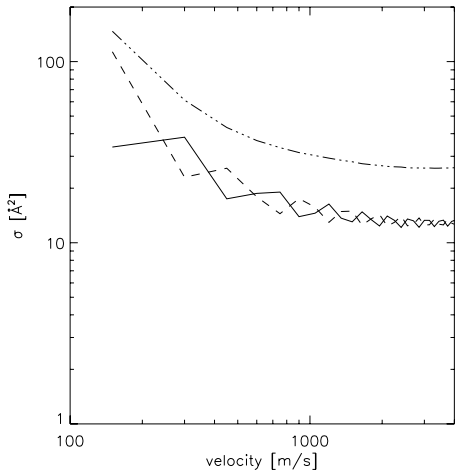

Fig. 7.4 Shown are the total Bose cross-section (solid line), total Fermi cross-section (dashed line), and total classical cross-section (dotted-dashed line) for liquid helium. Note that glory scattering is present in the Bose and Fermi cases, but not in the classical case.

7.3 Liquid lithium

Presented are the phase shift calculations of a liquid lithium-lithium scattering event using the interaction potential published by Dalgic *et al.* [61]. First, the phase shifts for $l = 0 \rightarrow 71$ were calculated and the cross-sections (total, diffusion, and viscosity) were determined (see Fig. 7.5). As was the case for liquid helium, there are oscillations present, indicating glories.

Next, the total cross-sections are shown in Fig. 7.6 for the different statistics (^{6}Li and ^{7}Li). For ^{6}Li, 500 m/s would correspond to $k = 4.7\text{Å}^{-1}$ in a neutron scattering experiment.

Finally, the two methods for finding the phase shifts, namely the RKG4 method and the integral method, are compared in Figs. 7.7, 7.8, 7.9, 7.10 for various relative velocities. Comparing the two methods, we can see that the impact parameters b=

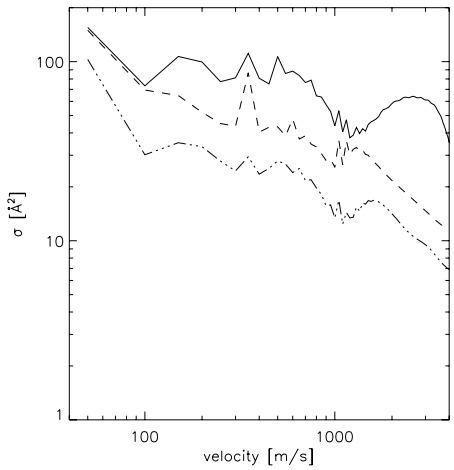

Fig. 7.5 Shown are the total cross-section (solid line), diffusion cross-section (dashed line), and viscosity cross-section (dotted-dashed line) for liquid lithium using Bose statistics.

$(l + \frac{1}{2})/k)$ when the phase shift goes to zero are similar for the two methods. We use the notation b here for the quantum mechanical impact parameter to distinguish it from its classical equivalent s. It can also be seen from these figures that where the integral method produces random phase shifts for smaller impact parameters, the RKG4 method does not. This shows that the integral method underestimates the correlations present in the quantum mechanical problem. When it comes to calculating total-cross sections, the integral method would yield the wrong results since it would essentially produce and average value of 1/2 for the $\sin^2\eta_l$ term in the low b-region, in disagreement with the exact quantum mechanical calculation. Thus, for a light element like Li, the integral method is of limited use.

7.4 Liquid sodium

Presented are the phase shift calculations of a liquid sodium-sodium scattering event using the potential published by Dalgic *et al.* [61]. First, the phase shifts for $l =$

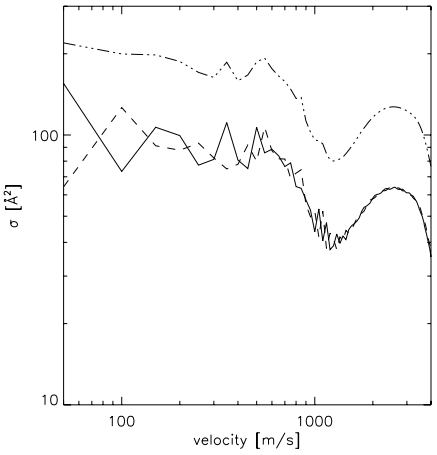

Fig. 7.6 Shown are the total Bose cross-section (solid line), total Fermi cross-section (dashed line), and total classical cross-section (dotted-dashed line) for liquid lithium. Note that a mixture of ^{6}Li and ^{7}Li would not show glory oscillations at the smaller velocities, as opposed to Li consisting of only one isotope.

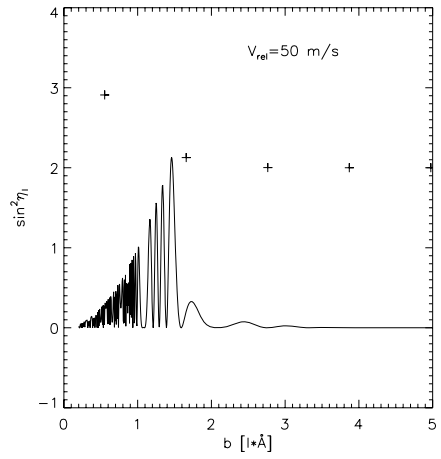

Fig. 7.7 Shown are the two methods of calculating the phase shifts for liquid lithium at a relative velocity of 50 m/s. The integral method is shown as a solid line and the RKG4 method is shown as data points. The RKG4 method is raised by two units to distinguish the plots.

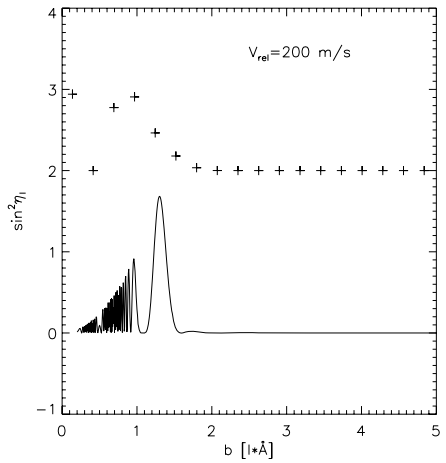

Fig. 7.8 Same as Fig. 7.7 except at a relative velocity of 200 m/s.

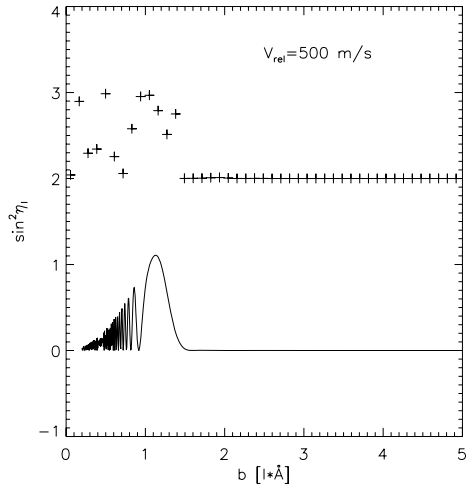

Fig. 7.9 Same as Fig. 7.7 except at a relative velocity of 500 m/s.

$0 \rightarrow 121$ were calculated and the cross-sections (total, diffusion, and viscosity) were evaluated (see Fig. 7.11). As in He and Li, glory oscillations can be observed despite the much higher Na mass. For sodium, 100 m/s corresponds to k= 3.6 Å^{-1} in a neutron

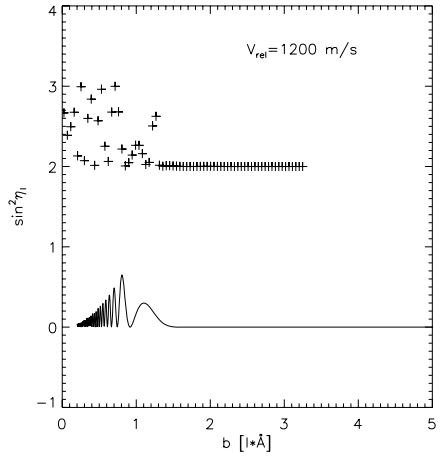

Fig. 7.10 Same as Fig. 7.7 except at a relative velocity of 1200 m/s.

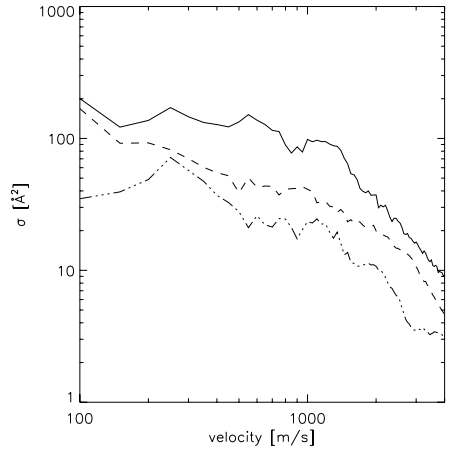

Fig. 7.11 Shown are the total cross-section (solid line), diffusion cross-section (dashed line), and viscosity cross-section (dotted-dashed line) for liquid sodium using Bose statistics.

scattering experiment.

Next, the total cross-sections are shown for the different statistics (Fig. 7.12). Compared to Li, it would appear that the difference between Bose and Fermi statistics is getting smaller.

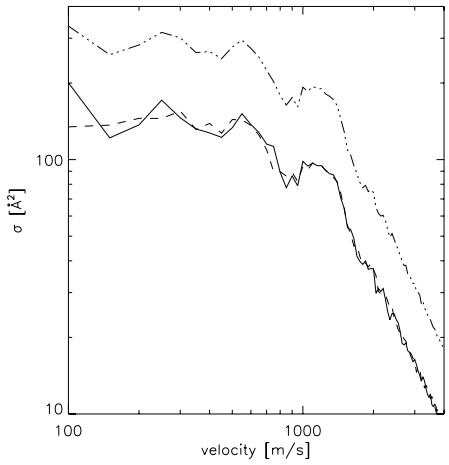

Fig. 7.12 Shown are the total Bose cross-section (solid line), total Fermi cross-section (dashed line), and total classical cross-section (dotted-dashed line) for liquid sodium.

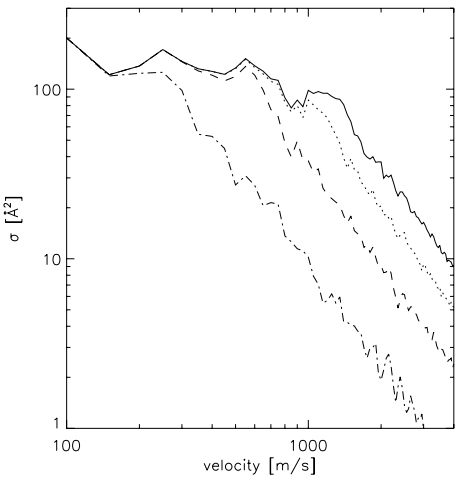

Fig. 7.13 Shown is the total cross-section of liquid sodium for Bose statistics. The solid line is taking up to 121 l values. The dotted line is taking up to 90 l values. The dashed line is taking up to 60 l values. The dashed-dotted line is taking up to 30 l values.

Given the much larger mass of Na, we next calculate up to what value of l has to be included in the calculations to obtain an accurate cross-section. This is shown in Fig. 7.13. Note that at lower relative velocities, the cross-section does not differ when

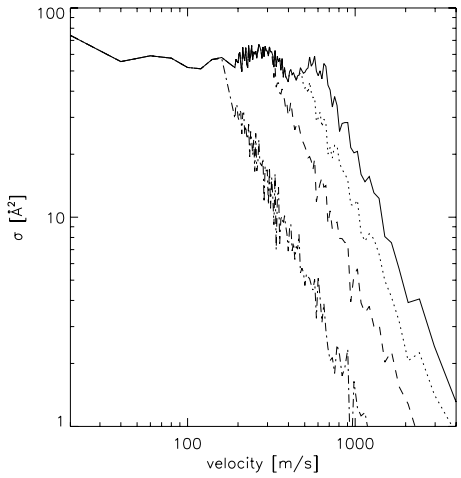

Fig. 7.14 Shown is the total cross-section of liquid gallium for Bose statistics. The solid line is taking up to 141 l values. The dotted line is taking up to 105 l values. The dashed line is taking up to 70 l values. The dashed-dotted line is taking up to 35 l values.

fewer l values are taken into account, but that the effects become very noticeable at the higher velocities.

7.5 Liquid gallium

Presented are the phase shift calculations of a liquid gallium-gallium scattering event using the potential published by Baskes *et al.* [62]. We show the results for the total cross-section for the Bose case in Fig. 7.14. As was the case for liquid sodium, depending on the relative velocity of the colliding particles, more and more l-terms have to be taken into account in order to arrive at an accurate value. For liquid Ga, 30 m/s would correspond to $k = 3.3\text{Å}^{-1}$ in neutron scattering experiment (such as the one shown in Fig 6.5).

It is clear from this figure that glory oscillations are present in the range relevant to neutron scattering experiments, and the period of oscillations is such that it would

definitely affect any oscillations present to classical interaction mechanisms. Also, the amplitude of the oscillations is comparable to the case of liquid helium, so that we have every reason to expect that these oscillation would make their presence felt in the characteristic linewidth as observed in neutron scattering experiments.

While it might be counterintuitive that a heavy element like Ga should show the effects of quantum oscillations, the key to these scattering events that determine the cage diffusion process is that only the relative velocities are relevant. Because of the increased mass, for a given amount of momentum transfer in a neutron scattering experiment, lower and lower relative velocities become important in the quantum mechanical scattering problem (through the relation $mv = \hbar k$), making quantum effects more pronounced.

Finally, the two methods for finding the phase shifts, namely the RKG4 method and the integral method, are compared for various relative velocities. The results are shown in Figs. 7.15, 7.16, 7.17, 7.18. Comparing the two methods, we can see that the integral method would once again yield inaccurate results for relative velocities relevant to neutron scattering experiments.

7.6 Liquid lead

As of now, the RKG4 approach does not work for liquid Pb due to limitations of the code. The larger the relative mass, the more η_l values must be calculated while the solution becomes more and more dependent on the smallest r value used in solving the Schrödinger equation. The integral approach might work, but given the results for Ga it is unclear whether the results can be trusted. However, given published data showing oscillations in the neutron scattering linewidth for momentum transfers well beyond

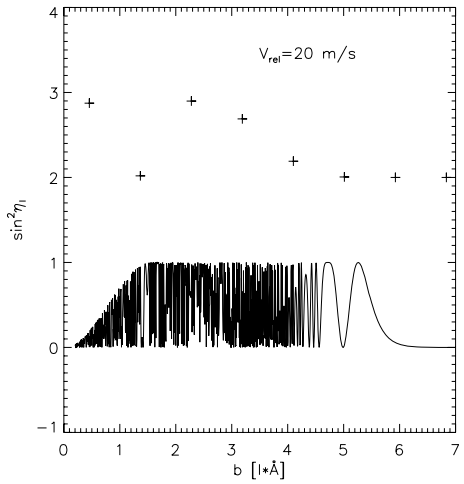

Fig. 7.15 Shown are the two methods of calculating the phase shifts for liquid gallium at a relative velocity of 20 m/s. The integral method is shown as a solid line and the RKG4 method is shown as data points. The RKG4 method is raised by two units to distinguish the plots.

the region where such oscillations are to be expected based upon classical dynamics (see Fig. 7.19), it would appear that quantum interference effects are always relevant to inter-atomic collisions as they are being probed in neutron scattering experiments.

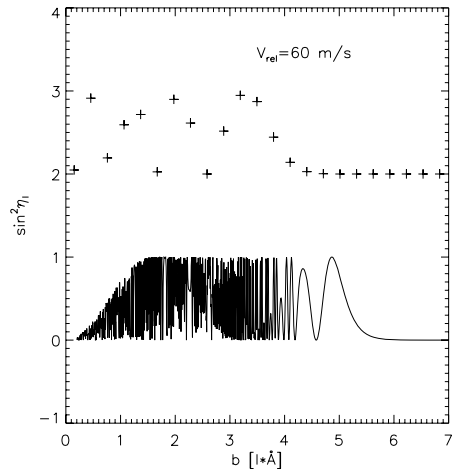

Fig. 7.16 Same as Fig. 7.15 except at a relative velocity of 60 m/s.

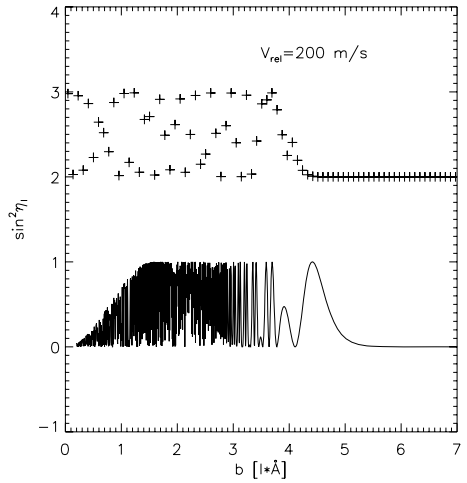

Fig. 7.17 Same as Fig. 7.15 except at a relative velocity of 200 m/s.

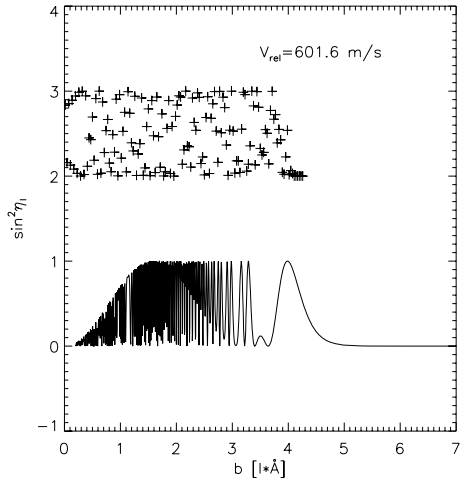

Fig. 7.18 Same as Fig. 7.15 except at a relative velocity of 600 m/s.

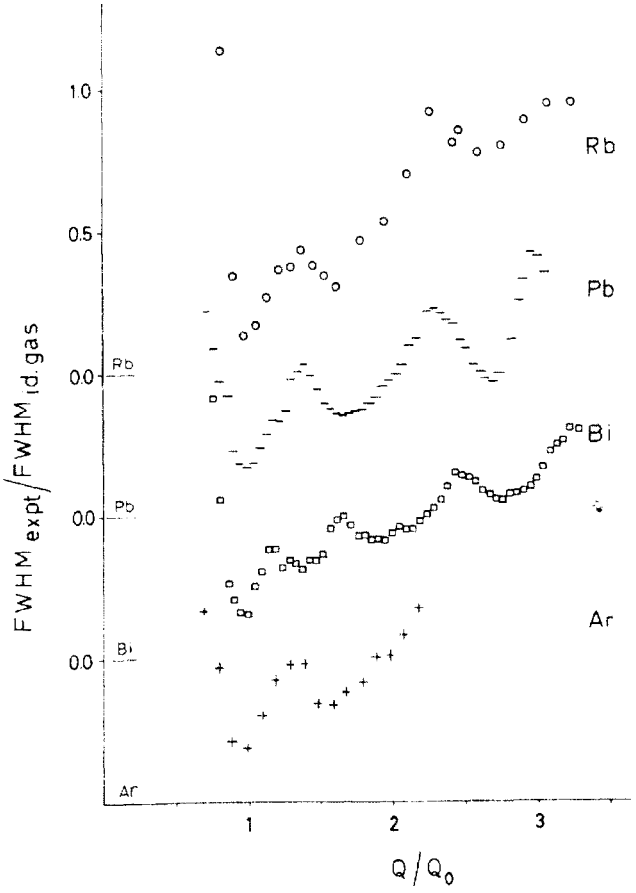

Fig. 7.19 Figure reproduced from Scopigno [63]. The figure shows that even the very heavy elements like Pb do show oscillations in the neutron scattering linewidth, indicative of quantum interference affects. In this figure Q_0 is the position of the first maximum of the static structure factor.

8
Immediate outlook

8.1 Fluctuating magnetic moments in other liquid metals

Even though we did not find evidence of a magnetic moment in liquid gallium, that does not mean that this magnetic moment does not exist in other liquid metals. In fact, it is likely that they do exist since the very same method that was used to identify the unexplained contribution to the cross-section in liquid Ga as being caused by multiple scattering events failed to explain the additional scattering in liquid mercury. Inelastic neutron scattering studies on Hg with a polarized setup would be ideal; however, reactors within a containment building would not permit such experiments. The next likely candidate would be liquid lead. It has a relatively low melting point, and unlike mercury, it does not present a problem when it comes to safety issues.

8.2 Quantum interference effects and their influence on the cage-diffusion mechanism

Overall, it seems that quantum mechanical interference effects should play a role in the dynamics of liquid metals when it comes to the cage-diffusion mechanism; the observed oscillations in liquid gallium are at least partly attributable to glory oscillations. Whether inclusion of the glory oscillations in the analysis of the liquid Ga data would remove the need to use unphysical parameters when describing the liquid as a purely classical liquid is unclear at present. In order to resolve this issue, we need

to carry out a range of calculations for various interaction potentials and determine whether they would all yield glory oscillations of similar periods.

Our study of the importance of quantum interference effects in classical liquids does open up new avenues of research. First, it might be possible to test models for various interaction potentials by performing neutron scattering experiments at very high momentum transfers. For the potential to give a correct description of the dynamics of the liquid, it should be able to reproduce the observed oscillations in a neutron scattering experiment. Second, it should be possible to develop a better understanding of the cage-diffusion mechanism that is most important to the relaxation of short-lived excitations in liquids. This requires a more detailed analysis than what we have presented in the preceding chapter; it would require that one takes the full $f(\theta)$ into account, not merely the total cross-section, and that one scrutinizes all the glories that show up in this differential cross-section. However, all the computer code to be able to do such a detailed study is now in place.

References

[1] L.E. Bove, F. Sacchetti, C. Petrillo, B. Dorner, F. Formisano, and F. Barocchi, Phys. Rev. Lett. **87**, 215504 (2001).

[2] T. Scopigno, R. DiLeonardo, L. Comez, A.Q.R. Baron, D. Fioretto, and G. Ruocco, Phys. Rev. Lett. **94**, 155301 (2005).

[3] G.L. Squires. *Introduction to the Theory of Thermal Neutron Scattering*. New York: Dover, 1996.

[4] Y.S. Badyal, U. Bafile, K. Miyazaki, I.M. de Schepper, and W. Montfrooij, Phys. Rev. **E68**, 061208 (2003).

[5] M. Patty, K. Schoen, and W. Montfrooij, Phys. Rev. **E73**, 021202 (2006).

[6] U. Balucani and M. Zoppi, *Dynamics of the Liquid State* (Clarendon Press, Oxford, 1994), and references therein.

[7] L.E. Bove, F. Sacchetti, C. Petrillo, B. Dorner, F. Formisano, M. Sampoli, and F. Barocchi, Philos. Mag. **82**, 365 (2002); Journ. of Non-Cryst. Solids **307-310**, 842 (2002).

[8] K. Tamura, M. Inui, I. Nakaso, Y. Oh'ishi, K. Funakoshi, and W. Utsumi, J. Phys.: Condens. Matt. **10**, 11405 (1998).

[9] K. Tamura and S. Hosokawa, J. Phys.: Condens. Matt. **6**, A241 (1994).

[10] T. Bodensteiner, Chr. Morkel, W. Glaeser, and B. Dorner, Phys. Rev. A **45**, 5709 (1992).

[11] L.E. Bove, F. Sacchetti, C. Petrillo, and B. Dorner, Phys. Rev. Lett. **85**, 5352 (2000).

[12] M.J. Huijben and W. van der Lugt, J. Phys. F.: Met. Phys. **6**, L225 (1976).

[13] C. Cabrillo, F.J. Bermejo, M. Alvarez, P. Verkerk, A. Maira-Vidal, S.M. Bennington, and D. Martin, Phys. Rev. Lett. **89**, 075508 (2002).

[14] A.G. Novokov, M.N. Ivanovskii, V.V. Savostin, A.L. Shimkevich, O.V. Sobolev, and M.V. Zaezjev, J. Phys.: Condens. Matt. **8**, 3525 (1996).

[15] L.E. Bove, B. Dorner, C. Petrillo, F. Sacchetti, and J.-B. Suck, Phys. Rev. B. **68**, 024208 (2003).

[16] J.R.D. Copley and J.M. Rowe, Phys. Rev. A **9**, 1656 (1974).

[17] D.I. Page, P.A. Egelstaff, J.E. Enderby, and B.R. Wingfield, Phys. Lett. **29A**, 296 (1969).

[18] Chr. Morkel and W.-C. Pilgrim, Journ. Non-Cryst. Solids **312-314**, 128 (2002).

[19] B.P. Alblas, W. van der Lugt, J. Dijkstra, W. Geertsma, and C. van Dijk, J. Phys. F.: Met. Phys. **13**, 2465 (1983).

[20] A. Stangl, C. Morkel, U. Balucani, and A. Torcini, J. Non-Crys. Sol. **205-207**, 402 (1996).

[21] U. Balucani, A. Torcini, A. Stangl, and C. Morkel, Physica Scripta. **T75**, 13 (1995).

[22] W.-C. Pilgrim, S. Hosokawa, H. Saggau, H. Sinn, and E. Burkel, J. Non-Crys. Sol. **250-252**, 96 (1999).

[23] T. Scopigno, U. Balucani, G. Ruocco, and F. Sette, Phys. Rev. E. **65**, 031205 (2002).

[24] A. Torcini, U. Balucani, P.H.K. de Jong, and P. Verkerk, Phys. Rev. E. **51**, 3126 (1995).

[25] H. Sinn and E. Burkel, J. Phys. Cond.Mat. **8**, 9369 (1996).

[26] P.H.K. de Jong, P. Verkerk, and L.A. de Graaf, J. Phys.: Condens. Matt. **6**, 8391 (1994).

[27] T. Scopigno, U. Balucani, G. Ruocco, and F. Sette, Phys. Rev. Lett. **85**, 4076 (2000).

[28] S.J. Cocking and P.A. Egelstaff, J. Phys. C. (Proc. Phys. Soc.). **1**, 507 (1968).

[29] D.M. North, J.E. Enderby, and P.A. Egelstaff, J. Phys. C**1**, 784 (1968).

[30] O. Söderström, J.R.D. Copley, J.-B. Suck, and B. Dorner, J. Phys. F.: Metal Phys. **10**, L151 (1980).

[31] H.T.J. Reijers, W. van der Lugt, C. van Dijk, and M.-L. Saboungi, J. Phys.: Condens. Matt. **1**, 5229 (1989).

[32] M. Dzugutov, K.-E. Larsson, and I. Ebbsjo, Phys. Rev. A. **38**, 3609 (1988).

[33] N. Iqbal, N.H. van Dijk, V.W.J. Verhoeven, W. Montfrooij, T. Hansen, L. Katgerman, and G.J. Kearley, Acta Materialia. **51**, 4497-4504 (2003).

[34] IAMP database of SCM-LIQ, Tohoku University. Available at: http://www.tagen.tohoku.ac.jp/general/building/iamp/database/scm/LIQ/sq.html.

[35] T. Scopigno, U. Balucani, G. Ruocco, and F. Sette, Phys. Rev. E **63**, 011210 (2000).

[36] M.C. Bellissent-Funel, P. Chieux, D. Levesque, and J.J. Weis, Phys. Rev. A. **39**, 6310 (1989).

[37] L.E. Bove, F. Formisano, F. Sacchetti, C. Petrillo, A. Ivanov, B. Dorner, and F. Barocchi, Phys. Rev. B **71**, 014207 (2005).

[38] L. E. Bove, F. Sacchetti, C. Petrillo, F. Formisano, M. Sampoli, and F. Barocchi, Philos. Mag. **84**, 1609 (2004).

[39] T. Scopigno, A. Filipponi, M. Krisch, G. Monaco, G. Ruocco, and F. Sette, Phys. Rev. Lett. **89**, 255506 (2002).

[40] H. Fredrikze, Phys. Rev. A **36**, 2272 (1987).

[41] P.A. Egelstaff, N.H. March, and N.C. McGill, Can. J. Phys. **52**,1651 (1974).

[42] I.M. de Schepper, E.G.D. Cohen, and M.J. Zuilhof, Phys. Lett. **101A**, 399 (1984).

[43] E.G.D. Cohen, P. Westerhuijs, and I.M. de Schepper, Phys. Rev. Lett. **59**, 2872 (1987).

[44] P.N. Pusey, H.N.W. Lekkerkerker, E.G.D. Cohen, and I.M. de Schepper, Physica A**164**, 12 (1990).

[45] R. Verberg, I.M. de Schepper, and E.G.D. Cohen, Europhys. Lett. **48**, 397 (1999); Phys. Rev. E**61**, 2967 (2000).

[46] V.F. Sears, Adv. Phys. **24**, 1 (1975).

[47] *Handbook of Chemistry and Physics*, 79^{th} edition, CRC, 1998-1999.

[48] The relative intensity I_{rel} of the cage diffusion mode, as observed in MD simulation, is given at low q values by $q\Delta^2/10$ with Δ the radius of the cage. This is true for both the coherent and incoherent contribution since it is the form factor effect: $I_{rel} = \int_{cage} e^{i\mathbf{q}\cdot\mathbf{r}} d\mathbf{r}/V_{cage}$.

[49] G.S. Dubey, R. Bansal and K.N. Pathak, J. Phys. C: Solid St. Phys. **13**, 6119 (1980).

[50] T. Gaskell, J. Phys. F: Met. Phys. **16**, 381 (1986).

[51] N.M. Keita and S. Steinemann, J. Phys. C: Solid State Phys. **11**, 4635 (1978).

[52] V.F. Sears, Neutron News **3**(3), 29 (1992); also http://www.ncnr.nist.gov/resources/n-lengths/.

[53] F.J. Bermejo, I. Bustinduy, C. Cabrillo, S.J. Levitt, and J.W. Taylor, Phys. Rev. Lett. **95**, 269601 (2005).

[54] T. Scopigno, R.Di Leonardo, L. Comez, A.Q.R. Baron, D. Fioretto, G. Ruocco, and W. Montfrooij, Phys. Rev. Lett. **95**, 269602 (2005).

[55] N.F. Mott and H.S.W Massey, *The Theory of Atomic Collisions*. Oxford: Clarendon Press, 1965.

[56] M. Abramowitz and I.A. Stegun (Editors), *Handbook of Mathematical Functions with Formulas, Graphs, and Mathematical Tables, 9^{th} printing*. New York: Dover, 1972.

[57] R.B. Bernstein, J. Chem. Phys. **33** #3, 795 (1960).

[58] H. Goldstein, *Classical Mechanics, Second Edition*. Addison-Wesley Publishing Company, Inc., 1980.

[59] K.H. Anderson, G.W. Sterling, and H.R. Glyde, Phys. Rev. B **56**, 8978 (1997).

[60] R.K.B. Helbing, J. Chem. Phys. **50**, 493 (1969).

[61] S. Dalgic, S. Dalgic, and M. Tomak, Tr. J. of Physics **22**, 47 (1998).

[62] M.I. Baskes, S.P. Chen, and F.J. Cherne, Phys. Rev. B **66**, 104107 (2002).

[63] T. Scopigno, G. Ruocco, and F. Sette, Rev. Mod. Phys. **77**, 881 (2005).

Appendix A
Differential cross-section

A.1 Fermi's Golden Rule

Fermi's Golden Rule is given by

$$\sum_{\mathbf{k}' ind\Omega} W_{\mathbf{k},\lambda\rightarrow\mathbf{k}',\lambda'} = \frac{2\pi}{\hbar}\rho_{\mathbf{k}'}| < \mathbf{k}'\lambda'|V|\mathbf{k}\lambda > |^2, \tag{A.1}$$

where $\rho_{\mathbf{k}'}$ is the number of momentum states in the solid angle $d\Omega$ per unit energy range for neutrons in a state $\mathbf{k}'$ and where

$$< \mathbf{k}'\lambda'|V|\mathbf{k}\lambda >= \int \psi^*_{\mathbf{k}'}\chi^*_{\lambda'}V\psi_{\mathbf{k}}\chi_{\lambda}d\mathbf{R}d\mathbf{r}. \tag{A.2}$$

In this case, $d\mathbf{R} = d\mathbf{R}_1 d\mathbf{R}_2 ... d\mathbf{R}_N$, where $d\mathbf{R}_i$ is a volume element of the i^{th} particle in the sample and $d\mathbf{r}$ is a volume element of the neutron. Also, ψ is the wavefunction of the neutron and χ is the wavefunction associated with the scattering system.

A.2 Density of states

$\rho_{\mathbf{k}'}$ can be further specified by the relation that the number of states in $d\Omega$ with an energy between E' and E'+dE' is equal to the number of wavevector points within the volume element $k'^2 dk' d\Omega$. So,

$$\rho_{\mathbf{k}'} dE' = k'^2 dk' d\Omega = \frac{1}{\text{Volume}_{cell}} k'^2 dk' d\Omega. \tag{A.3}$$

dE' can be specified from the kinetic energy term $E' = (\hbar^2/2m)k'^2$. Differentiating gives $dE' = (\hbar^2/m)k'dk'$. So,

$$\rho_{\mathbf{k}'} = \frac{m}{\hbar^2}\frac{1}{\text{Volume}_{cell}}k'd\Omega = \frac{\text{Volume}}{(2\pi)^3}\frac{m}{\hbar^2}k'd\Omega. \tag{A.4}$$

So, putting Eq. A.4 into Eq. A.1 and then putting Eq. A.1 and the incident flux into Eq. 2.8, the differential cross-section becomes

$$\begin{aligned}(\frac{d\sigma}{d\Omega})_{\lambda\to\lambda'} &= \frac{1}{\text{Volume}}\frac{m}{\hbar}\frac{1}{k}\frac{1}{d\Omega}\frac{2\pi}{\hbar}\frac{\text{Volume}}{(2\pi)^2}\frac{m}{\hbar^2}k'd\Omega|<\mathbf{k}'\lambda'|V|\mathbf{k}\lambda>|^2 \\ &= \frac{k'}{k}(\frac{m}{2\pi\hbar^2})^2|<\mathbf{k}'\lambda'|V|\mathbf{k}\lambda>|^2.\end{aligned} \tag{A.5}$$

A.3 Particle wavefunction and the potential function

The wavefunction ψ_k of the neutron confined to a box is given by a plane wave, yielding:

$$\psi_k = \frac{1}{\text{Volume}}e^{i\mathbf{k}\cdot\mathbf{r}}. \tag{A.6}$$

Putting this form of the wavefunction into Eq. A.2 gives

$$<\mathbf{k}'\lambda'|V|\mathbf{k}\lambda>=\frac{1}{\text{Volume}}\int e^{-i\mathbf{k}'\cdot\mathbf{r}}\chi^*_{\lambda'}Ve^{i\mathbf{k}\cdot\mathbf{r}}\chi_\lambda d\mathbf{R}d\mathbf{r}. \tag{A.7}$$

A further simplification is possible here with the introduction of a more specific potential. Since the scattering depends upon the distance between the neutron and the j^{th} nucleus, the potential will have the form $V = \sum_j V_j(\mathbf{x}_j)$, where $\mathbf{x}_j$ is the separation distance. For an arbitrary origin point, the potential can be written as $V = \sum_j V_j(\mathbf{r} - \mathbf{R}_j)$, with $\mathbf{r}$ as the distance from the origin to the neutron and $\mathbf{R}_j$ as the distance from the origin to the j^{th} nucleus. Eq. A.7 can be written as

$$< \mathbf{k}'\lambda'|V|\mathbf{k}\lambda >= \sum_j \int e^{-i\mathbf{k}'\cdot(\mathbf{x}_j+\mathbf{R}_j)}\chi^*_{\lambda'}V_j(\mathbf{x}_j)e^{i\mathbf{k}\cdot\mathbf{r}}\chi_\lambda d\mathbf{R}d\mathbf{x}_j \tag{A.8}$$

$$< \mathbf{k}'\lambda'|V|\mathbf{k}\lambda >= \sum_j \int V_j(\mathbf{x}_j)e^{i(\mathbf{k}-\mathbf{k}')\cdot\mathbf{x}_j}d\mathbf{x}_j \int \chi^*_{\lambda'}e^{i(\mathbf{k}-\mathbf{k}')\cdot\mathbf{R}}\chi_\lambda d\mathbf{R} \tag{A.9}$$

$$< \mathbf{k}'\lambda'|V|\mathbf{k}\lambda >= \sum_j V_j(\mathbf{q}) < \lambda'|e^{i\mathbf{q}\cdot\mathbf{R}_j}|\lambda >, \tag{A.10}$$

with $V_j(\mathbf{q}) = \int V_j(\mathbf{x}_j)e^{i(\mathbf{k}-\mathbf{k}')\cdot\mathbf{x}_j}d\mathbf{x}_j$, $< \lambda'|e^{i\mathbf{q}\cdot\mathbf{R}_j}|\lambda >= \int \chi^*_{\lambda'}e^{i(\mathbf{k}-\mathbf{k}')\cdot\mathbf{R}}\chi_\lambda d\mathbf{R}$, and **q=k-k'** is the scattering vector.

Inserting Eq. A.10 into Eq. A.5, the equation becomes

$$(\frac{d\sigma}{d\Omega})_{\lambda\to\lambda'} = \frac{k'}{k}(\frac{m}{2\pi\hbar^2})^2|\sum_j V_j(\mathbf{q}) < \lambda'|V_j(i\mathbf{q}\cdot\mathbf{R}_j)|\lambda > |^2. \tag{A.11}$$

Eq. A.11 is in a form where it is easy to see that there is a correlation between the initial and final states.

A.4 Fermi pseudopotential

Introduce the Fermi pseudopotential $V(\mathbf{r}) = a\delta(\mathbf{r})$ to further simplify Eq. A.11. Consider only one term in the summation so that $\mathbf{R}_1 = 0$ and $\lambda = \lambda'$. Eq. A.11 becomes

$$\frac{d\sigma}{d\Omega} = \frac{k'}{k}(\frac{m}{2\pi\hbar^2})^2|\int V(\mathbf{r})e^{i\mathbf{q}\cdot\mathbf{r}}d\mathbf{r}|^2, \tag{A.12}$$

when k=k'. With the introduction of the Fermi pseudopotential, the integral in Eq. A.12 is

$$\int V(\mathbf{r})e^{i\mathbf{q}\cdot\mathbf{r}}d\mathbf{r} = a\int \delta(\mathbf{r})e^{i\mathbf{q}\cdot\mathbf{r}}d\mathbf{r} = a. \tag{A.13}$$

So,

$$\frac{d\sigma}{d\Omega} = \frac{k'}{k}(\frac{m}{2\pi\hbar^2})^2a^2. \tag{A.14}$$

We can set this constant equal to b, also called the scattering length. This makes the Fermi pseudopotential

$$V(\mathbf{r}) = \frac{2\pi\hbar^2}{m}\delta(\mathbf{r}). \tag{A.15}$$

Using the Fermi pseudopotential, the differential cross-section can be written as

$$(\frac{d\sigma}{d\Omega})_{\lambda\to\lambda'} = \frac{k'}{k}|\sum_j b_j < \lambda'|e^{i\mathbf{q}\cdot\mathbf{R}_j}|\lambda > |^2. \tag{A.16}$$

Appendix B
Partial differential cross-section

B.1 Hamiltonian

Introduce the Hamiltonian such that the eigenfunctions are the states λ and λ' with corresponding energies E_λ and $E_{\lambda'}$ for all states. We can then write $H^n|\lambda>=E_\lambda^n|\lambda$, leading to

$$e^{-iHt/\hbar}|\lambda>=e^{-iE_\lambda t/\hbar}|\lambda> . \tag{B.1}$$

By substituting this result into Eq. 2.12, we get

$$\begin{aligned}&(\frac{d^2\sigma}{d\Omega dE'})_{\lambda\to\lambda'}\\&=\frac{k'}{k}\sum_{jj'}b_{j'}b_j<\lambda|e^{-i\mathbf{q}\cdot\mathbf{R}_{j'}}|\lambda'><\lambda'|e^{i\mathbf{q}\cdot\mathbf{R}_j}|\lambda>\frac{1}{2\pi\hbar}\int_{-\infty}^{\infty}e^{i(E_{\lambda'}-E_\lambda)t/\hbar}e^{-i\omega t}dt,\end{aligned} \tag{B.2}$$

where $\hbar\omega=E-E'$. Eq. B.2 can be written as

$$\begin{aligned}&(\frac{d^2\sigma}{d\Omega dE'})_{\lambda\to\lambda'}\\&=\frac{k'}{k}\frac{1}{2\pi\hbar}\sum_{jj'}b_{j'}b_j\int_{-\infty}^{\infty}<\lambda|e^{-i\mathbf{q}\cdot\mathbf{R}_{j'}}|\lambda'><\lambda'|e^{iHt/\hbar}e^{i\mathbf{q}\cdot\mathbf{R}_j}e^{-iHt/\hbar}|\lambda>e^{-i\omega t}dt,\end{aligned} \tag{B.3}$$

B.2 Summation notation

The $(...)_{\lambda\to\lambda'}$ notation refers to the summation of all processes, which takes the system from a state λ to a state λ'. So,

$$\frac{d^2\sigma}{d\Omega dE'}=\sum_{\lambda\lambda'}p_\lambda(\frac{d^2\sigma}{d\Omega dE'})_{\lambda\to\lambda'}, \tag{B.4}$$

where p_λ is the probability that the system is in a state λ, namely

$$p_\lambda = \frac{e^{-E_\lambda \beta}}{\sum_\lambda e^{-E_\lambda \beta}}, \tag{B.5}$$

and $\beta = 1/k_B T$. Then we use the relation

$$\sum_{\lambda'} < \lambda|A|\lambda' >< \lambda'|B|\lambda >=< \lambda|AB|\lambda > \tag{B.6}$$

to get Eq. 2.15.

B.3 Heisenberg operator

The Heisenberg time-independent operator is $\hat{R}_j(t)$ such that

$$\hat{R}_j(t) = e^{iHt/\hbar}\hat{R}_j e^{-iHt/\hbar}, \hat{R}_j(0) = \hat{R}_j \tag{B.7}$$

and

$$e^{i\mathbf{q}\cdot\mathbf{R}_j(t)} = e^{iHt/\hbar}e^{i\mathbf{q}\cdot\mathbf{R}_j}e^{-iHt/\hbar}. \tag{B.8}$$

B.4 Thermal average

The thermal average of $\hat{A}$ is

$$< \hat{A} >= \sum_\lambda p_\lambda < \lambda|A|\lambda > \tag{B.9}$$

B.5 Small momentum transfer approximation

The exponential tends to zero as $q \to 0$ in

$$S(\mathbf{q}) = 1 + \int [g(\mathbf{r}) - \rho]e^{i\mathbf{q}\cdot\mathbf{r}}d\mathbf{r}, \tag{B.10}$$

so

$$\begin{aligned} S(0) &= 1 + \int [g(r) - \rho] d\mathbf{r} \\ &= 1 + \int g(r) d\mathbf{r} - \int \rho d\mathbf{r} \\ &= 1 + \int g(r) d\mathbf{r} - \overline{n}, \end{aligned} \tag{B.11}$$

where $\overline{n}$ is the mean number of atoms in a volume. Now, consider that volume fixed. The number of atoms can vary inside that volume in a liquid according to $\overline{n} = \rho\overline{V}$. Assume that if there is an atom at a certain point $\mathbf{r}_1$ and, given this atom at $\mathbf{r}_1$, there is an atom at $\mathbf{r}_2$ at the same time, then

$$\begin{aligned} \overline{n^2} &= \int_{\overline{V}} \int_{\overline{V}} [\delta(\mathbf{r}_2 - \mathbf{r}_1) + g(\mathbf{r}_2 - \mathbf{r}_1)] \rho d\mathbf{r}_1 d\mathbf{r}_2 \\ &= \overline{n} \int_{\overline{V}} [\delta(\mathbf{r}_2 - \mathbf{r}_1) + g(\mathbf{r}_2 - \mathbf{r}_1)] d\mathbf{r}_2 \\ &= \overline{n}[1 + \int_{\overline{V}} g(r) d\mathbf{r}]. \end{aligned} \tag{B.12}$$

Rearranging the above equation gives

$$\frac{\overline{n^2}}{\overline{n}} = 1 + \int_{\overline{V}} g(r) d\mathbf{r}. \tag{B.13}$$

Substituting Eq. B.13 into Eq. B.11 yields

$$\begin{aligned} S(0) &= \frac{\overline{n^2}}{\overline{n}} - \overline{n} \\ &= \frac{\overline{(\Delta n)^2}}{\overline{n}} \end{aligned} \tag{B.14}$$

with $\Delta n = n - \overline{n}$. Relating number fluctuation to volume fluctuation, the equation becomes

$$S(0) = \rho \frac{\overline{(\Delta V)^2}}{\overline{V}}, \tag{B.15}$$

with $\Delta V = V - \overline{V}$. At this point, a relation between $\overline{(\Delta V)^2}$ and $\overline{V}$ is needed. If the volume of the system is between V and V+dV, then the probability is proportional to

$e^{-\beta G_0} dV$, where β is $1/k_b T$ and $G_0 = \overline{E} - T_0 S + p_0 V$. Performing a Taylor expansion around G_0 gives

$$G_0 = G_0(\overline{V}) + \frac{1}{2} \frac{1}{\overline{V} \kappa_T}, \tag{B.16}$$

so the probability goes as something proportional to $e^{-\frac{\beta}{2\kappa_T} \frac{(\Delta V)^2}{\overline{V}}}$. Standard deviation of a Gaussian is $\overline{(\Delta V)^2} = \overline{V} \kappa_T / \beta$. This result substituted into Eq. B.15 yields

$$S(0) = \frac{\rho \kappa_T}{\beta}. \tag{B.17}$$

Appendix C
magnetic surprise for liquids- physics world.com

The following is a [verbatim] popular write up of our investigation of possible magnetism in diamagnetic metals. It was written by Belle Dumé, who is a Science Writer at PhysicsWeb (now Physicsworld).

Jun 29, 2005

Magnetic surprise for liquids Physicists have found that some liquid metals which appear to be non-magnetic -- such as mercury, aluminium, gallium and lead -- actually contain magnetic moments that appear and disappear on extremely short time scales. Wouter Montfrooij and colleagues at the University of Missouri made the discovery, which had been predicted by theorists, when they re-analysed neutron scattering data. The phenomenon is thought to be caused by a phenomenon called cage diffusion.

Cage-diffusion occurs when an atom in a liquid bounces off neighbouring atoms and becomes confined to a ‘‘cage". In

self-diffusion, on the other hand, the atom simply moves through the liquid. Molecular dynamics simulations have shown that these two processes take place on very different time scales: cage-diffusion occurs on picosecond (10-12 s) time scales, while self-diffusion takes much longer. Neutron scattering can be used to observe both.

At first the results of neutron scattering experiments and molecular dynamics calculations on liquid mercury did not agree with each other. However, in 2003, Yaspal Badyal of the Oak Ridge National Laboratory and colleagues suggested that the discrepancy might be caused by the atoms in the liquid having a magnetic moment that fluctuates.

The basic idea is as follows: atoms can approach each other very closely in a liquid, which can cause an electron to be ejected from a filled inner shell. This results in the atom having an unpaired electron -- and therefore a magnetic moment. Once the ions move away from each other, the shell fills up again. This means that the magnetic moment should pop in and out of existence on the same time scale as the ion ‘‘rattles around" in the cage formed by its neighbours.

Montfrooij and colleagues have now shown that the cage-diffusion

process is indeed accompanied by a fluctuating magnetic moment in liquid metals. By re-analysing published neutron scattering data on various liquids, they found that ions in gallium, aluminium and lead show a large effect similar to mercury, which has unpaired electrons for up to 20\% of the time.

‘‘Not only do these magnetic moments provide an additional means for studying cage-diffusion by neutron scattering, they provide an additional long-range interaction mechanism for the ions in the liquid," they write in a paper that will be published in Physical Review E.

Appendix D
Corrections to data

D.1 Slab attenuation

The elastic slab attenuation is given by

$$A_s(E_0,\phi) = N\int_0^d e^{-\sigma\rho(\frac{d-x}{\cos\phi})}e^{-\sigma\rho x}dx, \tag{D.1}$$

where N is the normalization, which is $\frac{1}{d}$ here. The solution is as follows:

$$\begin{aligned}
A_s(E_0,\phi) &= \frac{1}{d}\int_0^d e^{-\sigma\rho(\frac{d-x}{\cos\phi})}e^{-\sigma\rho x}dx \\
&= \frac{1}{d}\int_0^d e^{-\sigma\rho d/\cos\phi}e^{\sigma\rho x/\cos\phi}e^{-\sigma\rho x}dx \\
&= \frac{1}{d}e^{-\sigma\rho d/\cos\phi}\int_0^d e^{\sigma\rho(\frac{1}{\cos\phi}-1)x}dx \\
&= \frac{1}{d}e^{-\sigma\rho d/\cos\phi}[\sigma\rho(\frac{1}{\cos\phi}-1)]^{-1}e^{\sigma\rho(\frac{1}{\cos\phi}-1)x}|_0^d \\
&= \frac{1}{d}e^{-\sigma\rho d/\cos\phi}[\sigma\rho(\frac{1}{\cos\phi}-1)]^{-1}[e^{\sigma\rho(\frac{1}{\cos\phi}-1)d}-1] \\
&= [d\sigma\rho(\frac{1}{\cos\phi}-1)]^{-1}[e^{-\sigma\rho d/\cos\phi}e^{\sigma\rho(\frac{1}{\cos\phi}-1)d}-e^{-\sigma\rho d/\cos\phi}] \\
&= [d\sigma\rho(\frac{1}{\cos\phi}-1)]^{-1}[e^{-\sigma\rho d/\cos\phi}e^{\sigma\rho d/\cos\phi}e^{-\sigma\rho d}-e^{-\sigma\rho d/\cos\phi}] \\
&= [d\sigma\rho(\frac{1}{\cos\phi}-1)]^{-1}[e^{-\sigma\rho d}-e^{-\sigma\rho d/\cos\phi}].
\end{aligned} \tag{D.2}$$

For inelastic scattering, the difference is in the σ term. We can say that $\sigma = \sigma_{coh} + \sigma_{inc} + \sigma_{abs}$ where σ_{abs} is defined for $E = 25.3$meV as $\sigma_{abs} = \sigma_{abs}(E = 25.3meV)\sqrt{25.3meV/E_i}$. This σ is associated with the incident neutron beam, before scattering occurs. Then σ' would be $\sigma_{coh} + \sigma_{inc} + \sigma_{abs}\sqrt{\frac{E_i}{E_i-E}}$ which is associated with the scattered neutrons. This change makes the attenuation factor

$$A_s(E_0,\phi) = \frac{1}{d}\int_0^d e^{-\sigma'\rho(\frac{d-x}{\cos\phi})}e^{-\sigma\rho x}dx, \tag{D.3}$$

and the solution becomes

$$\begin{aligned}
A_s(E_0,\phi) &= \frac{1}{d}\int_0^d e^{-\sigma'\rho(\frac{d-x}{\cos\phi})}e^{-\sigma\rho x}dx \\
&= \frac{1}{d}\int_0^d e^{-\sigma'\rho d/\cos\phi}e^{\sigma'\rho x/\cos\phi}e^{-\sigma\rho x}dx \\
&= \frac{1}{d}e^{-\sigma'\rho d/\cos\phi}\int_0^d e^{\sigma'\rho(\frac{1}{\cos\phi}-1)x}dx \\
&= \frac{1}{d}e^{-\sigma'\rho d/\cos\phi}[\rho(\frac{\sigma'}{\cos\phi}-\sigma)]^{-1}e^{\rho(\frac{\sigma'}{\cos\phi}-\sigma)x}|_0^d \\
&= [d\rho(\frac{\sigma'}{\cos\phi}-\sigma)]^{-1}e^{-\sigma'\rho d/\cos\phi}[e^{d\rho(\frac{\sigma'}{\cos\phi}-\sigma)}-1] \\
&= [d\rho(\frac{\sigma'}{\cos\phi}-\sigma)]^{-1}[e^{-\sigma'\rho d/\cos\phi+\sigma'\rho d/\cos\phi-\sigma\rho d}-e^{-\sigma'\rho d/\cos\phi}] \\
&= [d\rho(\frac{\sigma'}{\cos\phi}-\sigma)]^{-1}[e^{-\sigma\rho d}-e^{-\sigma'\rho d/\cos\phi}].
\end{aligned} \tag{D.4}$$

For elastic scattering where the ϕ_0 is included, the integral is

$$A_s(E_0,\phi) = \frac{1}{d}\int_0^d e^{-\sigma\rho(\frac{d-x}{\cos(\phi-\phi_0)})}e^{-\sigma\rho x/\phi_0}dx. \tag{D.5}$$

The solution is as follows:

$$\begin{aligned}
A_s(E_0,\phi) &= \frac{1}{d}\int_0^d e^{-\sigma\rho(\frac{d-x}{\cos(\phi-\phi_0)})}e^{-\sigma\rho x/\phi_0}dx \\
&= \frac{1}{d}\int_0^d e^{-\sigma\rho d/\cos(\phi-\phi_0)}e^{\sigma\rho x/\cos(\phi-\phi_0)}e^{-\sigma\rho x/\phi_0}dx \\
&= \frac{1}{d}e^{-\sigma\rho d/\cos(\phi-\phi_0)}\int_0^d e^{\sigma\rho(\frac{1}{\cos(\phi-\phi_0)}-\frac{1}{\cos\phi_0})x}dx \\
&= \frac{1}{d}e^{-\sigma\rho d/\cos(\phi-\phi_0)}\frac{1}{\sigma\rho(\frac{1}{\cos(\phi-\phi_0)}-\frac{1}{\cos\phi_0})}e^{\sigma\rho(\frac{1}{\cos(\phi-\phi_0)}-\frac{1}{\cos\phi_0})x}|_0^d \\
&= \frac{1}{\sigma\rho d(\frac{1}{\cos(\phi-\phi_0)}-\frac{1}{\cos\phi_0})}e^{-\sigma\rho d/\cos(\phi-\phi_0)}[e^{\sigma\rho(\frac{1}{\cos(\phi-\phi_0)}-\frac{1}{\cos\phi_0})d}-1] \\
&= \frac{1}{\sigma\rho d(\frac{1}{\cos(\phi-\phi_0)}-\frac{1}{\cos\phi_0})}[e^{-\sigma\rho d/\cos(\phi-\phi_0)}e^{\sigma\rho d/\cos(\phi-\phi_0)}e^{-\sigma\rho d/\cos\phi_0}-e^{-\sigma\rho d/\cos(\phi-\phi_0)}] \\
&= \frac{1}{\sigma\rho d(\frac{1}{\cos(\phi-\phi_0)}-\frac{1}{\cos\phi_0})}[e^{-\sigma\rho d/\cos\phi_0}-e^{-\sigma\rho d/\cos(\phi-\phi_0)}],
\end{aligned} \tag{D.6}$$

where ϕ_0 is the angle made by the perpendicular of the incident beam and sample slab.

Appendix E
Partial wave method

E.1 Incident plane wave

Start with the incident plane wave $\psi = e^{i\mathbf{q}\cdot\mathbf{r}}$. This is the solution to the equation $\nabla^2\psi + q^2\psi = 0$. The incident wavefunction can also be solved in spherical coordinates. The equation is

$$\frac{1}{r^2}\frac{d}{dr}(r^2\frac{df}{dr}) + (k^2 - \frac{l(l+1)}{r^2})f = 0, \tag{E.1}$$

and if f is a solution, then so is $\psi = P_l(\cos\theta)f_l(r) = \sum_{l=0}^{\infty} A_l P_l(\cos\theta)f_l(r)$, where $P_l(\cos\theta)$ is the l^{th} Legendre coefficient and A_l is a coefficient as yet undetermined. The f's are Bessel functions with an asymptotic form

$$f_l(r) \sim \frac{\sin(qr - \frac{1}{2}l\pi)}{qr}. \tag{E.2}$$

To determine the coefficient A_l, we set the two wavefunctions equal to each other.

$$\sum_{l=0}^{\infty} A_l P_l(\cos\theta)f_l(r) = e^{iqr\cos\theta} \tag{E.3}$$

Then we multiply both sides by $P_l(\cos\theta)\sin\theta$ and integrate; we get

$$\int_0^{\pi} P_l(\cos\theta)\sin\theta[\sum_{l=0}^{\infty} A_l P_l(\cos\theta)f_l(r) = e^{iqr\cos\theta}]d(\cos\theta) \tag{E.4}$$

$$\sum_{l=0}^{\infty}\int_0^{\pi} A_l {P_l}^2(\cos\theta)f_l(r)\sin\theta d(\cos\theta) = \int_0^{\pi} P_l(\cos\theta)e^{iqr\cos\theta}\sin\theta d(\cos\theta). \tag{E.5}$$

Then substitute $t = \cos\theta$, $dt = -\sin\theta d\theta$ into Eq. E.5.

$$\sum_{l=0}^{\infty} \int_{-1}^{+1} A_l {P_l}^2(t) f_l(r) dt = \int_{-1}^{+1} e^{iqrt} P_l(t) dt \tag{E.6}$$

The left-hand side of Eq. E.6 is

$$\begin{aligned} \sum_{l=0}^{\infty} \int_{-1}^{+1} A_l {P_l}^2(t) f_l(r) dt &= \sum_{l=0}^{\infty} A_l f_l(r) \int_{-1}^{+1} {P_l}^2(t) dt \\ &= A_l f_l(r) (\frac{2}{2l+1}). \end{aligned} \tag{E.7}$$

The right-hand side of Eq. E.6 integrated by parts is

$$\begin{aligned} \int_{-1}^{+1} e^{iqrt} P_l(t) dt &= \frac{1}{iqr} [e^{iqrt} P_l(t)]|_{-1}^{+1} - \frac{1}{iqr} \int_{-1}^{+1} e^{iqrt} P_l'(t) dt \\ &\approx 2i^l \frac{\sin(qr - l\pi/2)}{qr}. \end{aligned} \tag{E.8}$$

The second term in the equation is much smaller than the first, so the right hand side is approximately equal to the first term. Putting the two sides together again gives the relation

$$A_l f_l(r) (\frac{2}{2l+1}) = 2i^l \frac{\sin(qr - l\pi/2)}{qr}. \tag{E.9}$$

From earlier, $f_l(r)$ is a Bessel function, so the remainder of the relation gives

$$A_l = (2l+1) i^l. \tag{E.10}$$

The wavefunction of the incident plane wave in spherical coordinates is

$$\begin{aligned} \psi &= \sum_{l=0}^{\infty} (2l+1) i^l P_l(\cos\theta) f_l(r) \\ &= \sum_{l=0}^{\infty} (2l+1) i^l P_l(\cos\theta) j_l(qr). \end{aligned} \tag{E.11}$$

E.2 Full wavefunction

Now that we have the incident wavefunction solution to the Schrödinger equation, the scattered wavefunction is the only piece that is missing. To get that scattered

solution, we will construct the wavefunction solution to the full Schrödinger equation and subtract the incident wavefunction solution. The Schrödinger equation in this case is

$$\frac{1}{r^2}\frac{d}{dr}(r^2\frac{dL_l}{dr}) + (k^2 - U(r) - \frac{l(l+1)}{r^2})L_l = 0. \tag{E.12}$$

To simplify the math, let $L_l = G_l/r$, making Eq. E.12 now

$$\frac{d^2G_l}{dr^2} + (k^2 - U(r) - \frac{l(l+1)}{r^2})G_l = 0. \tag{E.13}$$

For large r, the potential U(r) and the spherical potential both go to zero. This means that the solution G_l should have the form $B\sin(qr+\epsilon)$. This makes the full wavefunction of the form

$$L_l(r) = \frac{\sin(qr - l\pi/2 + \eta_l)}{qr}, \tag{E.14}$$

where the ϵ becomes the phase factor η_l.

So, the full solution has the form

$$B_lL_l(r) \sim (2l+1)i^l f_l(r) + C_l\frac{e^{iqr}}{r} \tag{E.15}$$

$$C_l\frac{e^{iqr}}{r} \sim B_lL_l(r) - (2l+1)i^l f_l(r) \tag{E.16}$$

$$\sim B_l\frac{\sin(qr - l\pi/2 + \eta_l)}{qr} - (2l+1)i^l\frac{\sin(qr - l\pi/2)}{qr} \tag{E.17}$$

$$\sim \frac{B_l}{qr}\sin(qr - l\pi/2 + \eta_l) - \frac{(2l+1)i^l}{qr}\sin(qr - l\pi/2) \tag{E.18}$$

$$\sim \frac{B_l}{qr}\frac{e^{i(qr-l\pi/2)}e^{i\eta_l} - e^{-i(qr-l\pi/2)}e^{-i\eta_l}}{2i} + \frac{(2l+1)i^l}{qr}\frac{-e^{i(qr-l\pi/2)} + e^{-i(qr-l\pi/2)}}{2i} \tag{E.19}$$

$$\sim \frac{e^{i(qr-l\pi/2)}}{2iqr}[B_le^{i\eta_l} - (2l+1)i^l] - \frac{e^{-i(qr-l\pi/2)}}{2iqr}[B_le^{-i\eta_l} - (2l+1)i^l]. \tag{E.20}$$

We want the e^{-iqr} term to vanish, so that means

$$[B_le^{-i\eta_l} - (2l+1)i^l] = 0, \tag{E.21}$$

or

$$B_l = (2l+1)i^l e^{i\eta_l}. \tag{E.22}$$

This gives the full wavefunction solution of

$$\psi = \sum_{l=0}^{\infty}(2l+1)i^l e^{i\eta_l} P_l(\cos\theta)L_l(r). \tag{E.23}$$

The asymptotic form of the scattered wave is

$$f(\theta)\frac{e^i qr}{r}, \tag{E.24}$$

where

$$\begin{aligned} f(\theta) &= \frac{1}{2iq}\sum_{l=0}^{\infty}(2l+1)[e^{2i\eta_l}-1]P_l(\cos\theta) \\ &= \frac{1}{q}\sum_{l=0}^{\infty}(2l+1)e^{i\eta_l}\sin\eta_l P_l(\cos\theta). \end{aligned} \tag{E.25}$$

Appendix F
Computer code

F.1 Multiple scattering code

This code calculates the scattering of a given order.

```
function
master1_get_scat,ei,phi,energy,sigma,absorbtion,point,direction,order,gammaq=gammaq,$
    qsq=qsq,sq=sq,sig_inc=sig_inc,gam_inc=gam_inc,npts=npts,not_first=not_first,$
    mingam=mingam,xsize=xsize,ysize=ysize,zsize=zsize
  ;ei = initial energy [meV]
  ;phi = phi angle [rad]
  ;energy = total energy transfer [meV] = ef - ei
  ;absorbtion = absorbtion cross-section * density [barn*atom/ang^3]
  ;point = initial location of scatterer (could be inside or outside of sample).  given in
        ;[x,y,z]
  ;direction = initial direction of motion of scatterer.  given in [x,y,z]
  ;order = highest order of scattering
  ;gammaq = linewidth of structure factor at a given q-value
  ;qsq = intensity of structure factor at given q-value
  ;sq = given q-value for gammaq and qsq
```

```
  ;sig_inc = incoherent cross-section * density
  ;gam_inc = incoherent linewidth
  ;npts = number of divisions in len
  ;not_first = indicator that the program is calling itself for higher orders
  ;xsize, ysize, and zsize indicate the sample size [cm]  eg. ysize=[-0.2,0.2]

res=fltarr(n_elements(energy),n_elements(phi))

if n_elements(gammaq) ne n_elements(qsq) then gammaq=gammaq*qsq^2
   if keyword_set(sig_inc) then begin
      if n_elements(gam_inc) ne n_elements(qsq) then gam_inc=gam_inc*qsq^2
   endif
if keyword_set(mingam) then begin
   ind=where(gammaq lt mingam,cc)
   if cc ne 0 then gammaq(ind)=mingam
      if keyword_set(gam_inc) then begin
```

```
         ind=where(gam_inc lt mingam,cc)
            if cc ne 0 then gam_inc(ind)=mingam
      endif
endif if not keyword_set(sig_inc) then sig_inc=0 if not
keyword_set(npts) then npts=10 npts=long(npts)

sel=sigma+sig_inc+absorbtion*sqrt(25.3/ei)    ;total cross-section
dmax=max(-alog(0.001)/sel)      ;to avoid too much computation
ki=sqrt(ei/2.0718) if n_elements(ki) gt 1 then
kelastic=min(sqrt((ei-energy)/2.0718)) else kelastic=ki

if not keyword_set(xsize) then xsize=[-12.5,12.5]   ;sample size if
not keyword_set(ysize) then ysize=[-0.2,0.2] if not
keyword_set(zsize) then zsize=[-12.5,12.5] ; in [cm]

;make neutron contact sample if not keyword_set(not_first) then
```

```
begin
   direction=direction/sqrt(scalar_product(direction,direction)) ;unit vector
   vec=direction
   pold=point
  ;x-dir
   if abs(vec(0)) ge 0.001 then begin
    lx=[(xsize(0)-pold(0))/(vec(0)),(xsize(1)-pold(0))/(vec(0))]
    lx=lx(where(lx ge 0)) & if n_elements(lx) eq 2 then point=point+min(lx)*vec
   endif else lx=1.e6
  ;y-dir
   if abs(vec(1)) ge 0.001 then begin
    ly=[(ysize(0)-pold(1))/(vec(1)),(ysize(1)-pold(1))/(vec(1))]
    ly=ly(where(ly ge 0)) & if n_elements(ly) eq 2 then point=point+min(ly)*vec
   endif else ly=1.e6
  ;z-dir
   if abs(vec(2)) ge 0.001 then begin
```

```
    lz=[(zsize(0)-pold(2))/(vec(2)),(zsize(1)-pold(2))/(vec(2))]
    lz=lz(where(lz ge 0)) & if n_elements(lz) eq 2 then point=point+min(lz)*vec
   endif else lz=1.e6
  ;end program if neutron misses
   if min([lx,ly,lz]) gt 1e5 then begin
    print,'neutron misses sample'
    return,-1
   endif
endif

if order gt 1 then begin    ;need higher order basis outside of
'for' loop
  phiac=(findgen(npts)+0.5)*2.*!pi/npts
  th=(findgen(npts)+0.5)*!pi/npts
  hdir=fltarr(3,npts*npts)
  hdir(0,*)=(sin(th)#cos(phiac))(*)
```

```
  hdir(1,*)=(cos(th)#(phiac ge -100.))(*)
  hdir(2,*)=(sin(th)#sin(phiac))(*)
  np2=npts*npts
  sint=(sin(th)#(phiac ge -100.))(*)
endif

;FAKE loop. for z=0,n_elements(direction)/3-1 do begin
  pold=point
  vec=direction(*,z)
 ;find nearest point of sample exit for point and/or path length
  ;x-dir
   if abs(vec(0)) ge 0.001 then begin
    lx=[(xsize(0)-pold(0))/(vec(0)),(xsize(1)-pold(0))/(vec(0))]
    lx=lx(where(lx gt 0))
   endif else lx=1.e6
  ;y-dir
```

```
 if abs(vec(1)) ge 0.001 then begin
  ly=[(ysize(0)-pold(1))/(vec(1)),(ysize(1)-pold(1))/(vec(1))]
  ly=ly(where(ly gt 0))
 endif else ly=1.e6
;z-dir
 if abs(vec(2)) ge 0.001 then begin
  lz=[(zsize(0)-pold(2))/(vec(2)),(zsize(1)-pold(2))/(vec(2))]
  lz=lz(where(lz gt 0))
 endif else lz=1.e6

 ;shortest distance to leave sample.  will break this into npts segments of equal length
 len=min([lx,ly,lz])

 if len gt dmax then len=dmax   ;to avoid too much computation

;for order 0 ==> attenuation
```

```
 if order eq 0 then begin
  res(*)=exp(-len*sel)    ;transmission probability
 endif else begin
  lens=len
  if len*sigma gt 4 then begin
   lens=4./sigma
  endif else cf=1.

;for order 1 ==> attenuation + single scattering
  cf=lens/len
  h=(findgen(npts)+0.5)/npts*lens
  kf=sqrt((ei-energy)/2.0718)
 if order eq 1 then begin
  for k=0,npts-1 do begin
   f=h(k)
   pp=f*vec+point
```

```
inel=sigma+sig_inc+absorbtion*sqrt(25.3/ei)

at1=exp(-inel*f)

hh=fltarr(3,n_elements(phi))

 hh(0,*)=sin(phi)   ;final dir known

 hh(1,*)=cos(phi)

cx=transpose(scalar_product(hh,vec)) ;scattering angles at final scattering event


for l=0,n_elements(phi)-1 do begin

 argu=ki^2+kf^2-2.*ki*kf*cx(l)

 ;q=sqrt(argu*(argu ge 0))+0.001

 q=sqrt(argu)

 s=interpoll(q,qsq,sq)      ;structure factors for these scattering events

 g=interpoll(q,qsq,gammaq)  ;linewidths for these q-values

  if keyword_set(sig_inc) then gi=interpoll(q,qsq,gam_inc)

 pref=at1/!pi*s*g/(energy^2+g^2)

  if keyword_set(sig_inc) then pref=pref+at1/!pi*gi/(energy^2+gi^2)*sig_inc/sigma
```

```
    res(*,l)=res(*,l)+pref*master1_get_scat(ei-energy,phi(l),energy,sigma,absorbtion,$
                pp(*),hh(*,l),0,npts=npts,/not_first)
    ;with order=0 and /not_first
   endfor
  endfor

;higher order scattering ==> attenuation + single scattering + HOT
 endif else begin
  if keyword_set(sig_inc) then bbb=sig_inc/sigma else bbb=0
  sel=sigma+sig_inc+absorbtion*sqrt(25.3/(kelastic^2*2.0718))
  for k=0,npts-1 do begin & print,k+1
    f=h(k)
    pp=point+f*vec
    at1=exp(-sel*f)
     ;double integration over intermediate angles
     cx=acos(transpose(scalar_product(vec,hdir)))  ;in the np2 direction
```

```
        q1=2.*kelastic*sin(cx/2)
        sq1=interpoll(q1,qsq,sq)
        gamma1=interpoll(q1,qsq,gammaq)
       for l=0,np2-1 do begin
         res=res+at1*sint(l)*(sq1(l)+bbb)*master1_get_scat(ei,phi,energy,sigma,absorbtion,$
                   pp(*),hdir(*,l),order-1,/not_first,mingam=mingam,npts=npts/5,qsq=qsq,$
                   sq=sq,gammaq=gammaq+gamma1(l),sig_inc=sig_inc,gam_inc=gam_inc)
                   ;with order=order-1
       endfor
     endfor
    res=!pi/2.*res/np2                    ;to normalize
    endelse
    res=(sigma+sig_inc)*len*res/npts*cf   ;more normalize
   endelse
endfor
```

```
return,res end
```

This program calculates the neutron flux profile after passing through a sapphire filter.

```
function
monitor_contamination_sapphire,energy,temp=temp,h20=h20,thick=thick,norm=norm
   if not keyword_set(norm) then norm=1.
   if not keyword_set(thick) then thick=1. ; thick of filter compared to HB3 filter
   if not keyword_set(temp) then temp=303. ; temperature of reactor bath
   if not keyword_set(h20) then h20=45.62  ; thickness of water in cm that will absorb neutrons
   v=findgen(10000)+100 ;neutron speed in m/s
   lam=3956/v ;in angstrom
   num=v^3*exp(-0.5*1.67e-27*v^2/1.3805e-23/temp)*exp(-h20*2200./v*0.3326*0.033457*2)
     ; 2200./v*0.3326 is velocity dependent absorbtion x-section
     ; 0.033457*2 is atms/cm^3, two for the 2 in h2o
   num=num/integrate(v,num)
   ereactor=(2.*!pi/lam)^2*2.0718   ;in meV
   fn=smartscan('c:data\sapphire_transmission.dat')
   w=ascrd(fn)
```

```
   e=get_data_x(w) & trans=exp(alog(get_data(w))*thick)
   fluxonsample=interpoll(ereactor,e,trans)*num

   sigwanted=interpoll(energy,ereactor,fluxonsample)
   sig=sigwanted
   for z=2,6 do begin
      sig=sig+interpoll(energy*z^2,ereactor,fluxonsample)/z ;/z for monitor efficiency
   endfor
   ; use
   cor=sigwanted/sig
   ind=min(abs(energy-13.7),minind)
   cor=cor/cor(minind)*norm
return,cor end
```

This program calculates the efficiency of a cylindrical ^{3}He detector.

```
function transmission_cylinder,absorb_xsec,density,thickness
  ;absorb_xsec = absorbtion cross-section
  ;density = density of liquid [atoms/ang^3]
  ;thickness = thickness of sample [mm]

   ef=findgen(10000)/100+3   ;+3 is not forgotten.  will be taken into account later
   sigma=absorb_xsec*sqrt(25.3/ef)*density*thickness

abs_prob=fltarr(n_elements(ef))

 for m=0,7 do begin
  abs_prob=abs_prob+sigma*[sigma^(2*m)*!pi/4/factorial(m+1)/factorial(m)/2^(2*m)- $
     sigma^(2*m+1)*2^(2*m+1)*factorial(m)*factorial(m+1)/factorial(2*m+1)/factorial(2*m+3)]
 endfor
ba=min(abs(ef-13.7),ind)
```

```
return,abs_prob/abs_prob(ind)


end
```

This program calculates the attenuation due to a slab-shaped sample.

```
function
get_slab_attenuation,sigma,thickness,zerophi=zerophi,phi=phi,ei=ei,ef=ef,$
        absorb=absorb, sig_cont=sig_cont,abs_cont=abs_cont,thick_cont=thick_cont
  ;sigma = coherent cross-section * density [barn*atoms/ang^3]
  ;thickness = sample thickness [mm]
  ;zerophi = angle of sample rotation
  ;phi = angle of arm rotation
  ;ei = initial energy and ef = final energy
  ;absorb = absorbtion cross-section  density
  ;sig_cont, abs_cont, and thick_cont are the coherent cross-section * density, absorbtion
            ;cross-section * density, and thickness, respectively, of the container
if not keyword_set(zerophi) then phi0=0.0 else phi0=zerophi   ;sets
default phi0 as 0
            ;unless specified
  if phi0 eq 90. then phi0=89.9
```

```
if not keyword_set(phi) then phi=0.05                          ;sets
default phi... can't =
            ;0 else divides by zero
if not keyword_set(absorb) then absorb=0. if not keyword_set(ei)
then ei=100. if not keyword_set(ef) then ef=100.
  if n_elements(ei) ne 1 and n_elements(ef) eq 1 then ef=ef*(ei ge min(ei))
  if n_elements(ei) ne n_elements(ef) then ei=ei*(ef ge min(ef))
  if n_params() lt 2 then return,-1
if keyword_set(sig_cont) or keyword_set(abs_cont) then container=1
else container=0
  if container then if not keyword_set(sig_cont) then sig_cont=0.
  if container then if not keyword_set(abs_cont) then abs_cont=0.
pphi=(phi)
  ;need to "get rid of" points near 90 deg and such... some PROTection maybe
    prot=where(pphi gt 180.,count)
      if count ne 0 then pphi(prot)=pphi(prot)-360.          ;top or bottom of unit circle
```

```
    prot=where(pphi-phi0 eq 90.,count)
      if count ne 0 then pphi(prot)=90.01+phi0          ;stops cosines from going to zero
    prot=where(pphi-phi0 eq -90.,count)
      if count ne 0 then pphi(prot)=-89.99+phi0
    prot=where(pphi eq 90.,count)
      if count ne 0 then pphi(prot)=90.01
    prot=where(pphi eq -90.,count)
      if count ne 0 then pphi(prot)=-89.99
    prot=where(pphi eq 0.,count)                        ;stops sines from going to zero
      if count ne 0 then pphi(prot)=0.05
    prot=where(abs(pphi) lt 0.05,count)                 ;small pphi limit
      if count ne 0 then pphi(prot)=0.05*pphi(prot)/(abs(pphi(prot))+0.01)

pphi=(pphi)*!pi/180.    ;radians

pphi0=atan(tan((phi0)*!pi/180.))    ;puts phi0 between -90 and 90 in
```

```
radians b=thickness/cos(pphi0)


res=fltarr(n_elements(phi),n_elements(ef))


;  there are four sectors:
;             Pi/2
;              |
;              |
;        2     |      1
;Pi ____________|_____________ 0  <== pphi
;              |
;              |
;        3     |      4
;              |
;            -Pi/2
```

```
sect1=where(pphi ge 0. and pphi lt pphi0+!pi/2.,count1)
sect2=where(pphi le !pi and pphi gt pphi0+!pi/2.,count2)
sect3=where(pphi gt -!pi and pphi lt pphi0-!pi/2.,count3)
sect4=where(pphi lt 0. and pphi gt pphi0-!pi/2.,count4)

;sector 1 if count1 ne 0 then begin
  ph=(pphi(sect1))
  for j=0,n_elements(ef)-1 do begin
    sig_init=sigma+absorb/(sqrt(ei(j)/5.2276)*1000./2200.)
    sig_fin=sigma+absorb/(sqrt(ef(j)/5.2276)*1000./2200.)
    a=sig_init-sig_fin/(cos(ph)+sin(ph)*tan(pphi0))
    g=sig_fin/(cos(ph)+sin(ph)*tan(pphi0))

    res(sect1,j)=(exp(-g*b)-exp(-sig_init*b))/(a*b)

    prot=where(abs(a) lt 0.01,count)                    ;setup limit as a-->0
```

```
      if count ne 0 then res(sect1(prot),j)=(1-0.5*a(prot)*b)*exp(-g*b)


    if container then begin                                    ;container attenuation
      sig_cont_init=sig_cont+abs_cont/(sqrt(ei(j)/5.2276)*1000./2200.)*thick_cont/cos(pphi0)
      sig_cont_fin=sig_cont+abs_cont/(sqrt(ef(j)/5.2276)*1000./2200.)*thick_cont/(cos(ph)$
              +sin(ph)*tan(pphi0))

      res(sect1,j)=res(sect1,j)*exp(-sig_cont_init/sig_cont_fin)

    endif
  endfor
endif

;sector 2 if count2 ne 0 then begin
  ph=(pphi(sect2))
  for j=0,n_elements(ef)-1 do begin
```

```
sig_init=sigma+absorb/(sqrt(ei(j)/5.2276)*1000./2200.)

sig_fin=sigma+absorb/(sqrt(ef(j)/5.2276)*1000./2200.)

a=sig_init-sig_fin/(cos(ph)+sin(ph)*tan(pphi0))


res(sect2,j)=(1.-exp(-a*b))/(a*b)


prot=where(abs(a) lt 0.01,count)

  if count ne 0 then res(sect2(prot),j)=(1-0.5*a(prot)*b)


if container then begin                                          ;container attenuation

  sig_cont_init=sig_cont+abs_cont/(sqrt(ei(j)/5.2276)*1000./2200.)*thick_cont/cos(pphi0)

  sig_cont_fin=sig_cont+abs_cont/(sqrt(ef(j)/5.2276)*1000./2200.)*thick_cont/(cos(ph)$

          +sin(ph)*tan(pphi0))


  res(sect2,j)=res(sect2,j)*exp(-sig_cont_init/sig_cont_fin)
```

```
    endif
  endfor
endif

;sector 3 if count3 ne 0 then begin
  ph=(pphi(sect3))
  for j=0,n_elements(ef)-1 do begin
    sig_init=sigma+absorb/(sqrt(ei(j)/5.2276)*1000./2200.)
    sig_fin=sigma+absorb/(sqrt(ef(j)/5.2276)*1000./2200.)
    a=sig_init-sig_fin/(cos(ph)+sin(ph)*tan(pphi0))

    res(sect3,j)=(1.-exp(-a*b))/(a*b)

    prot=where(abs(a) lt 0.01,count)
      if count ne 0 then res(sect3(prot),j)=(1-0.5*a(prot)*b)
```

```
    if container then begin                                          ;container attenuation
      sig_cont_init=sig_cont+abs_cont/(sqrt(ei(j)/5.2276)*1000./2200.)*thick_cont/cos(pphi0)
      sig_cont_fin=sig_cont+abs_cont/(sqrt(ef(j)/5.2276)*1000./2200.)*thick_cont/(cos(ph)$
              +sin(ph)*tan(pphi0))

      res(sect3,j)=res(sect3,j)*exp(-sig_cont_init/sig_cont_fin)

    endif
  endfor
endif

;sector 4 if count4 ne 0 then begin
  ph=(pphi(sect4))
  for j=0,n_elements(ef)-1 do begin
    sig_init=sigma+absorb/(sqrt(ei(j)/5.2276)*1000./2200.)
    sig_fin=sigma+absorb/(sqrt(ef(j)/5.2276)*1000./2200.)
```

```
a=sig_init-sig_fin/(cos(ph)+sin(ph)*tan(pphi0))
g=sig_fin/(cos(ph)+sin(ph)*tan(pphi0))

res(sect4,j)=(exp(-g*b)-exp(-sig_init*b))/(a*b)

prot=where(abs(a) lt 0.01,count)
  if count ne 0 then res(sect4(prot),j)=(1-0.5*a(prot)*b)*exp(-g*b)

if container then begin                                    ;container attenuation
  sig_cont_init=sig_cont+abs_cont/(sqrt(ei(j)/5.2276)*1000./2200.)*thick_cont/cos(pphi0)
  sig_cont_fin=sig_cont+abs_cont/(sqrt(ef(j)/5.2276)*1000./2200.)*thick_cont/(cos(ph)$
          +sin(ph)*tan(pphi0))

  res(sect4,j)=res(sect4,j)*exp(-sig_cont_init/sig_cont_fin)

endif
```

```
  endfor
endif


return,res
end
```

F.2 RKG4 and phase shift code

First, the particular function is specified. I am using sodium as an example here.

```
function Na_fcn,y,dy,r,l,Vrel

f=dindgen(2) & x=dindgen(2) & Z=0.0d0

eppy= d    ;potential well depth, epsilon

;siggy= e-010    ;in m

siggy= d    ;in Ang

mu=1.9087e-026      ;in kg

hbar=1.05520e-34    ;in kg m^2/s

wn=1.d*mu/hbar*Vrel

B=2.d*mu/hbar*eppy*siggy^2

A=wn*siggy

K=A^2/B

;Z=Turkey_Na_Potential(r/siggy/1e10,eppy)+((l*1.d)*((l*1.d)+1)/r^2/B)

Z=Turkey_Na_Potential(r/siggy,eppy)+((l*1.d)*((l*1.d)+1)/r^2/B)

x(0)=y & x(1)=dy

f(0)=x(1)
```

```
f(1)=-(K-Z)*B*x(0)

return,f

end
```

where the potential is given by

```
function Turkey_Na_Potential,r,eppy

Z=11.d

k_f=2.55d  ; in Ang^-1.  for now...

A1=2.230d

A2=0.684d

A3=0.014d

k1=2.d*k_f*0.292d

k2=2.d*k_f*0.717d

k3=2.d*k_f*0.958d
```

```
alf1=-0.336d*!pi

alf2=-0.813d*!pi

alf3=-0.874d*!pi

kap1=2.d*k_f*0.899d

kap2=2.d*k_f*0.639d

kap3=2.d*k_f*0.271d

pot=2.d*Z^2/r*(A1*cos(k1*r+alf1)*exp(-kap1*r)+A2*cos(k2*r+alf2)*exp(-kap2*r)$

       +A3*cos(k3*r+alf3)*exp(-kap3*r))

return,pot/eppy

end
```

This program calculates the phase shift for a given l-value and relative velocity. The Gill portion is the relevant portion.

```
function RK4_2_Na_Phase,l,Vrel=Vrel,y_o=y_o,dy_o=dy_o,t_o=t_o,h=h,tmax=tmax,zero=zero,gill=gill,limit=limit


if not keyword_set(y_o) then y_o=0.00001d0

if not keyword_set(dy_o) then dy_o=0.00001d0

if not keyword_set(time) then t_o=0.85d0

if not keyword_set(h) then h=0.005d0

if not keyword_set(tmax) then tmax=100.00001

if not keyword_set(Vrel) then Vrel=1000.d

if not keyword_set(limit) then limit=0.01d


x=y_o

dx=dy_o

time=t_o
```

```
wave=dindgen(6,tmax/h+1)

;siggy=1.525e-010    ;in m

siggy=1.525d    ;in Ang

mu=1.9087e-026      ;in kg

hbar=1.05520e-34    ;in kg m^2/s

wn=1.d*mu/hbar*Vrel

A=wn*siggy          ; different;=8.3286798 @ Vrel=1000  m/s


;================================ quartic RK, 2nd order ODE ================================

k1=dindgen(2) & k2=dindgen(2) & k3=dindgen(2) & k4=dindgen(2) & xtemp=dindgen(2)


if not keyword_set(gill) then begin

;

;j=0l & dist=1.0d0

;;while time lt tmax do begin

;while time lt tmax and dist gt 0.00001d0 do begin
```

```
;   wave(0,j)=time & wave(1,j)=x & wave(2,j)=dx
;   f1=he_fcn(x,dx,time,l,Vrel)
;    k1(0)=f1(0)
;    k1(1)=f1(1)
;     xtemp(0)=dx+k1(1)*h/2.0d0
;     xtemp(1)=x+k1(0)*h/2.0d0
;   f2=he_fcn(xtemp(1),xtemp(0),time+h/2.0d0,l,Vrel)
;    k2(0)=f2(0)
;    k2(1)=f2(1)
;     xtemp(0)=dx+k2(1)*h/2.0d0
;     xtemp(1)=x+k2(0)*h/2.0d0
;   f3=he_fcn(xtemp(1),xtemp(0),time+h/2.0d0,l,Vrel)
;    k3(0)=f3(0)
;    k3(1)=f3(1)
;     xtemp(0)=dx+k3(1)*h
;     xtemp(1)=x+k3(0)*h
```

```
;   f4=he_fcn(xtemp(1),xtemp(0),time+h,l,Vrel)
;    k4(0)=f4(0)
;    k4(1)=f4(1)
;     dx=dx+(k1(1)+k2(1)*2.0d0+k3(1)*2.0d0+k4(1))*h/6.0d0
;     x=x+(k1(0)+k2(0)*2.0d0+k3(0)*2.0d0+k4(0))*h/6.0d0
;     time=time+h
;     j=j+1
;   zer=findzero(wave(0,*),wave(1,*))
;   if n_elements(zer) ge 3 then dist=abs(abs(zer(n_elements(zer)-2)-zer(n_elements(zer)-3))$
;          -abs(zer(n_elements(zer)-1)-zer(n_elements(zer)-2))) else dist=1.
;;  if n_elements(zer) ge 3 then dist=abs(zer(n_elements(zer)-2)-zer(n_elements(zer)-3))$
;          -(zer(n_elements(zer)-1)-zer(n_elements(zer)-2)) else dist=1.
;;     if T(n-1)-T(n) lt 0.000001 then endwhile else continue
;   if n_elements(zer) ge 3 then x_max=zer(n_elements(zer)-2) else x_max=1.0d0
endwhile
```

```
;=============================================================================================

endif else begin

;================================ quartic RKG, 2nd order ODE ==================================
j=0l & dist=1.0d0 & dist2=1.d
;while time lt tmax do begin
;while time lt tmax and dist gt 0.01d0 do begin
while time lt tmax and dist gt limit and dist2 gt limit do begin
   wave(0,j)=time & wave(1,j)=x & wave(2,j)=dx
   f1=Na_fcn(x,dx,time,l,Vrel)
    k1(0)=f1(0)
    k1(1)=f1(1)
     xtemp(0)=dx+k1(1)*h/2.0d0
     xtemp(1)=x+k1(0)*h/2.0d0
   f2=Na_fcn(xtemp(1),xtemp(0),time+h/2.0d0,l,Vrel)
```

```
 k2(0)=f2(0)
 k2(1)=f2(1)
  xtemp(0)=dx+k1(1)*h/2.0d0*(-1.0d0+sqrt(2.0d0))+k2(1)*h*(1.0d0-sqrt(2.0d0)/2.0d0)
  xtemp(1)=x+k1(0)*h/2.0d0*(-1.0d0+sqrt(2.0d0))+k2(0)*h*(1.0d0-sqrt(2.0d0)/2.0d0)
f3=Na_fcn(xtemp(1),xtemp(0),time+h/2.0d0,l,Vrel)
 k3(0)=f3(0)
 k3(1)=f3(1)
  xtemp(0)=dx-k2(1)*h*sqrt(2.0d0)/2.0d0+k3(1)*h*(1.0d0+sqrt(2.0d0)/2.0d0)
  xtemp(1)=x-k2(0)*h*sqrt(2.0d0)/2.0d0+k3(0)*h*(1.0d0+sqrt(2.0d0)/2.0d0)
f4=Na_fcn(xtemp(1),xtemp(0),time+h,l,Vrel)
 k4(0)=f4(0)
 k4(1)=f4(1)
  dx=dx+(k1(1)+k2(1)*(2.0d0-sqrt(2.0d0))+k3(1)*(2.0d0+sqrt(2.0d0))+k4(1))*h/6.0d0
  x=x+(k1(0)+k2(0)*(2.0d0-sqrt(2.0d0))+k3(0)*(2.0d0+sqrt(2.0d0))+k4(0))*h/6.0d0
  time=time+h
  j=j+1
```

```
   zer=findzero(wave(0,*),wave(1,*))


   if N_elements(zer) ge 3 then begin
      point1=zer(n_elements(zer)-3) & phase1=atan(sp_beselj(A*point1,l)/sp_besely(A*point1,l))
      point2=zer(n_elements(zer)-2) & phase2=atan(sp_beselj(A*point2,l)/sp_besely(A*point2,l))
      point3=zer(n_elements(zer)-1) & phase3=atan(sp_beselj(A*point3,l)/sp_besely(A*point3,l))
      dist=abs(abs(point2-point1)-abs(point3-point2))
      dist2=abs(abs(phase2-phase1)-abs(phase3-phase2))
   endif else begin
      dist=1.d
      dist2=1.d
   endelse
   if n_elements(zer) ge 3 then x_max=point2 else x_max=1.d
endwhile


endelse
```

```
;=============================================================================================

;print,l,'    ',x_max,'    ',systime()


x_max=phase2

return,x_max

end
```

VITA

Mark Patty was born in Alton, IL. on February 20, 1980. He graduated in 2002 with a Bachelor of Physics and a Bachelor of Mathematics from the University of Missouri - Columbia. In 2004 Mark received his Masters degree in Physics from the same institution. Mark received his Ph.D. in 2008.